11-28-2007

Intrinsic Absorption with the Far Ultraviolet Spectroscopic Explorer

Jay Patrick Dunn

Intrinsic Absorption with the Far Ultraviolet Spectroscopic Explorer

by

Jay P. Dunn

Under the Direction of D. Michael Crenshaw

Abstract

We present a survey of 72 Seyfert galaxies and quasars observed by the *Far Ultraviolet Spectroscopic Explorer (FUSE)*. Our survey is the largest to date searching for intrinsic UV absorption with high spectral resolution, and is the first step toward a more comprehensive study of intrinsic absorption in low-redshift AGN. We have determined that 72 of 253 available active galactic nuclei (AGN) are viable targets for detection of intrinsic absorption lines. We examined these spectra for signs of intrinsic absorption in the O VI doublet ($\lambda\lambda$1031.9, 1037.6) and Lyman β (λ1025.7). The fraction of Seyfert 1 galaxies and low-redshift quasars at $z \lesssim 0.15$ that show evidence of intrinsic UV absorption is $\sim$50%, which is slightly lower than Crenshaw et al. found (60%) based on a smaller sample of C IV absorption in Seyfert 1 galaxies observed with the *Hubble Space Telescope (HST)*. The intrinsic absorption lines are mostly blueshifted with respect to the rest frame of the galaxy, indicating outflow of ionized gas from

the AGN. With this new fraction we find a global covering factor of the absorbing gas with respect to the central nucleus of $\sim$0.4.

We also provide a deeper analysis of the intrinsic absorption features we found in 35 objects. We have characterized the relation between luminosity and velocity, and examined the relationships between equivalent width, full width at half maximum, velocity and continuum flux. The luminosity/velocity correlation has been explored previously by Laor & Brandt (2002), but at a significantly higher redshift and heavily weighted by Broad Absorption Line quasars. Our survey is for lower redshift and lower luminosity objects, mostly Seyfert galaxies.

We have also explored each object with multiple observations for variablity in each of the aforementioned quantities and characterized the variation of equivalent width with continuum flux. Variability for low-z AGN has been seen in the past. In our survey, we find that variability of O VI ($\lambda\lambda$1032, 1038) is less common than for the UV doublets of C IV and N V seen at longer wavelengths, because the O VI absorption is usually saturated. Lyman β absorption variability is more frequent. In the target-by-target examination we find that Broad Absorption Line (BAL) features and Narrow Absorption Line (NAL) features are related, in that they follow a single relationship between the maximum outflow velocity and the AGN luminosity, and both can be exhibited in similar luminosity objects.

IRAS F22456-5125 is one particular Seyfert galaxy that we have selected for modelling due to its interesting assortment of intrinsic absorption lines. It shows a system

of five individual kinematic components of absorption features in both O VI lines and in several of the Lyman series lines. We find that each of the components are relatively simple to model and appear to be weak in the X-ray.

Index Words: galaxies: active, galaxies: Seyfert, quasars: absorption lines, ultraviolet: galaxies

Intrinsic Absorption with the Far Ultraviolet Spectroscopic Explorer

by

Jay P. Dunn

A Dissertation Presented in Partial Fulfillment of Requirements for the Degree of

Doctor of Philosophy

in the College of Arts and Sciences

Georgia State University

2007

Intrinsic Absorption with the Far Ultraviolet Spectroscopic Explorer

by

Jay P. Dunn

Major Professor:	D. Michael Crenshaw
Committee:	Steven B. Kraemer
	Paul J. Wiita
	H. Richard Miller
	Brian Thoms

Electronic Version Approved:

Office of Graduate Studies
College of Arts & Sciences
Georgia State University
December 2007

Acknowledgments

A wise man once told me that I was the sort of person that if I was not related to him, he could still call me a friend. I hope that my work here reflects the type of work that my father is proud of. Thanks for the long talks about science growing up and the encouragement you provided me. As for my mother, I hope that all the years of torment and shirking things I should have done, such as going to high school, have not been too taxing. More than anything, I hope that I've proven that all your years of patience with me have paid off and that this dissertation can reflect that. Thanks to both of you so much!

I would like thank my brother for allowing me to bend an ear over the frivolous activities we have shared over the past five years, not to mention the last 27 years. If not for those activities I know my sanity would not be as preserved as it has been. I want to tell my significant other thank you, for putting up with my temporary loss of sanity and lack of available time these past couple of years. Also, I thank my friends, both from graduate school and those I knew long before I got to graduate school, who have aided me in keeping my sanity and put up with a lot; thank you.

D. Michael Crenshaw, you have been a great advisor and a good friend. Without your influence, suggestions, advice, corrections, mirth, etc., I would not have made it through a great program such as this. We have had several adventures and I look

forward to collaborating with you in the future on other projects, and adventures, I take on outside of my graduate education.

Thank you to all the committee members who took a good deal of time out of their lives to review my material and make sure I was worthy of the title Doctor of Philosophy. Steve Kraemer, you have been a great help over the course of my education, taking an interest in everything from this dissertation to the first poster I presented in Atlanta. I hope that in the classes I have taken with Paul Wiita over the course of my five-year stay in the astronomy PhD program, I have not embarassed myself too much. Thank you for your interest in my research and the general discussions we've had. Dick Miller, I owe you a lot. Without the summer undergraduate program I started with you and John McFarland, I would never have had the chance to experience astronomy research and the opportunity to meet my future advisor. Brian Thoms was kind enough to include me in the undergraduate Sigma Pi Sigma and Society for Physics Students here at Georgia State University, which helped me find my way into the astronomy program.

On the more technical side of things, I must thank Alvin Das for his dissertation template that works very smoothly. I know you put a lot of hard work into it. Thank you to Raj Deo for all the help with the website and for the general work of systems manager. I cannot imagine the amount of time you put into that. I especially wish to thank Raj Deo, Justin Cantrell and Duke Windsor for the quick recovery of the data we lost. And thanks to the people at Johns Hopkins University for keeping their

little satellite running as long as it did and allowing me access to the data.

Contents

Tables

Figures

Abbreviations and Acronyms

AGN	Active Galactic Nuclei
ASCA	Advanced Satellite for Cosmology and Astrophysics
BAL	broad absorption line
BLR	broad-line region
CCD	Charged Coupled Device
COG	curve of growth
COS	Cosmic Origins Spectrograph
CTIO	Cerro Telolo Interamerican Observatory
EUV	extreme ultraviolet
EW	equivalent width
FARF	flight alignment reference frame
FEC	front end counter
FES	fine error sensor
FOS	Faint Object Spectrograph
FPA	focal plane assembly
FUSE	*Far Ultraviolet Spectroscopic Explorer*
FWHM	full-width at half-maximum
GHRS	Goddard High Resolution Spectrograph

HST	*Hubble Space Telescope*
HUT	*Hopkins Ultraviolet Telescope*
IDL	Interactive Data Language
IDS	instrument data system
IGM	intergalactic medium
IR	infrared
ISM	interstellar medium
IUE	*International Ultraviolet Explorer*
LiF	Lithium Flouride
LOS	line-of-sight
MAST	Multimission Archive at Space Telescope
MCP	micro channel plate
NASA	National Aeronautic and Space Administration
NAL	narrow absorption line
NED	NASA Extragalactic Database
NLR	narrow-line region
NELR	narrow emission line region
O VI	Li-like oxygen
pc	parsecs
PSF	point spread function
quasars	quasi-stellar radio sources

ROSAT	Roentgen Satellite
SED	spectral energy distribution
SiC	Silicon Carbide
SMBH	supermassive black hole
STIS	Space Telescope Imaging Spectrograph
SXWQ	soft X-Ray weak quasar
TTAG	time-tag mode
UV	ultraviolet
3-D	three dimensional

Back off man...I'm a scientist.

—— Bill Murray (Ghostbusters)

– 1 –

Introduction

1.1 AGN: The Important Types

The subject of Active Galactic Nuclei (AGN) began in 1962 with a strong radio source whose position was determined by Hazard (1962). Schmidt (1962) showed that 3C273 had a spectrum with permitted and forbidden lines that were redshifted by 47,400 km s^{-1}. This left the object to be either an extremely dense star with a radius less than 10 km with a strong gravitational redshift or an active galactic nuclear region at extragalactic distances. Greenstein & Matthews (1963) showed another strong radio source, 3C48, to have lines with a redshift of 0.37 and arrived at a similar conclusion. One year later, Greenstein & Schmidt (1964) published a paper discussing these two objects in great detail, where many of the concepts we use to describe AGN originated.

Seyfert galaxies were identified years prior when they were discovered by their name-sake, by using emission lines in spectra. (Seyfert 1943). Seyfert galaxies are relatively nearby, mostly spiral galaxies that host AGN. Intensive studies over the past few decades lead us to believe that a supermassive black hole with an accretion disk lies at the core of every active galaxy and is the engine driving the activity. Seyfert galaxies, unlike quasars, are typically close, with redshifts $z \lesssim 0.1$, and have moderate bolometric luminosities ($\sim 10^{45}$ ergs s^{-1}). Over time scales ranging from

days to years, Seyfert galaxies show variations in UV continuum luminosity over a factor of up to ∼10 in amplitude (e.g. Dunn et al. (2006)).

Seyfert galaxies are divided into two basic types, 1 and 2 (Khachikian & Weedman 1974). Seyfert galaxies are best classified by their strong emission lines such as Hα, Hβ and [O III] $\lambda\lambda$4959, 5007. Seyfert 1 galaxies show both broad permitted emission lines (>5000 km s^{-1}) and narrow permitted and forbidden lines (∼500 km s^{-1}) as shown in Figure 1.1, while the UV and optical spectra of Seyfert 2 galaxies are devoid of broad emission features in unpolarized light. Beyond differences in emission lines, Seyfert 1 and 2 galaxies differ in continuum flux. A Seyfert 1 galaxy, as shown in Figure 1.1, has a rising continuum towards the blue, which we attribute to the accretion disk. A Seyfert 2 galaxy's spectrum is flat accross the optical and has prominent stellar absorption features from the host galaxy.

Osterbrock (1989) divides Seyfert 1's into more subtypes. He classifies Seyfert galaxies that show both narrow lines and broad lines for the permitted H I series as Seyfert 1.5. Those galaxies that show weak broad line components and strong narrow components for both Hα and Hβ are Seyfert 1.8s, while those that show only weak broad Hα are 1.9s. This gives a broad spectrum of types between Seyferts 1 and 2.

In order to explain this physically, we interpret the range of properties as a geometric observing effect. The standard unified model, seen in Figure 1.2, illustrates what we think is at the heart of every AGN. We believe that there is a supermassive black hole (SMBH). The SMBH is surrounded by an accretion disk of gas (not seen in

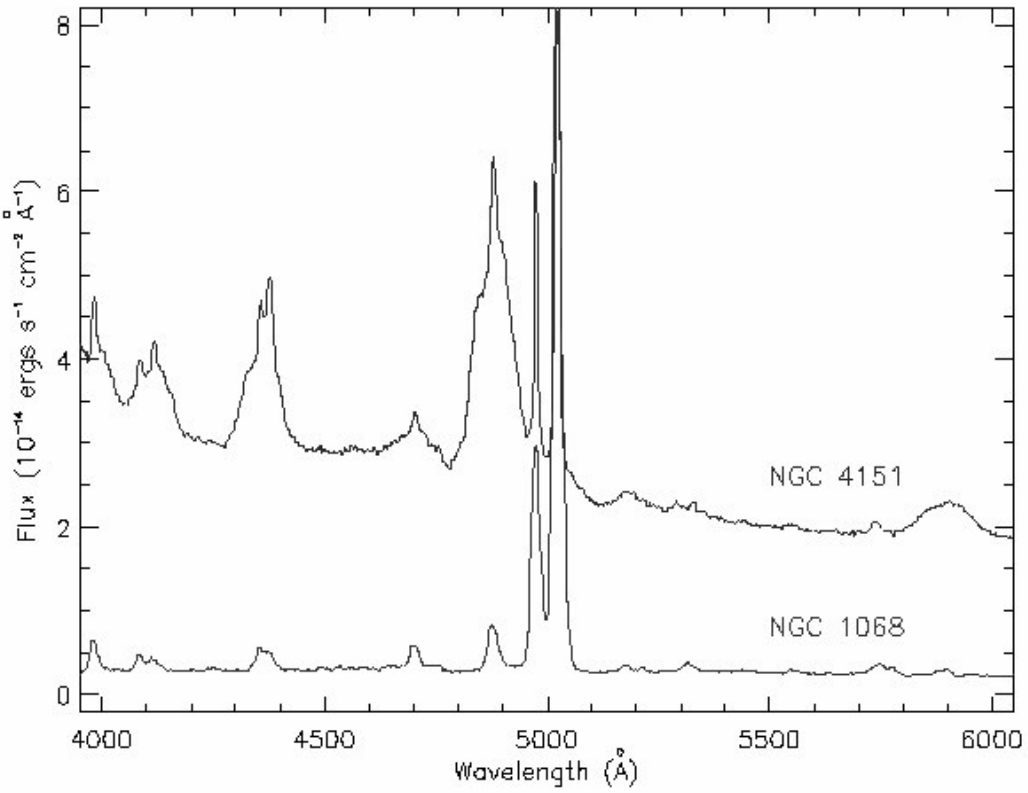

Figure. 1.1: Top: Spectrum of NGC 4151 in the optical. We see broad Hβ and broad Hγ at 4861 Å and 4340 Å respectively. At 4959 Å and 5007 Å are the narrow [O III] lines. Bottom: Spectrum of NGC 1068 with no broad lines and narrow Balmer series and [O III] forbidden lines.

Figure 1.2), which is the presumed source of the power law spectrum for the optical, UV and soft X-Ray portions of the spectral energy distribution (SED) seen in Figure 1.3. The orientation based observational effect is due to the putative dusty torus that can eclipse the Broad Line Region (BLR) clouds, which have densities on the order of $n_H \approx 10^8$ to 10^{11} cm^{-3} (Oseterbrock 1989), where n_H is the number density of hydrogen. From a viewing angle along the torus axis, we see the accretion disk and broad line clouds directly, and we see broad emission lines for only permitted lines due to the higher densities resulting in a Seyfert 1. This effect is due to collisional

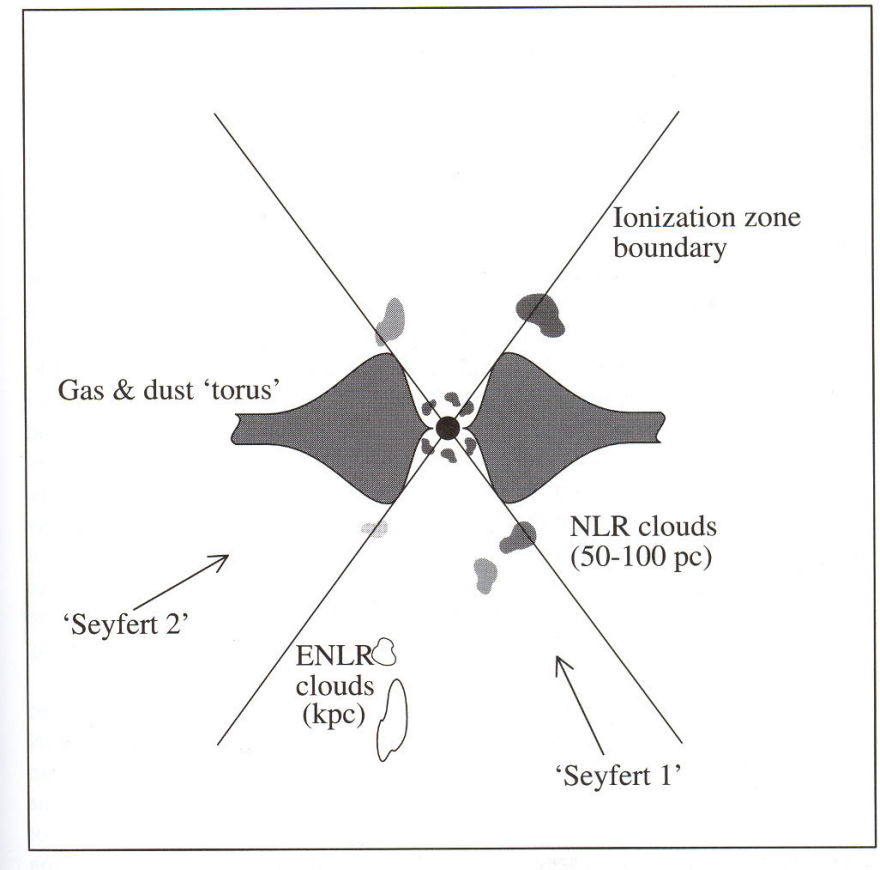

Figure. 1.2: Standard unified model of the AGN from Peterson (1997). The SMBH, accretion disk and the BLR are inside of the dusty torus.

dexcitation of the forbidden lines. If we observe at an angle close to the torus equator, the BLR is obstructed and we find that we see only the reflected light from the Narrow Line Region (NLR) clouds or hotter gas further out. These clouds are lower density than the BLR clouds ($n_H \approx 10^3$ to 10^6 cm^{-2}) so both permitted and forbidden lines are present.

This model was initiated by Antonucci & Miller (1985). Using a spectropolarimeter on the Lick 3-m Shane telescope, they compared spectra of the classic Seyfert 2 NGC 1068 in direct light with spectra in polarized light, as shown in Figure 1.4. The

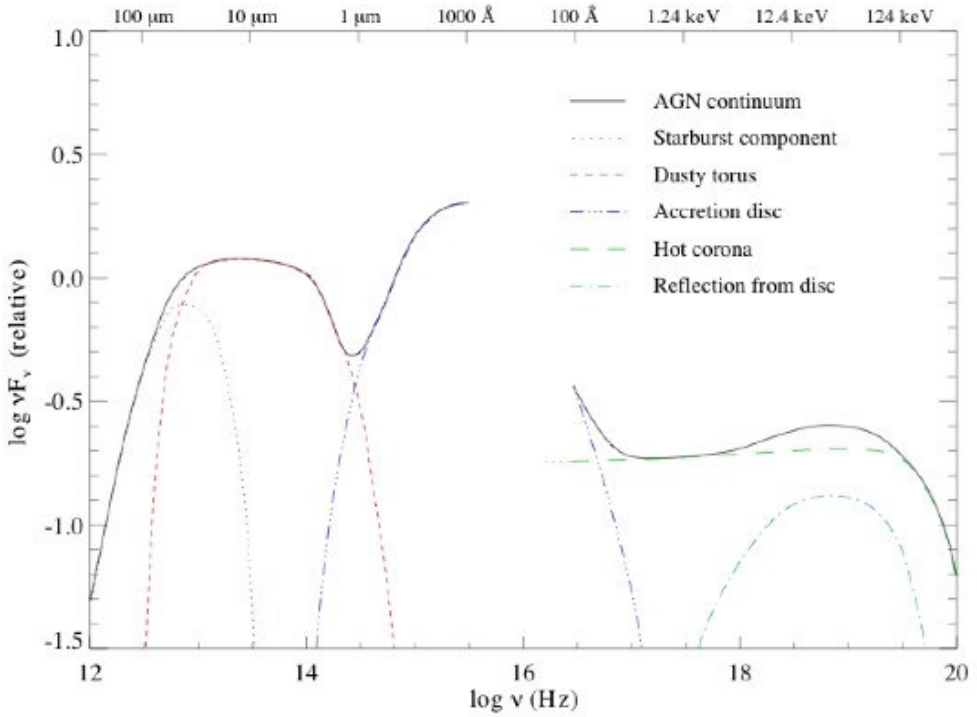

Figure. 1.3: The observed SED for a typical Seyfert galaxy with various individual components labeled. The gap between log$\nu\approx$15.5 and 16.5 Hz is due to our inability to observe in the EUV due to absorption by hydrogen.

results showed that in polarized light a Seyfert 2 looked like a Seyfert 1, due to the reflected light from the NLR.

1.2 Intrinsic Absorption History

Oke & Sargent (1968) found that while the optical spectra of Seyferts have absorption features, which were previously attributed to stars, there also was a He I line in NGC 4151 that was likely due to self-absorption. Anderson & Kraft (1969) found 3 kinematic components within the He I and hydrogen Balmer absorption lines that showed blueshifts, relative to the rest frame, of -280, -550 and -840 km s^{-1}. They

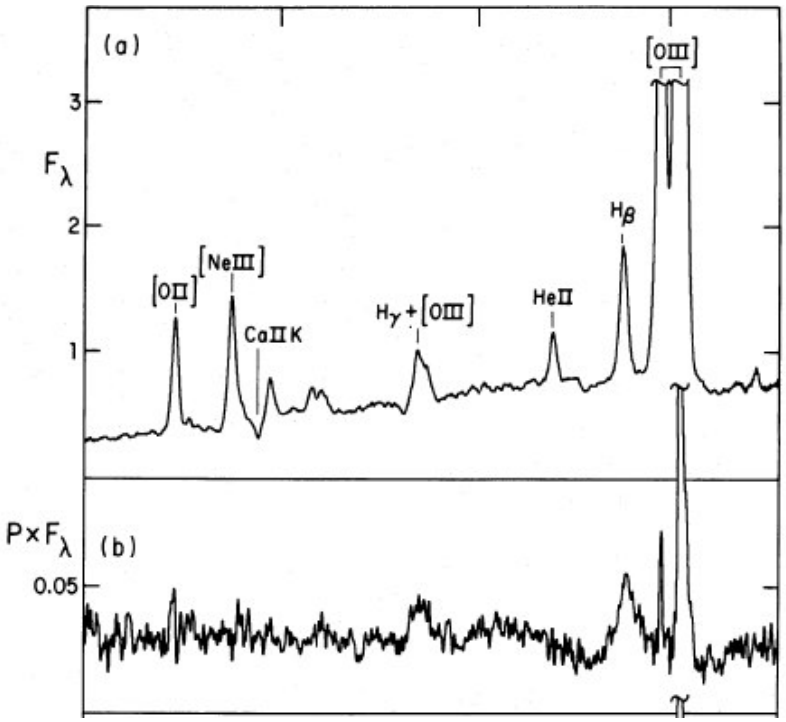

Figure. 1.4: Spectra from Antonucci & Miller (1985) Top: Spectrum of NGC 1068 in the optical with narrow lines. Bottom: Spectropolarimetry of NGC 1068 showing Hβ and Hγ as significantly broader lines.

attributed these features to an outflow of gas from the core with multiple kinematic components. Thus, these absorption lines are 'intrinsic' to the active nucleus.

Variable absorption features were first noticed by Cromwell & Weymann (1970). Their spectra showed that the lines were not visible in a 1962 observation by Sargent (shown in Figure 1.5). They attributed the appearance of the lines to an explosive event. While this was an important discovery, we discuss later that the absorption can be variable but can also be static over large timescales.

In data from the *International Ultraviolet Explorer (IUE)*, Ulrich et al. (1988) found that only 3 to 10% of Seyfert galaxies showed intrinsic absorption in high-

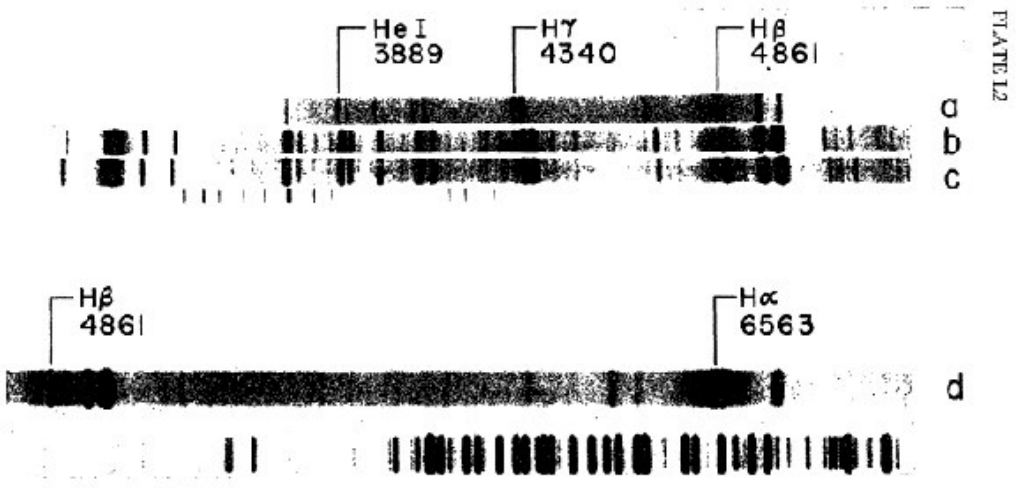

Figure. 1.5: Photograph of the spectra taken of NGC 4151 that show variability in the absorption lines (Cromwell & Weymann 1970).

ionization lines (C IV & N V). With IUE's resolution of only ∼6 Å Full Width at Half Maximum (FWHM), it turns out that many intrinsic absorption lines were not detectable, which we see many more cases of intrinsic absorption in higher resolution spectra.Thus, their estimate for the frequency of Seyfert galaxies with intrinsic absorption turned out to be a severe underestimate.

In a *Hubble Space Telescope* (*HST*) study by Crenshaw et al. (1999), they found that 3-10% fraction number was far too low due to the low resolution of *IUE*, and that the percentage of Seyfert galaxies that showed intrinsic C IV absorption was closer to 60%. All of the intrinsic absorption in these moderate-luminosity AGN was in the form of Narrow Absorption Lines (NALs) with velocity widths <500 km s^{-1}. Their survey, however, had only 17 objects and possibly contained some selection biases. It did show that intrinsic absorption was much more prominent in Seyfert 1 galaxies than previously thought, and that further study is required of this phenomenon to

more fully understand the central engine in AGN. Crenshaw et al. also showed a 1:1 relationship between the presence of UV and X-Ray absorbers, based on X-ray data from George et al. (1998) & Reynolds (1997). X-Ray studies also estimated a global covering factor for Seyfert galaxies of ∼0.5.

Broad Absorption Line (BAL) quasars have been studied even more extensively. These objects show much larger velocity widths, up to ∼10,000 km s^{-1} (Weymann et al. 1981; Turnshek et al. 1988) and they appear in ∼ 10% of all quasars (Foltz et al. 1990). This is a much smaller percentage than for narrow absorption lines, so global covering factor of the central source is an important consideration in determining their nature.

Laor & Brandt (2002) surveyed 50 AGN that included both quasars and Seyfert galaxies, and both NALs and BALs. Their survey found that 44% of the AGN showed C IV absorption with an equivalent width (EW) greater than 0.1 Å. Also, they looked for various trends concerning intrinsic absorption in data from the *HST* and the *IUE*. Their survey was derived from the PG quasar sample of Boroson & Green (1992). One of the more notable trends they found was a dependence of maximum outflow velocity on luminosity ($v_{max} \propto L^{0.62\pm0.08}$). Their plot contains both BAL and NAL lines. They found that the EW also increased with increasing luminosity. This trend is based on Soft X-Ray Weak Quasars (SXWQs), which show larger values of EW and v_{max} than any other quasar group across the luminosity span. They also showed that O [III] emission EW and v_{max} are correlated, with SXWQs showing a significant

correlation of EW vs. v_{max}. Of the 56 objects they investigated, 28 showed intrinsic UV absorption. This agrees well with the ∼60% Crenshaw et al. (1999) found in the lower luminosity sample.

To investigate these properties in a purely BAL sample, Ganguly et al. (2007) used data from the Sloan Digital Sky Survey to investigate their properties. They found in a sample of over 5000 objects that the overall fit between maximum velocity and luminosity found by Laor & Brandt applies to their sample, as shown in Figure 1.6.

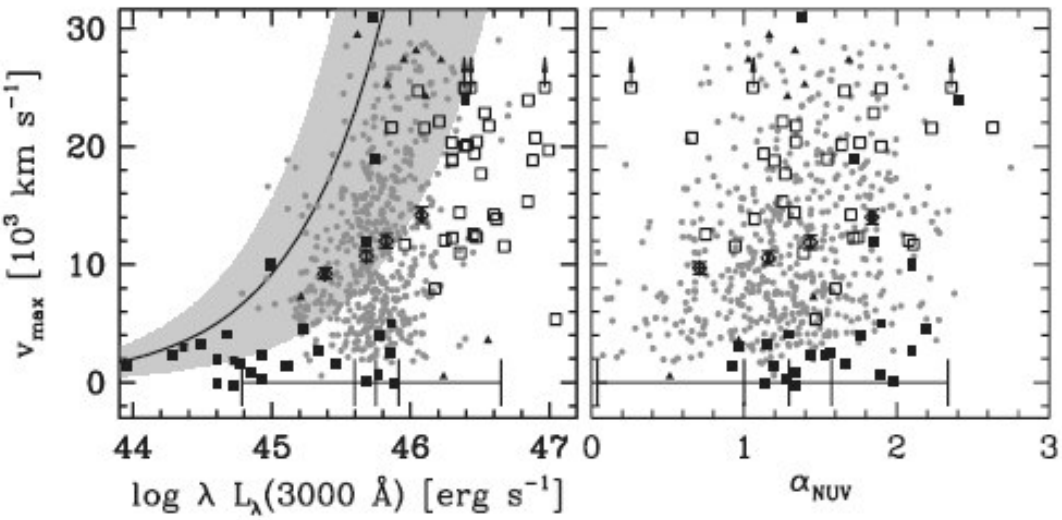

Figure. 1.6: Taken from Ganguly et al. (2007). Left: Plot of maximum velocity of absorbers versus the specific luminosity. The filled squares are taken from Laor & Brandt (2002) the trend is also taken from Laor & Brandt. Right: Plot of EW versus α_{NUV}, where α_{NUV} is the power law slope of the UV continuum.

1.3 Previous Intrinsic Absorption Variability

Our knowledge of variability for intrinsic absorption is limited. Variability is important because it is our only link to several key parameters concerning AGN. In data from *HST*, absorption variability was seen by Crenshaw et al. (1999) in Seyfert galaxies. Nearly all of the variability has been attributed to changes in the ionic column densities, which was assumed to be due to changes in ionizing flux from the continuum source. However, in 4 Seyfert galaxies (NGC 3516, NGC 3783, NGC4151, & NGC 5548) bulk transverse motion of gas across the line of sight was identified as another culprit for column variations (Crenshaw et al. 2003). In the bright Seyfert galaxy NGC 4151, both ionization change and bulk transverse motion were detected. Kraemer et al. (2006) performed a detailed analysis of the absorption from Space Telescope Imaging Specrograph (STIS) data. For the component they dub D+Ed, they find a lower limit to the transverse velocity of $v_t \geq 2100$ km s^{-1}, similar to other lower limits found in Seyferts (Crenshaw et al. 2003).

NGC 3783 has been shown previously to be variable. In 1993 February data from *HST*, NGC 3783 showed a spectrum with no narrow intrinsic absorption. By 1994 January, two obvious absorption features arose for each member of the C IV doublet. By 2000 February another pair of absorption lines had emerged. Gabel et al. (2003) showed that the radial velocity changed as well. In a series of several spectra the radial velocity of one of the kinematic components was seen to have changed over two time spans. The first gave a change of $\sim$35 km s^{-1} and in the second span they saw

a change of ~ 55 km s^{-1}. This is the first well documented case of a change in radial velocity for an intrinsic absorber in a Seyfert galaxy.

Transverse velocity was also measurable in NGC 3783, where they found a lower limit of $v_t \geq 542$ km s^{-1}, which is comparable to the radial velocity (-450 km s^{-1}). The first detection of transverse velocity in NGC 3783 was by Maran et al. (1996), where they estimated $v_t \geq 3000$ km s^{-1}, much higher than v_r.

1.4 Dynamical Models

The penultimate goal of our research is to understand the general dynamics of mass outflow and thereby to ultimately help complete the picture of the AGN central engine. Several dynamical scenarios have been offered as explanations for the outflow (see Crenshaw et al. 2003 for a review of the models).

One mechanism, Compton-heated winds, assumes that EUV and X-Ray photons from the inner accretion disk are irradiating the gas at larger distances and creating a thermal wind (Begelman et al. 1983). The disk irradiation can happen via any one of three different scenarios: the continuum source is above the disk; X-Rays are scattered onto the surface of the disk; or, the height of the disk increases faster than 1/R (Shakura & Syunyaev 1973).

The thermal balance in the disk is maintained by line cooling and recombination. If the ionization parameter (U) is high enough, line cooling becomes more difficult and the gas heats. Then Compton heating and inverse Compton cooling come into

play; this region is seen vertically extending from the disk as a hydrostatic corona. If the sound speed is less than the escape speed, which is dependent on the black hole mass and distance, then the gas can form a thermal wind beyond a certain radius (which is proportional to the black hole mass and inversely proportional to the temperature necessary for Compton heating and cooling). There is a 'characteristic temperature' that defines a critical luminosity. When the escape temperature equals the Compton temperature and this characteristic temperature, we see that there is a critical luminosity, which is proportional to the Eddington Luminosity (L_{Edd}), which can be used to define the wind's effectiveness in overcoming the gravitational potential. Thus, L/L_{Edd} should be a good proxy for the velocity of the wind.

Krolik & Begelman (1986, 1988) showed that, instead of using gas from the accretion disk itself, gas from the putative molecular torus could be the source for the outflowing wind. In this case, a luminosity greater than $0.08L_{Edd}$ would be sufficient to provide winds with velocities of hundreds of km s^{-1}.

Radiative driving is also a promising method to explain fast moving outflows such as BALs (Arav et al. 1994). This model requires that a gas be forced out with an acceleration due to radiation pressure. The terminal velocity is derived from this equation of motion and can be high enough to explain velocities seen in BAL-like flows.

The efficiency of radiative driving can be increased significantly by dust. The dust increases the effective opacity and allows the radiative pressure term to outweigh the

gravitational term, which is important for sub-Eddington luminosity objects. The problem is that the dust cannot exist near the continuum source, unless the UV radiation is attenuated (Emmering et al. 1992).

Another possibility is that magnetic fields from the accretion disk are lifting plasma from the disk in magneto-hydromagnetic flows, where the plasma follows helical magnetic field lines (Blandford & Payne 1982). The ionized gas in the accretion disk corona is trapped by magnetic field lines generated from the disk. As the disk revolves around the SMBH, the gas is spun outward carrying away centrifugal energy, which allows the gas in the disk to continue spiralling inwards and feeding the SMBH. Depending on how far from the central core these clouds can follow the field lines, this could also be an explanation for the high transverse velocities.

Our impetus for this work stems from these models. We seek to help constrain the observable traits of Seyferts and other low-z AGN, and to aid in determining which of these models or combination of these models best defines the situation. At present we need more observations with multi-wavelength coverage with significant time resolution for variability studies to provide model constraints such as densities, mass-loss rates and locations of the absorbers (Crenshaw et al. 2003).

Lead the way, toots.

—— Elias Koteas (TMNT)

– 2 –

The Far Ultraviolet Spectroscopic Explorer

2.1 The Instrument

FUSE was a Principle Investigator class mission. It was launched on 1999 June 24 and operated until 2007 August 17, when the final reaction wheel failed. It covered the far ultraviolet regime (∼900-1200 Å) of the electromagnetic spectrum and observed objects ranging from planets to the Interstellar Medium (ISM) to AGN to the Intergalactic Medium (IGM) at high resolution ($\lambda/\Delta\lambda \approx$ 20,000). The three main goals for FUSE were to put constraints on the abundance of deuterium in galactic environments with varying metallicites and evolutionary histories, to survey the O VI doublet in the halo and disk of the Milky Way along with the Large and Small Magellanic Clouds, and to explore the distribution and basic properties of the IGM (Sahnow et al. 2000).

FUSE was launched with four reaction wheels, which provided a pointing accuracy of 0.2-0.3 arcsec. In 2001, two of those died, decreasing the pointing accuracy. Three years later a third reaction wheel ceased functioning. Attitude control was still possible using the magnetic torquer bars, by using the earth's magnetic field to point the telescope with reasonable acuracy above declinations of 45°. This method became

unstable when the final reaction wheel failed.

The spectrograph is a Rowland circle design (shown in Fig 2.1) that had a diameter of 1652 mm. The telescope is designed with four off-axis parabolic mirrors in order to reduce cost, each with a diameter of 4 inches. Each mirror is equiped with a tip-tilt stepper motor. With four mirrors, *FUSE* defines four channels, each with one mirror, one Focal Plate Assembly (FPA), one diffraction grating and one-half of a far-UV detector.

Two mirrors are covered with lithium flouride (LiF) plus Al while silicon carbide (SiC) was used on the other two mirrors. The LiF coating provides nearly two times the reflectivity of the SiC coating at wavelengths greater than 1050 Å, and very little reflectivity at less than 1020 Å. The bandpass for each side of the channels is ∼200 Å, with a total coverage of 290 Å (see Table 2.1). *FUSE* has no onboard calibration lamp. In order to calibrate the spectra, there is a template based on several astronomical objects for the dispersion solution.

Table. 2.1: Wavelength Coverage

Channel	Seg A		Seg B	
	Min λ	Max λ	Min λ	Max λ
SiC 1	1003.7	1090.9	905.0	992.7
LiF 1	987.1	1082.3	1094.0	1187.7
SiC 2	916.6	1005.5	1016.4	1103.8
LiF 2	1086.7	1181.9	979.2	1075.0

In order to keep pointing for the spacecraft optimal, the positive x side of the craft

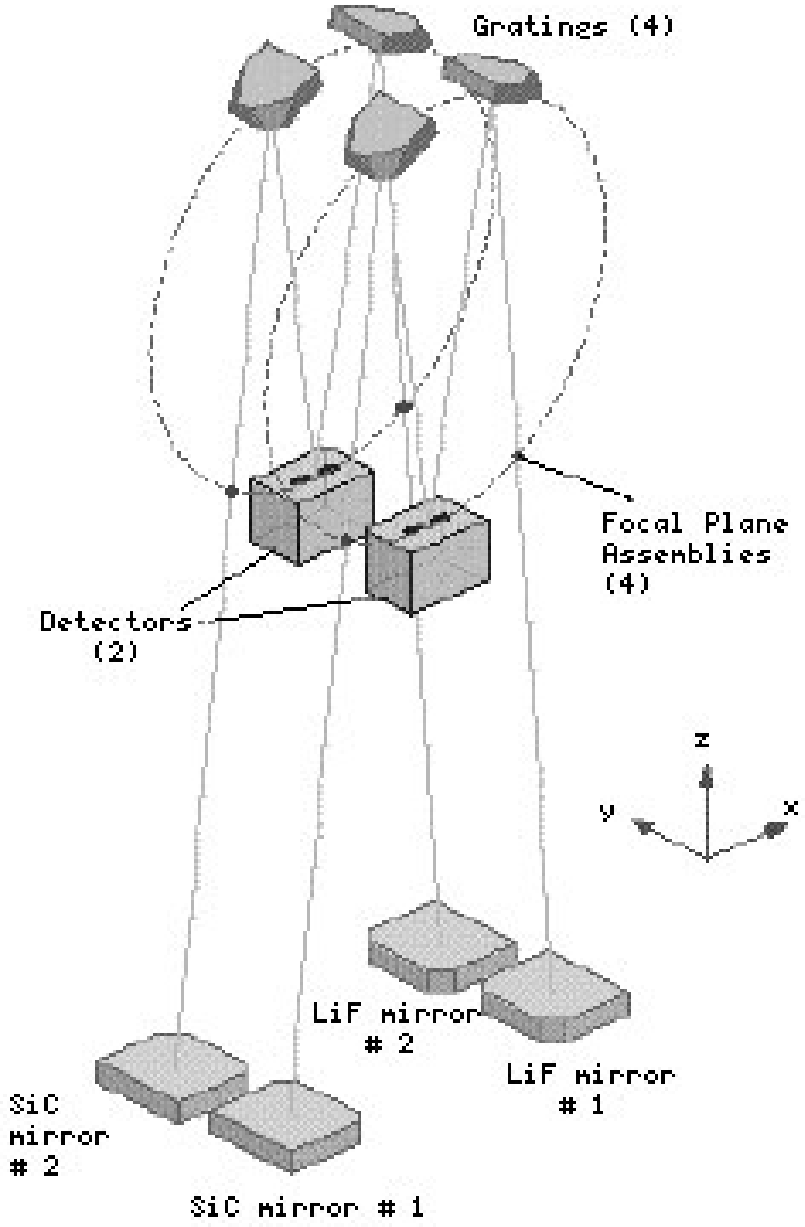

Figure. 2.1: The Rowland Circle design of the *FUSE* spectrograph is defined by the dashed lines where the gratings and detectors sit. The gratings are curved to match this circle. The x and y directions are important for the stray sunlight that can affect the spectral images (Sanhow et al. 2000).

in Figure 2.1 (LiF) was nominally kept in the shade during observations. Primarily this was to aid the Fine Error Sensor (FES) in pointing the telescope. The FES is an

optical camera; thus any stray light would adversely affect an observation. This also reduces the geocoronal dayglow effects in LiF spectra (Feldman et al. 2001), which we will discuss later.

WD0439+466 was used to determine the spectrograph's resolution. This object is a nearby white dwarf with H_2 ISM lines in its spectrum that could be easily measured and plotted in a curve of growth to find the thermal velocity parameter. The ultimate result was that they obtained a resolution power of 20000 $\pm$ 2000 by deconvolving the measured line widths.

The Focal Plane Assemly (FPA) was made up of an optical flat mirror mounted on a 2-axis flight adjustable stage. It was placed at the focus for each mirror and acted as an optical entrance aperture for each channel. The mirror was cut in four places for the four different available apertures shown in Figure 2.2 and Table 2.2. The LWRS was the standard aperture used for most observations. The telescope provided a Point Spread Function (PSF) of 90% in 1.5 arcsec. The CCD FES camera was mounted above the mirror to receive the reflected light and thus was able to provide pointing information.

Table. 2.2: Aperture Descriptions

Aperture	Keyword	Dimentions (arcsec)	Throughput (approx.)	Throughput LiF2 (approx.)
large square	LWRS	30 × 30	1.00	1.0
medium rectangle	MDRS	4.0 × 20	0.98	0.7
narrow rectangle	HIRS	1.25 × 20	0.85	0.15
pinhole (N/A)	PINH	0.5 (diameter)	0.10	

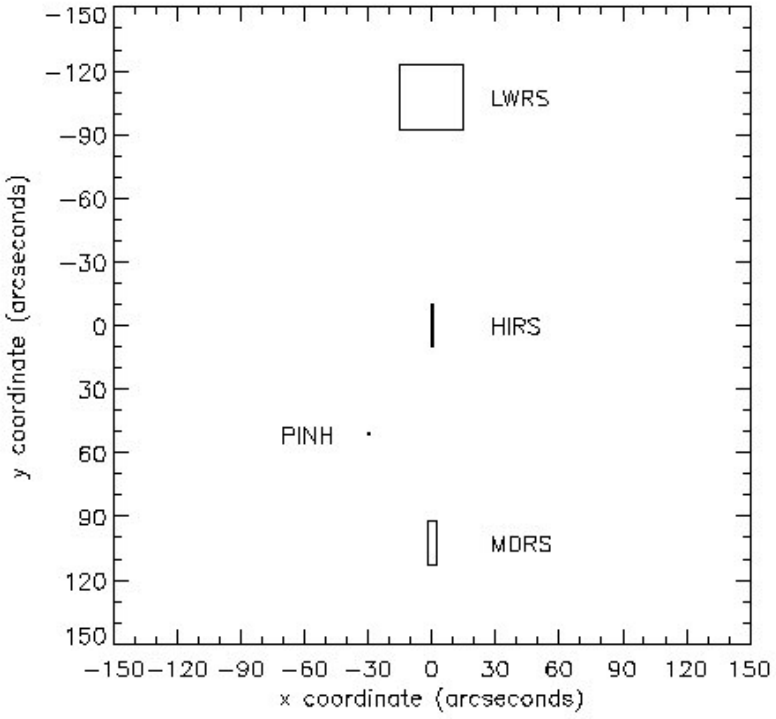

Figure. 2.2: This shows the layout of the mirror cuts that *FUSE* uses for apertures. The largest aperture (LWRS) is the most commonly used aperture, while the pinhole (PINH) was not used for science data.

There are two detectors for the four channels, one for each coating. These detectors are microchannel plate detectors (MCPs), labeled 1 and 2, which cover a total of 170 mm × 10 mm and allow for full coverage of the desired spectral range from a pair of SiC and LiF mirrors. The detectors are split in two segments, labeled A & B, with a 7 mm spacing between them. Thus, one observation provides 8 different spectra; four mirrors reflect light to gratings with 2 segments apiece. The MCPs are stacked in the Z direction (as shown in Figure 2.1), have pores of 10μm widths and have a ratio of pore to detector length of 80:1 (Siegmund et al. 1997). The MCPs pores are

curved cylindrically (R=0.826mm), which matches the Rowland circle (Siegmund et al. 1997) and are fed by electron cascades delivered by KBr opaque photocathodes. The charge clouds are drifted over a 6mm gap to the delay line anode. The X and Y positions are determined from the arrival delay times and the ratio of charges at the two ends of the anode respectively.

For time-tag (TTAG) mode, the detectors record a photon event as a 4-byte packet. The packet contains the detector ID (number and segment), the X and Y positions on the detector and the pulse height of the event. The packet is sent to the Instrument Data System (IDS) for recording. Output to the IDS cannot exceed 32,000 cnt s^{-1}, or else random photon events will be lost, thereby corrupting the photometric accuracy of the data. Because of this limitation, *FUSE* can only observe faint objects in this mode. Seyfert galaxies and quasars are all safe targets for time-tag mode. In the other available mode, histogram, the data are binned by 8 pixels in the Y direction, thus reducing the amount of information sent via the onboard bus.

The background for *FUSE* has only two components. These are intrinsic contamination from the spacecraft and geocoronal emission. The primary source of spacecraft contamination is due to the ^{40}K radioactive decay from the glass within the craft. The geocoronal emission is from ionization of atoms surround the earth by sunlight and subsequent recombination. These appear as bright lines compared to the continuum in the spectrum at specific wavelengths (Feldman et al. 2001). An example of this is seen in Figure 2.3. The strong sharp line at 1026 Å is due to geocoronal Lyβ. Be-

cause it is difficult to determine the background for an individual science observation, a uniform intrinsic background image imposed on a scattered light image has been created for subtraction. This subtraction is more accurate for TTAG mode than for histogram mode.

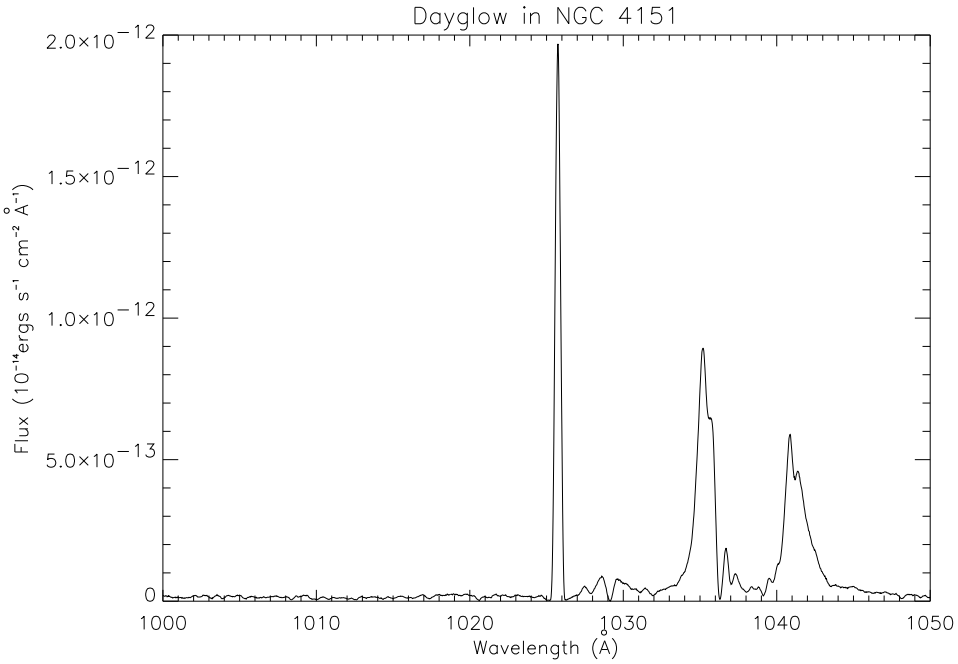

Figure. 2.3: Coadded spectrum for NGC 4151. We see the O VI doublet $\lambda\lambda$ 1031.93, 1038.62 in emission from the NLR and the geocoronal Lymanβ line at λ1025.72

In order to improve the quantum efficiency of the MCPs, two sets of wire grids are located above each MCP. One grid is designed to collect photoelectrons created from the MCP, the other is a 'plasma grid' intended to remove effects from geocoronal high altitude plasma; however, these wires can impede the photons path in the channel. The resultant spectrum has a warp or curvature that is not intrinsic to the object. The most famous case of this occurs in the LiF 1b spectrum (which we do not use in

our observations) seen in Figure 2.4.

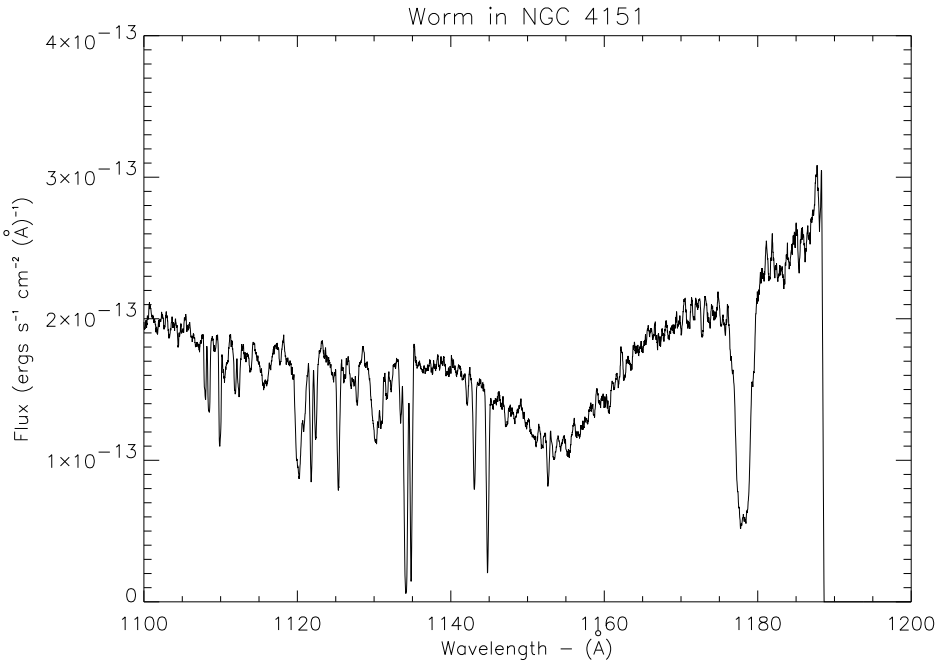

Figure. 2.4: The broad feature between 1140 and 1170 Å is the 'worm' feature created by the wire grid above the MCP.

2.2 CalFUSE

CalFUSE is the program created by Johns Hopkins University to reduce data from *FUSE*. It is a C based program available for Linux, Solaris and Mac. Both the raw data and the preprocessed data are available on the Multimission Archive at Space Telescope (MAST) for download. The majority of the data have been processed using CalFUSE 3.0; MAST is currently making efforts to reprocess the data with the latest version, CalFUSE 3.2. Because not all of the data were up to date with the most current version of CalFUSE, and this improvement would not be completely finished

until late 2007, we decided to download the raw files we needed and to process them directly with CalFUSE 3.2.

CalFUSE 3.2 applies several corrections to the raw data we download from MAST. The principle of the programming is to walk backwards from the detection on the microchannel plate through the steps a photon takes through the instrument on arrival. The file headers contain several flags that inform CalFUSE what steps are recommended. However, the operator may elect to run any process from the command line. We followed the suggested flags.

For our time-tag data, CalFUSE selects the X and Y positions on the detector, the time of arrival and the pulse height for each photon event. It looks for what are dubbed 'good-time' intervals, which are defined by the observing circumstances. During the time frame it records status flags, spacecraft position, detector high-voltages and count-rates.

The first module called by CalFUSE is a program to correct the inflight reference frame of *FUSE* or Flight Alignment Reference Frame (FARF), thus starting with the end of the photon's flight path. There are two particular effects that this module corrects, the dead-time effects and the X and Y position problems.

Dead-time refers to the period between a photon arrival and the detector recording the event. During this time, the detector is 'dead' to arriving photons. If many events come too quickly, some photons are neglected. This is corrected by the Front End Counter (FEC), which is a separate detector placed at the detector anode that simply

measures photon counts. By comparing the count from the FEC to the count recieved by the Instrument Data System (IDS), a correction can be applied to the spectrum based on the ratio (always ≥ 1.0).

The XY positions of the photons can be affected by several things. These positions are calculated based on the time of the detection and the voltage measurement associated with the incoming charge cloud (Siegmund et al. 1997). The position of arrival is often altered by the temperature of the MCPs. To correct for this, *FUSE* has 'stim' lamps that provide pulses outside of the spectral region at known locations.

The Y scale can be affected by the count-rate. As the detector recieves more photon events, the Y range is widened due to the method of detection mentioned in §2.1. This can be corrected using known bad pixel positions tabulated in the the Y direction as a function of count-rate.

Geometric distortions of the MCPs can cause what appear to be 'wiggles' in the image. These can be mapped and corrected with the two wire grids above the detector that are shadowed on the detector from the 'stim' lamps above.

The pulse height of the X values becomes distorted after a time. When there are too many events the detector is affected by 'gain sag'. This leads to a systematic X miscalculation across the detector. This effect is seen strongest near the Lyβ geocoronal dayglow line. To corect for this, a set 'stim' lamp image is available with only one pulse height which can be stepped across the image in the X direction and used to thereby align the shadow.

There are two detector effects that the module is unable to correct. The 'worm' that affects the LiF 1b (§2.1) and other 'worms' that appear from time to time are not constant and do not appear to be related to any measured quantities; thus they are uncorrectable. The other problem is that *FUSE* is unable to make flat-field images. This is often averaged out across the image due to spacecraft, grating, and mirror shifts, and seems mostly to affect only the brightest targets.

Module 2 screens specific photons or flagged photons. It minimizes the amount of airglow, by excluding data taken from targets near the earth's limb due to a higher amount of geocoronal emission recieved in those orientations. During passages through the South Atlantic Anomaly, where the earth's magnetic field is diminished, the voltage on the detector is lowered to prevent damage to the instrument. Module 2 also corrects this based on a model derived from observations in the first three years of operation. It eliminates event bursts, which are random detections of large count rates over a short period of time.

The second module also corrects photons by flagging times when the object falls out of the aperture. The user has the option for this module to select certain time intervals to use and exclude others. Flags are set for these times. After all the flags are set, the program copies the valid photon events and writes them to file.

The third module removes various motions from the spectrum. First it locates the spectrum and asigns the photons to individual channels. It then corrects for grating, FPA, mirror and spacecraft motions. The last two corrections are not applied to

extended sources. Once this step is done, the next module moves on to wavelength calibrations. First it corrects for the astigmatism of the mirrors. The wavelength scale is a predetermined solution that is applied to each segment. It finally corrects for the doppler motion of the spacecraft and makes the final correction to the heliocentric observation frame.

Once wavelength has been calibrated, another module calibrates the flux levels. The flux is calibrated based on a table of effective areas. The program calculates each photon's 'flux density', E, in ergs cm^{-2} via:

$E = \frac{Weight \times hc}{\lambda A_{eff}(\lambda)}$,

where h is the Planck constant, c is the speed of light, λ is the wavelength and A_{eff} is the effective area (Feldman et al. 2001). Finally, after flux calibration, the spectrum is extracted for each segment.

We incorporated CalFUSE 3.2 into our pipeline for processing to facilitate data analysis. Master Routine v3.0 was written by Jay Dunn and calls CalFUSE to do the aforementioned data reduction and calibration. The outputs for CalFUSE are calibrated FITS files for each detector and segment and exposure. Each observation of a target is broken up into a number of exposures (as many as 35 separate exposures). Master Routine takes the fits files and converts them to a more IDL friendly format. The exposures are coadded based on exposure time and saved as individual segment and detector spectra. Next it coadds each of the detector segments (minus the LiF 1b segment, which is corrupted by the worm) weighted by exposure time. Afterwards,

due to target misalignments, we found it necessary to examine each spectrum and manually scale the spectrum to match the LiF 1a spectrum in the range between ∼1050 and 1080Å. We opted to match the LiF 1a spectrum because it was used for primary alignment for the object and because the LiF had a higher reflectivity, giving a better signal-to-noise.

Complete data analysis is essential for the synthesis of successful strategy.

—— *Anonymous*

– 3 –

FUSE Analysis of Intrinsic Absorption in NGC 3516: A Case Study

3.1 Introduction

NGC 3516 (z=0.0088) is a well studied Seyfert 1 galaxy that has been shown in the past to exhibit intrinsic UV absorption (Crenshaw et al. 1999; Kriss et al. 1996). This absorption was first seen in IUE spectra by Ulrich & Boisson (1983). Kriss found O VI $\lambda\lambda$ 1031.9, 1037.6 absorption in data taken with the Hopkins Ultraviolet Telescope (HUT). Crenshaw et al. found in Goddard High Resolution Spectrograph (GHRS) data that NGC 3516 showed multiple components in Lyα, C IV, Si IV and N V. This target has also been known to show variability in the absorption lines (Begelman 1987; Kraemer et al. 2002), which makes it an excellent choice for a test case for a *FUSE* survey.

We obtained 2 new spectra of the Seyfert 1 galaxy NGC 3516 on 2006 February 9 and 2007 January 23 with the Far Ultraviolet Spectroscopic Explorer. These new spectra were obtained because X-Ray data showed that the flux state of NGC 3516 was increasing from an historically low state. They provide us with the only high resolution spectra of NGC 3516 in the far ultraviolet range with a significant signal-

to-noise ratio, each 1.5 times higher than the 2000 April *FUSE* spectrum, which had the previously highest S/N and was the most useful of the four previous observations.

3.2 Lightcurve

We followed the method used by Dunn et al. (2006) to generate a continuum flux lightcurve for NGC 3516 in the far UV. Over a range of wavelengths between 1110 Å and 1130 Å, we measured the average flux. We chose this range due to the lack of H_2 interference and the absence of flux from the broad line region of the O VI doublet. The 2006 February observation appeared to have little to no increase in continuum flux from the 2000 April observation. The 2007 January observation however showed significant increase in flux by $\sim$2 times.

The UV lightcurve for NGC 3516 was generated for the web-based database in Dunn et al. (2006) using all available *IUE* and FOS spectra. Using this lightcurve, we added points from HUT, STIS and the GHRS. The wavelength center position for the measurements for observations from each of these spectrographs was at 1460 Å. Because *FUSE* does not have coverage at 1460 Å we used the data from STIS which was taken near the same time as the *FUSE* spectra and covers both 1120 Å and 1460 Å. From the ratio between the two STIS and *FUSE* observations we find a scale factor for all of the *FUSE* data of 1.05. This lightcurve is shown in Fig 3.1.

X-Ray studies have shown that NGC 3516 was in a significant state of increase over the past few years. Unfortunately due to the failure of the last *FUSE* reaction

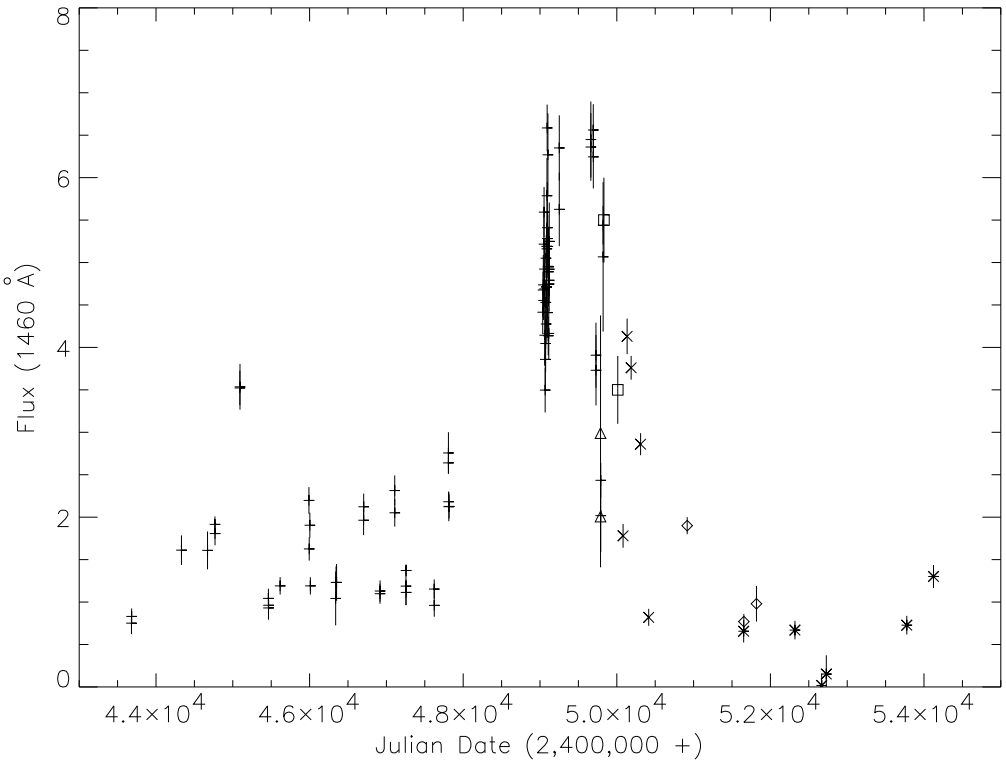

Figure. 3.1: Light curve for NGC 3516. Pluses are *IUE* data, ×s are FOS, squares are GHRS, triangles are HUT, and the diamonds are STIS data all taken in the 1460 Å range, while the asterisks are FUSE data from the 1120 Å range. We plotted the FUSE with the other datasets to get an overall view of where the flux state was.

wheel, we are no longer able to obtain UV spectra until the installation of the Cosmic Origins Spectrograph (COS) on *HST*. The increase we have seen over the past two observations is important because it suggests that we may be able to obtain high resolution far-UV spectra of this object in the future with COS, while it is in its highest state (seen in the *IUE* portion of the lightcurve).

3.3 H_2 Fitting

Many studies have been focused on ISM and molecular hydrogen (H_2) absorption features in *FUSE* data (Wakker 2006; Gillmon et al. 2006). In order to fully characterize the intrinsic absorption in our targets, we must ensure that this contamination is either removeable, insignificant or does not affect the wavelength regimes of interest.

Following the methods set forth by Gillmon et al. (2006), we attempted to define the column densities of H_2 gas in our line of sight through the galaxy to the object. H_2 molecules exhibit lines in the ultraviolet due to Lyman and Werner rovibrational transitions. Lyman transitions are from the ground electronic state ($X^1\Sigma^+{}_g$) to the first excited state ($B^1\Sigma^+{}_u$) and Werner transitions are to the second excited state ($C^1\Pi_g$) (Wakker 2006). We evaluated lines from the different rotational states for the molecule (J=0, 1, 2), where J=0 is the para-H_2 state or S=0, and J=1 is the ortho-H_2 state or S=1. We examined J=2 as well, but values greater than that yielded too few lines to allow curve of growth fitting. Because the gas is cold, the vibrational state is (v)=0.

First we used a HUT spectrum of NGC 3516 with markedly less noise to fit the continuum with the IDL routine SPLINE. Next we fit both the broad emission line and narrow emission lines for the O VI doublet. It was necessary to fit all of these features in order to obtain a template for the *FUSE* continuum plus BLR emission and thereby generate a H_2 synthetic spectrum.

The curve of growth method (COG) is used to describe absorption features that

are unresolved and saturated (Savage & Sembach 1991). Using the EW of the line, the oscillator strength and wavelength of the line we can estimate the column density of the gas creating the line by plotting EW divided by λ_{jk} against the factor $\lambda_{jk}\mathrm{f}_{jk}\mathrm{N}_j$, where λ_{jk} is the laboratory wavelength of the transition, f_{jk} is the oscillator strength of the transition and N_j is the column density of the species in question. By assuming different velocity impact parameters (b) of the gas we can create templates across a range of columns. We then plot the measured EW against column estimates to find where the points fit the templates best.

We measured the EW for as many H_2 lines as were available and unblended with other ISM or intrinsic lines to the object and created a curve of growth. To normalize the spectrum, we used the template created from the HUT fit, and simply scaled the HUT template to fit the current continuum flux level.

We performed this procedure for levels J=0, 1 & 2. Also, we were able to characterize the velocity for the H_2 cloud with velocity centroids measured at the same time we measured equivalent widths. For NGC 3516 we find values for the columns log[N(J=0)] = $18.4^{+0.3}_{-0.5}$, log [N(J=1)] = $18.5^{+0.7}_{-0.5}$ and log [N(J=2)] = 17.1$\pm$0.6 and a radial velocity for the system of -25.8 km $^{-1}$.

Charles Danforth provided us with an excellent program that was created by Jason Tumlinson (Tumlinson et al. 2002) and was subsequently used by Gillmon et al. (2006) to plot the synthetic H_2 spectrum using a fitted continuum and broad line region to the spectrum. In Fig 3.2 we show the best fit case for our synthetic

spectrum using the three previously discussed lower rovibrational levels. There do appear to be some lines which do not fit the actual spectrum. This could be due to noise or overestimates of particular levels. We chose this region due to the high number of H_2 lines present for a good evaluation of the fit.

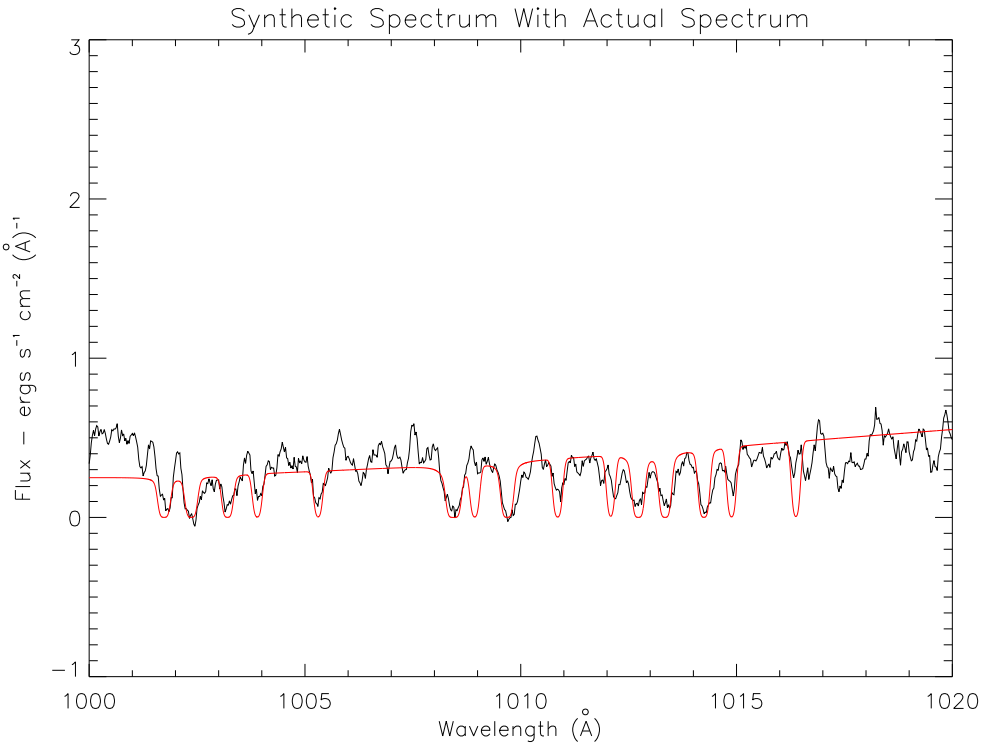

Figure. 3.2: Plot of the actual coadded spectrum (in black) with the overplotted synthetic spectrum (in red).

3.4 Intrinsic Absorption

Crenshaw et al. (1999) found that NGC 3516 showed 4 components of intrinsic absorption in the C IV doublet ranging in radial velocity between -375 km s^{-1} and -31 km s^{-1}, along with a range of FWHM between 206 km s^{-1} and 20 km s^{-1}.

Crenshaw et al. used primarily FOS data with 2 spectra from the GHRS.

Kraemer et al. (2002) showed that a total of 7 components could be resolved in STIS echelle spectra of NGC 3516 (Table 3.1), including the original components (1, 2, and the original 3 and 4 blended) and four new components (5-8) that appeared at a low flux state. The ionic column densities of these components were measured and fit with a CLOUDY model to estimate properties of the absorbing regions. They attributed variations in the absorption to changes in the ionizing flux rather than changes in the column density due to bulk motion. They also found a link between X-Ray absorption and UV absorption for NGC 3516.

Table. 3.1: Components for NGC 3516

Component	Velocity km s^{-1}	FWHM km s^{-1}	C_{los}
1	-376 (7)	70 (8)	0.98 (0.02)
2	-183 (8)	44 (10)	0.98 (0.02)
3+4	-36 (4)	20 (4), 31 (5)	0.95 (0.02)
5	-1372 (9)	271 (44)	0.81 (0.21)
6	-994 (16)	36 (6)	...
7	-837 (7)	99 (16)	...
8	-692 (4)	35 (5)	...

We find in our new spectra, that we can recover those same components. In Figure 3.3 we show the region containing the O VI doublet and Lyβ for both the 2006 and 2007 observations; note that the 2006 observation is only the spectrum taken by the LiF 1a segment. Both of the members of the doublet are visible in emission from the NLR at $\sim$1041 and 1047 Å. A dayglow Lyβ emission feature can be seen at

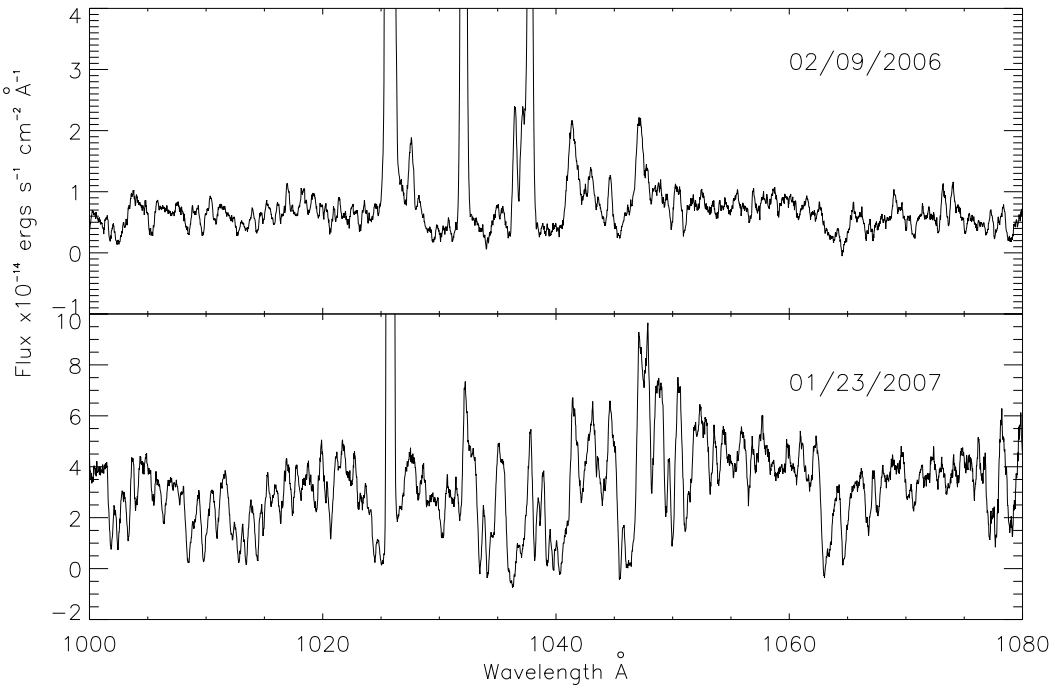

Figure. 3.3: Top: Spectrum for NGC 3516 in the observed frame taken 2006/02/09. The O VI doublet from the NLR is clearly visible at ∼1031 and 1037 Å and a Lyβ geocoronal dayglow line is at ∼1026 Å. The geocoronal emission at 1041 and 1047 Å is from O I. Bottom: Spectrum for NGC 3516 taken 2007/01/23. The flux for this observation is higher, but the O VI doublet is not easily visible. The same Lyβ geocoronal line is visible but there is no O I dayglow.

1025.72 Å. With O VI being so strong due to high abundance and oscillator strength, the absorption components are highly blended. The coadded spectrum for our 2006 February observation showed heavy contamination from geocoronal Lyβ in the Lyβ absorption features and O I contamination in the O VI λ1032 (O VIb) line. If we examine only the LiF portion of the spectrum however, we see no dayglow lines (see section 2.1), but the signal-to-noise falls significantly.

By examining the spectrum in velocity space we can identify the features seen

earlier by Crenshaw et al. (1999) and Kraemer et al. (2002). We plot in Figure 3.4 the coadded spectrum with each of the O VI doublet members and Lyβ in velocity space and overlay dotted lines marking the previously seen features. We can see that in the O VI λ1038 (O VIr) line the spectrum shows absorption signatures for 6 of the 7 components, but the fastest velocity component (5) is not visible due to the O VIb contamination.

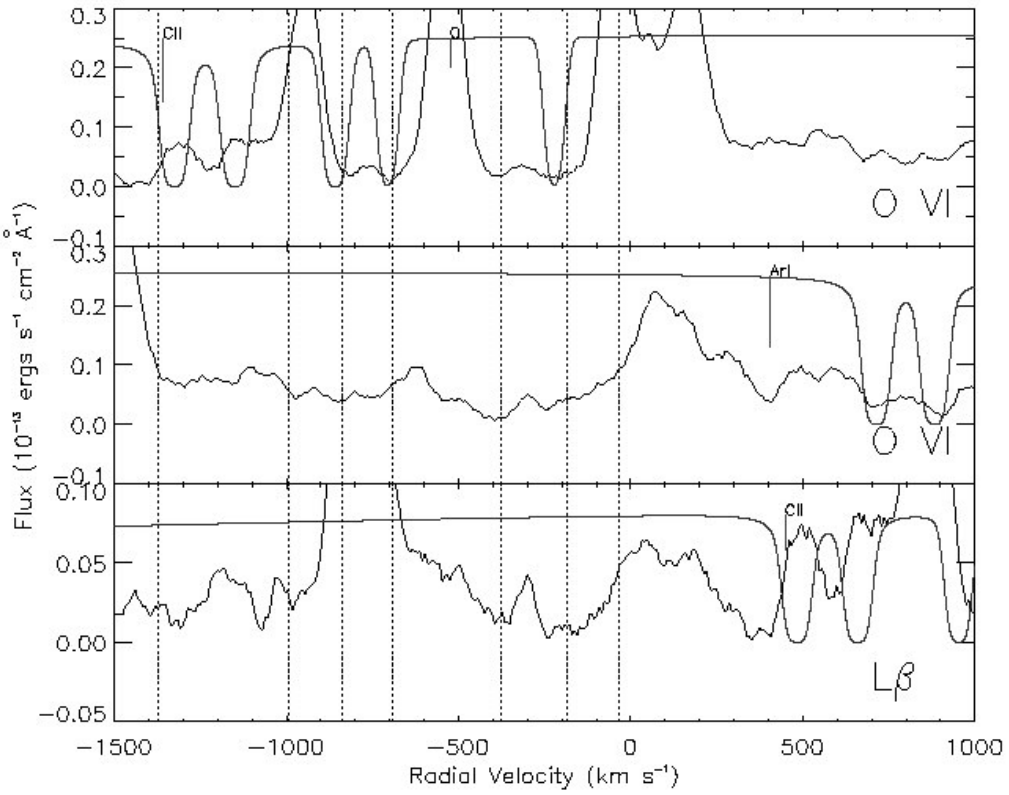

Figure. 3.4: Velocity plots for coadded spectrum of the OVI doublet (top: blue member, bottom: red member) and Lyβ. The dashed lines show the previous locations of absorbers found in Kraemer et al. (2002). The solid line is the H_2 synthetic spectrum. The ISM lines are scaled based on the oscillator strength.

Using the values predicted from the photoionization models of the *HST* data

by Kraemer et al. (2002) for O VI, along with the fits for continuum, broad line and narrow line we found for the H_2 fitting, we can check the validity of the O VI predictions in the *FUSE* data. Shown in Figure 3.5, we plot the coadded spectrum for NGC 3516 for the O VIr line. To model the spectrum in this region we fit the red wing of the O VI narrow emission line and inverted it about the peak to get the blue wing. We simulated the O VI absorption by combining the predicted O VI columns with the observed radial velocities, FWHMs and covering factors for the three kinematic components in this region, and assumed Gaussian profiles for the optical depths. We then generated a normalized absorption profile and multiplied by the continuum plus broad-line fit. Then we added our narrow emission profile to arrive at the fit shown in Figure 3.5. The excellent fit shows that the major kinematic components detected in the *HST* spectra are also present in the *FUSE* spectra and the prediction of saturated O VI columns by Kraemer et al. are correct. Furthermore, the shape of the absorption profile just blueward of the line peak is due to the unabsorbed blue wing of the narrow emission-line profile.

By recovering the same features as Crenshaw et al. (1999) and Kraemer et al. (2002), and showing we can match the predicted values of Kraemer et al., we find that while H_2 lines are prevalent in the far ultraviolet regime of the spectrum, it is possible to find absorption features and quickly estimate the amount of contamination if necessary, as seen in Figure 3.4. We also learn that O VI is very likely to be strong in outflows and therefore sensitive, because of abundance, to relatively small columns

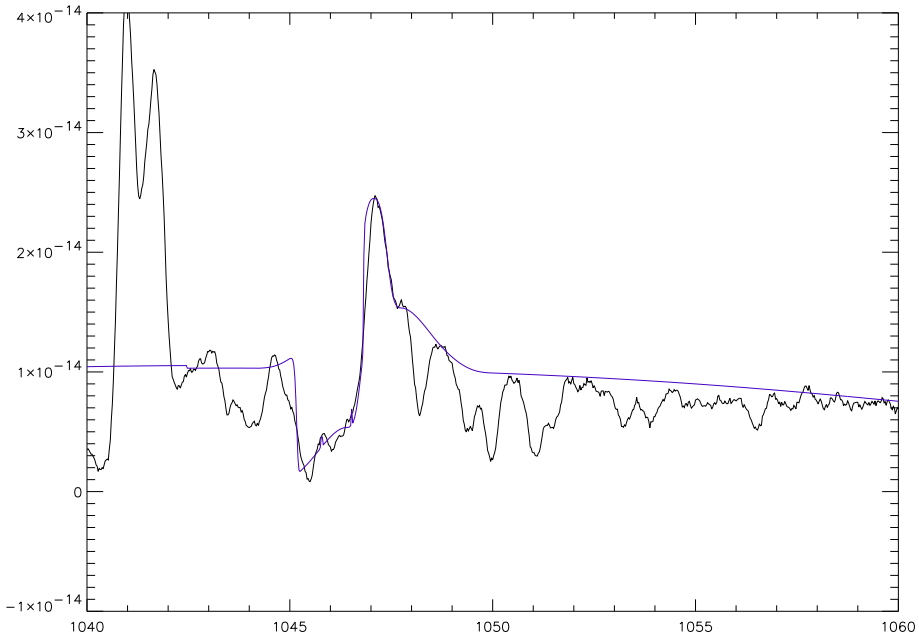

Figure. 3.5: Plot of the coadded spectrum for NGC 3516 in the region of OVIr. The solid blue line is our fit to the continuum, BLR and blue wing of the NLR. We include the estimate of absorption from Kraemer et al. (2002). The blue wing of the narrow-line profile fits the residual flux in the absorption trough from the NLR.

of gas, but saturation blends components together and makes O VI column density measurements difficult.

You keep using that word, I do no think it means what you think it means.

—— Mandy Patinkin (The Princess Bride)

– 4 –

The Search for Intrinsic Absorption

4.1 The Survey

Our survey is more than four times larger than that of Crenshaw et al. (1999) and is taken from the available *FUSE* data at the *Multimission Archives at Space Telescope (MAST)*[1]. *FUSE* is ideal for intrinsic absorption studies in AGN due to the wavelength coverage (905 Å to 1187 Å) that allows for the O VI doublet ($\lambda\lambda$1031.9, 1037.6) and Lyman β (λ1025.7) to be detected at low redshifts. *FUSE* also lends itself to this work because of its resolution, approximately 15 km s^{-1} (FWHM), allowing us to find narrow absorption features and resolve structure in broader features.

Because the LiF coating provides a reflectivity nearly twice that of the SiC at wavelengths greater than 1050 Å, this implies a better signal-to-noise across the LiF spectrum in the region of interest. We downloaded the raw data for all of the targets we selected and processed them using CalFUSE v3.2 in time-tag mode (TTAG) (Dixon et al. 2002). We coadded 7 of the 8 spectra into one spectrum weighted by exposure time. We did not include the LiF 1b segment in the coadded spectrum. We intentionally omitted this because of the 'worm' (section 2.1) in the spectrum

[1]url: http://archive.stsci.edu/

for this segment that has no available correction. For objects with multiple epochs of observing, we averaged the spectra. In section 5, we will examine the absorption variability using the multi-epoch observations.

FUSE has no calibration lamp onboard, leaving wavelength calibration to ISM lines (Sahnow et al. 2000). This introduces a velocity error of approximately 20 km s^{-1} (Gillmon et al. 2006), which is significant given a resolution of 15 km s^{-1}. However, our survey's initial purpose is to find Seyfert galaxies that exhibit intrinsic absorption and provide approximate velocity centroids, and as seen in NGC 3516 previously, a typical FWHM is on the order of 100 km s^{-1}.

Our list of targets originated from the category designations on the *MAST* website. We took all targets listed by observers as Seyfert galaxies or as Quasars, which comprised 253 targets. Using the NASA Extragalactic Database (NED)[2], we narrowed the total list to 143 objects by eliminating any targets that had a redshift greater than $z \approx 0.15$. Any target with a redshift greater than this places the O VI doublet outside of the wavelength coverage for *FUSE*. We have retained these data for possible further analysis of the C III line (λ977.03) and the N III (λ989.79) line.

We narrowed the list further to 122 objects, by removing any galaxy that had a type listed in NED other than Seyfert 1 or quasar; note that we still examined the spectra of these targets, but these were not included in the survey. We included only Seyfert 1 galaxies or quasars because detection of intrinsic absorption requires a

[2]url: http://nedwww.ipac.caltech.edu/index.html

strong background source (i.e. continuum and broad line region). It should be noted that in the Seyfert 2 spectra we did not find intrinsic absorption.

One interesting target that we originally removed is WPVS007 (Dunn et al. 2007). According to Leighly (2007), this Seyfert galaxy has evolved to a Broad Absorption Line mini-quasar. However, upon further examination we have found narrow absorption lines buried in the BAL trough. Thus, we have returned it to our list of absorbers.

The last criterion that we applied to the data was a signal-to-noise cutoff. By utilizing the provided noise vector with the data, we found a good cutoff for the signal-to-noise per resolution element ($\sim$ 15 km s^{-1} FWHM) of 1.5 across the span 1050Å to 1100Å. Although this value appears to be low, there are many resolution elements across a typical intrinsic absorption line. In this region we have data from the LiF portion of the spectrograph as well as data from the SiC portion coadded to give a good overall estimate of the quality of the spectrum.

Table 4.1 lists the 72 AGN that survived all these cuts and are thus used in our survey. We list the signal-to-noise we found in this region for a coadded spectrum per object. We also provide a list of the observations available per object. In the case of NGC 3516 we did not use all available observations. We chose to use only the 2000 observation, the LiF portion of the February 2006 observation and the January 2007 observation in our coadded spectrum. This set of spectra has a lower signal to noise, 1.9, than the total coadded spectrum, but these observations have no O I geocoronal

dayglow interference, which is heavy in the O VI region of the spectrum.

Table. 4.1: AGN Included in the Survey

Object	RA	Dec	z	Class[b]	S/N	Observation ID	Observation Date	Exposure Time (s)
MRK335	00 06 19.53	+20 12 10.3	0.026	Sey 1.2	54.9	P1010204000	11/21/2000	53391
						P1010203000	12/4/1999	45894
WPVS007	00 39 15.81	−51 17 01.9	0.029	Sey 1	5.1	D8060201000	11/6/2003	48135
QSO0045+3926	00 48 18.90	+39 41 12.0	0.134	Sey 1	9.6	D1310101000	10/8/2003	42658
						D1310105000	11/25/2004	25452
						D1310106000	11/26/2004	27487
						D1310104000	12/9/2003	40728
						D1310107000	11/27/2004	25058
						D1310102000	10/10/2003	34371
						Z0020401000	11/25/2000	8561
						D1310103000	10/11/2003	7272
I ZW 1	00 53 34.90	+12 41 36.0	0.061	Sey 1	3.8	P1110101000	12/3/1999	13584
						P1110102000	11/20/2000	25189
TONS180	00 57 19.95	−22 22 59.3	0.062	Sey 1.2	14.0	P1010502000	12/12/1999	15420
						D0280101000	7/13/2004	8955
MRK352	00 59 53.28	+31 49 36.7	0.015	Sey 1	3.7	P1070201000	10/11/1999	16644
RXJ010027-511346	01 00 27.06	−51 13 54.8	0.063	Sey 1	2.5	D8060301000	9/11/2003	6321
						E8970201000	8/22/2004	16845
TONS210	01 21 51.56	−28 20 57.3	0.116	Sey 1	23.0	P1070301000	10/21/1999	14023
						P1070302000	8/10/2001	41023
FAIRALL9	01 23 46.04	−58 48 23.8	0.047	Sey 1	12.54	P1010601000	7/3/2000	34896
MRK1044	02 30 05.45	−08 59 52.6	0.016	Sey 1	7.3	D0410101000	1/1/2004	12608
NGC985	02 34 37.77	−08 47 15.6	0.043	Sey 1	29.4	P1010903000	12/24/1999	49968
ESO31-8	03 07 35.30	−72 50 06.2	0.028	Sey 1	3.3	D9110201000	7/13/2003	15915
EUVEJ0349-537	03 49 28.50	−53 44 47.0	0.130	Sey 1	2.9	E8970301000	8/20/2004	27732
IRASF04250-5718	04 26 00.83	−57 12 00.4	0.104	Sey 1	2.1	D8080801000	9/4/2003	4895
FAIR303	04 30 40.02	−53 36 55.9	0.040	Sey 1	3.1	D8060702000	10/31/2003	16728
MRK618	04 36 22.25	−10 22 33.9	0.036	Sey 1	3.2	P1070901000	10/21/1999	2691
						P1070902000	12/7/2000	6293
AKN120	05 16 11.42	−00 08 59.4	0.033	Sey 1	12.2	P1011203000	12/31/2000	25617

Continued on Next Page...

Table. 4.1 – Continued

Object	RA	Dec	z	Class[b]	S/N	Observation ID	Observation Date	Exposure Time (s)
						P1011201000	11/1/2000	8448
						P1011202000	11/3/2000	20942
PKS0558-504	05 59 47.40	−50 26 52.0	0.137	NL Sey 1	18.4	C1490601000	11/7/2002	48480
						P1011504000	12/10/1999	47271
IRASL06229-6434	06 23 09.10	−64 36 24.0	0.129	Sey 1	2.9	D9030304000	12/17/2003	14494
						U1071002000	7/19/2006	18569
						D9030301000	12/14/2003	51104
						U1071001000	7/17/2006	11284
						D9030302000	12/16/2003	23363
						D9030303000	12/17/2003	11122
VIIZW118	07 07 13.10	+64 35 58.8	0.080	Sey 1	11.6	P1011606000	1/1/2000	9805
						P1011604000	10/6/1999	77568
						P1011605000	11/29/1999	26075
						P1011601000	10/2/1999	47515
						S6011301000	2/8/2002	47363
						P1011603000	10/2/1999	8957
1H0707-495	07 08 41.50	−49 33 05.8	0.041	Sey 1	12.8	B1050101000	11/16/2001	19989
						E1190101000	12/10/2004	50252
						B1050102000	3/6/2003	24260
						B1050103000	3/6/2003	22576
MRK9	07 36 57.02	+58 46 13.4	0.040	Sey 1.5	5.3	P1071102000	1/8/2000	14278
						P1071101000	11/29/1999	11829
						P1071103000	2/22/2000	10664
						S6011601000	2/11/2002	23555
MRK79	07 42 32.80	+49 48 34.9	0.022	Sey 1.2	3.0	P1011702000	1/14/2000	11688
						P1011701000	11/30/1999	3147
						P1011703000	2/22/2000	12498
MRK10	07 47 29.10	+60 56 01.0	0.029	Sey 1.2	2.7	Z9072801000	2/2/2003	22699
IR07546+3928	07 58 0.05	+39 20 29.1	0.096	Sey 1.5	6.7	P1071201000	3/9/2000	15290
						S6011801000	2/11/2002	27410
						E0870101000	11/7/2004	53151
PG0804+761	08 10 58.46	+76 02 41.9	0.100	Sey 1	28.3	S6011002000	2/9/2002	36886

Continued on Next Page...

Table. 4.1 – Continued

Object	RA	Dec	z	Class[b]	S/N	Observation ID	Observation Date	Exposure Time (s)
						S6011001000	2/5/2002	58506
						P1011901000	10/5/1999	42715
						P1011903000	1/4/2000	21128
UGC4305	08 19 12.90	+70 43 06.0	0.001	Sey 1	11.1	F0270104000	12/20/2005	2210
						F0270102000	12/18/2005	28130
						F0270103000	12/19/2005	18821
PG0838+770	08 44 45.26	+76 53 10.0	0.132	Sey 1	2.62	G0200101000	2/10/2006	5942
						G0200104000	2/13/2006	35047
Ton951	08 47 42.60	+34 45 04.7	0.064	Sey 1	7.515	D0280304000	3/15/2004	10874
						P1012002000	2/20/2000	30962
						D0280303000	3/15/2004	12774
						D0280302000	3/15/2004	12713
						D0280301000	3/14/2004	7935
IRAS09149-62	09 16 9.41	−62 19 29.5	0.057	Sey 1	6.45	S7011003000	3/31/2005	14520
						S7011002000	3/30/2005	13648
						A0020503000	2/6/2000	13157
						U1072201000	1/19/2006	7554
MRK110	09 25 12.87	+52 17 10.7	0.035	Sey 1	2.52	P1071302000	2/11/2001	10791
TON1187	10 13 3.21	+35 51 22.2	0.079	Sey 1	2.90	P1071502000	1/13/2000	7994
PG1011-040	10 14 20.58	−04 18 41.2	0.058	Sey 1	35.78	B0790101000	5/16/2001	85197
MKN141	10 19 12.59	+63 58 02.7	0.042	Sey 1.5	1.73	D8061001000	3/21/2004	15768
MKN142	10 25 31.28	+51 40 34.9	0.045	Sey 1	8.53	D8061101000	3/23/2003	20103
KUV-1031+398	10 34 38.61	+39 38 28.4	0.042	Sey 1	7.08	A0990101000	4/30/2000	53185
NGC3516	11 06 47.55	+72 34 06.9	0.009	Sey 1.5	1.91[a]	P2110103000	1/28/2003	16753
						G9170101000	2/9/2006	28718
						P1110404000	4/17/2000	16335
						P2110102000	2/14/2002	20702
						P2110104000	3/29/2003	16125
						G9170102000	1/23/2007	16877
ESO265-G23	11 20 47.89	−43 15 50.6	0.056	Sey 1	3.2	A1210409000	4/29/2002	6428
						A1210405000	3/9/2001	4863
						A1210408000	4/28/2002	11487

Continued on Next Page...

Table. 4.1 – Continued

Object	RA	Dec	z	Class[b]	S/N	Observation ID	Observation Date	Exposure Time (s)
						A1210407000	3/7/2002	21716
						A1210406000	2/28/2002	8381
						A1210404000	5/28/2000	1782
MRK734	11 21 47.11	+11 44 18.3	0.050	Sey 1.2	3.1	P1071702000	4/16/2001	4587
NGC3783	11 39 01.78	−37 44 18.5	0.010	Sey 1	21.6	B1070103000	3/11/2001	27221
						B1070104000	3/30/2001	25180
						B1070105000	6/27/2001	27483
						B1070106000	3/7/2001	25541
						P1013301000	2/2/2000	37003
						E0310101000	5/5/2004	23286
						B1070102000	2/28/2001	26645
IR1143-1810	11 45 40.48	−18 27 15.3	0.033	Sey 1	8.51	P1071901000	5/29/2000	7243
NGC4051	12 03 09.61	+44 31 52.8	0.002	Sey 1.5	7.26	B0620201000	3/29/2002	28659
						C0190102000	3/19/2003	28594
						C0190101000	1/18/2003	13933
NGC4151	12 10 32.60	+39 24 21.0	0.003	Sey 1.5	61.79	P2110201000	4/8/2001	13612
						P2110202000	6/1/2002	5953
						C0920101000	5/28/2002	48892
						P1110505000	3/5/2000	21522
PG1211+143	12 14 17.61	+14 03 12.7	0.081	Sey 1	40.02	P1072001000	4/25/2000	52274
MRK205	12 21 44.04	+75 18 38.3	0.071	Sey 1	24.71	S6010801000	2/2/2002	16027
						D0540101000	11/13/2003	19618
						D0540103000	11/17/2003	19131
						Q1060203000	12/29/1999	37051
						D0540102000	11/14/2003	114015
NGC4395	12 25 48.92	+33 32 48.4	0.001	Sey 1	4.39	C0860101000	2/25/2003	36484
RXJ1230.8+0115	12 30 50.00	+01 15 22.7	0.117	Unk[c]	2.79	P1019001000	6/20/2000	4031
PG1229+204	12 32 3.62	+20 09 29.4	0.063	Sey 1	2.62	P1072301000	2/5/2001	6267
TOL1238-364	12 40 52.90	-36 45 21.1	0.011	Sey 2?	4.67	D0100101000	6/13/2003	17912
PG1351+640	13 53 15.80	+63 45 45.0	0.088	Sey 1	15.42	S6010701000	2/1/2002	48620
						P1072501000	1/18/2000	70134
MRK279	13 53 3.52	+69 18 29.7	0.030	Sey 1.5	53.24	P1080304000	1/11/2000	30747

Continued on Next Page...

Table. 4.1 – Continued

Object	RA	Dec	z	Class[b]	S/N	Observation ID	Observation Date	Exposure Time (s)
						F3250103000	12/7/2005	2289
						C0900201000	5/18/2002	41708
						D1540101000	5/12/2003	91040
						F3250104000	12/8/2005	3187
						F3250106000	2/3/2006	3703
						P1080303000	12/28/1999	60338
RXJ135515+561244	13 55 16.55	+56 12 44.6	0.122	Sey 1	1.78	D8061601000	3/13/2003	47223
PG1404+226	14 06 22.15	+22 23 42.8	0.098	Sey 1	1.86	P2100401000	6/11/2001	11489
PG1411+442	14 13 48.32	+44 00 13.1	0.090	Sey 1	2.64	A0601010000	5/11/2000	7360
PG1415+451	14 17 00.84	+44 56 06.0	0.114	Sey 1	2.47	A0601111000	5/10/2000	12285
NGC5548	14 17 59.91	+25 08 12.6	0.017	Sey 1.5	11.11	D1550102000	2/11/2004	7757
						P1014601000	6/7/2000	25932
						D1550101000	2/10/2004	22229
MRK1383	14 29 6.60	+01 17 06.6	0.086	Sey 1	22.27	P1014801000	2/18/2000	25051
MRK817	14 36 22.09	+58 47 39.5	0.031	Sey 1.5	49.78	P1080404000	2/18/2001	86013
						P1080402000	2/18/2000	12911
						P1080401000	2/17/2000	12119
						P1080403000	12/23/2000	71804
MRK477	14 40 38.06	+53 30 15.7	0.038	Sey 1	7.25	P1110808000	5/8/2001	11289
MRK478	14 42 07.46	+35 26 22.9	0.079	Sey 1	1.86	P1110909000	1/29/2001	14118
MRK290	15 35 52.38	+57 54 09.3	0.030	Sey 1	5.53	D0760101000	6/28/2003	9239
						D0760102000	2/27/2004	46032
						P1072901000	3/16/2000	12769
						E0840101000	6/15/2004	11931
MRK876	16 13 57.21	+65 43 09.7	0.129	Sey 1	37.02	P1073101000	10/16/1999	52659
						D0280201000	5/16/2003	11786
						D0280203000	2/14/2004	73334
PG1626+554	16 27 56.09	+55 22 32.0	0.133	Sey 1	2.15	P1073201000	2/18/2000	9754
						C0370101000	5/20/2002	91237
MRK506	17 22 39.92	+30 52 53.1	0.043	Sey 1	4.34	P1073401000	6/8/2000	10430
3C382	18 35 03.38	+32 41 47.0	0.058	Sey 1	3.15	P1073701000	6/9/2000	11297
PKS2005-489	20 09 25.39	−48 49 53.7	0.071	QSO	6.97	C1490301000	4/12/2002	24726

Continued on Next Page...

Table. 4.1 – Continued

Object	RA	Dec	z	Class[b]	S/N	Observation ID	Observation Date	Exposure Time (s)
						C1490302000	6/4/2002	13422
MRK509	20 44 09.74	−10 43 24.7	0.034	Sey 1.2	42.83	P1080601000	9/5/2000	60656
						X0170102000	11/6/1999	33410
						X0170101000	11/2/1999	20004
IIZW136	21 32 27.83	+10 08 19.4	0.063	Sey 1	11.55	P1018301000	11/14/2000	22629
						P1018302000	5/27/2004	11497
						P1018303000	5/28/2004	8067
						P1018304000	11/1/2004	21872
MRK304	22 17 12.28	+14 14 20.9	0.066	RQQ	3.05	P1073901000	7/16/2000	12387
AKN564	22 42 39.34	+29 43 31.3	0.025	Sey 1.8	6.19	B0620101000	6/29/2001	55515
IRASF22456-5125	22 48 41.00	−51 09 54.0	0.100	Sey 1	6.82	Z9073902000	9/24/2002	31301
						Z9073901000	9/24/2002	5534
MR 2251-178	22 54 05.80	−17 34 55.0	0.064	Sey 1	16.13	P1111010000	6/20/2001	54113
NGC7469	23 03 15.62	+08 52 25.6	0.016	Sey 1.2	2.22	C0900101000	12/13/2002	3593
						C0900102000	12/14/2002	3352
						P1074101000	6/28/2000	13217

[a] Reduced from a possible S/N of 3.34.

[b] AGN types listed in the NASA Extragalactic Database

[c] No AGN type listed. From the *FUSE* spectrum, it appears to be a type 1 QSO.

4.2 Absorption Detection

4.2.1 Identification

In order to determine which lines are truly intrinsic versus lines that originate in our Galaxy's ISM, we used the Tumlinson et al. (2002) program (§3.2) that provides a synthetic H_2 spectrum, which we overlayed on our velocity plots. As an example, Figure 4.1 shows the spectrum of IRAS F04250-5718. We have the blue member and red member of the O VI doublet and the Lyman β lines in respective order from top to bottom, plotted in velocity space. The dashed line is the overlayed H_2 synthetic spectrum from the Tumlinson code, and the other lines are ISM lines, taken from Morton (1991), with tickmarks scaled to their oscillator strengths. The program requires H_2 columns to be input for each rovibrational level of the molecule.

Based on our test case, NGC 3516, we saw that detailed modeling of the H_2 is not necessary to uncover the intrinsic absorption. So, for detection purposes we input exceptionally high values for the column for each rovibrational level (lower angular momentum level J=0 through 7), on the order of 10^{19} cm^{-2}. This was to establish positions for all known H_2 lines and to identify any possible contaminant to the intrinsic absorption. For H_2 lines that were coincident with a possible intrinsic absorption feature, we examined nearby H_2 lines for both number and strength to place estimates on the contamination. Another factor that presented problems were geocoronal dayglow emission lines.

We visually examined the spectra for lines that did not match the H_2 synthetic spectra or the ISM lines. These were flagged for further consideration. We identified clean intrinsic absorption features that had components at approximately the same velocity in at least two of the available lines (the two members of the O VI doublet and Lyman β). Any absorption line that aligned in velocity space for two of the three available lines with at least a 2σ detection in equivalent width was identified as intrinsic absorption. We recorded the approximate velocities of these lines based on plots similar to Figure 4.1, which we provide in Table 4.2. An example is IRAS F04250-5718. We can see in Figure 4.1 for IRAS F04250-5718 that intrinsic absorption appears in all three lines at relatively the same velocity with one broad component ranging between -300 and -100 km s^{-1} and an additional component at approximately -100 km s^{-1}.

In all, we found intrinsic absorption in 35 AGN. We present the coadded spectra for the absorbers in Figures 4.2-4.11. A handful of targets are still enigmas; they show unexplained lines, but the lines either do not agree in velocity or are possibly contaminated by ISM. All AGN that only contained one line or highly questionable lines were discarded as non-absorbers. We provide a target by target explanation in Appendix A.

4.2.2 Comparison

There have been two previous surveys of intrinsic UV absorption in low-z AGN: Crenshaw et al. (1999) and the preliminary survey by Kriss (2002). Crenshaw et

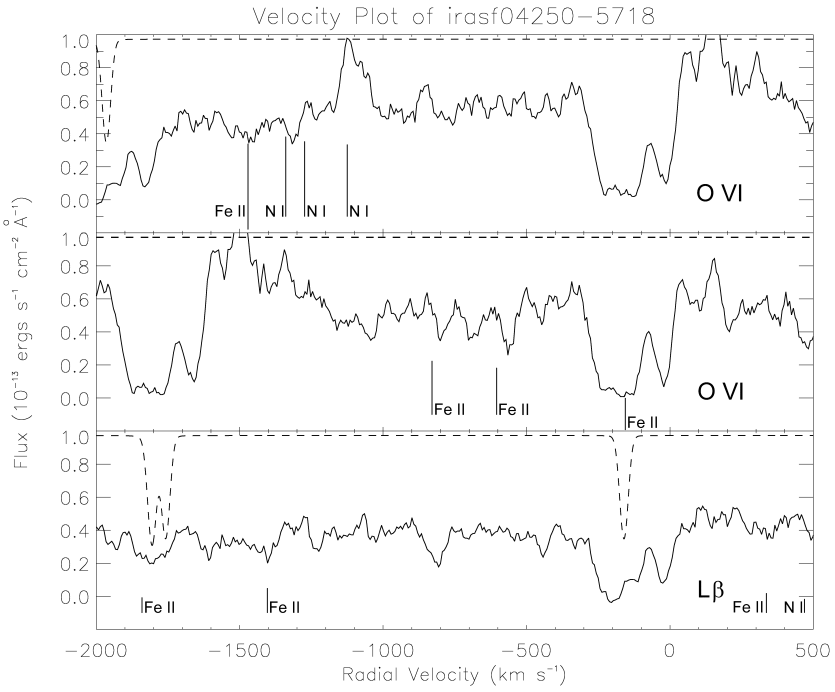

Figure. 4.1: Plot of the spectrum of IRAS 04250-5718 in velocity space. The intrinsic absorption is visible in components between -300 and -50 km s^{-1}. The ISM tick marks are sized relative to oscillator strength, and the H_2 spectrum is the dashed curve. Between -1000 and -500 km s^{-1} there are possibly two ISM lines of Fe II that can be seen offset by approximately -50 km s^{-1} with respect to the observed frame. This gives us a good approximation for all Fe II lines across the spectrum.

al. had 17 targets in their C IV survey of data from the Faint Object Spectrograph (FOS) and the Goddard High Resolution Spectrograph (GHRS). In the paper they labeled each of the targets as absorbers or non-absorbers, and we agree on all but one target of the 17, I Zw 1. Kriss had 16 targets which he identified with *FUSE* spectra as intrinsic absorbers. We disagree on three of the targets, I Zw 1, Mrk 304 and Mrk 478.

I Zw 1 is a weak C IV absorber in the spectrum taken by FOS. In the *FUSE*

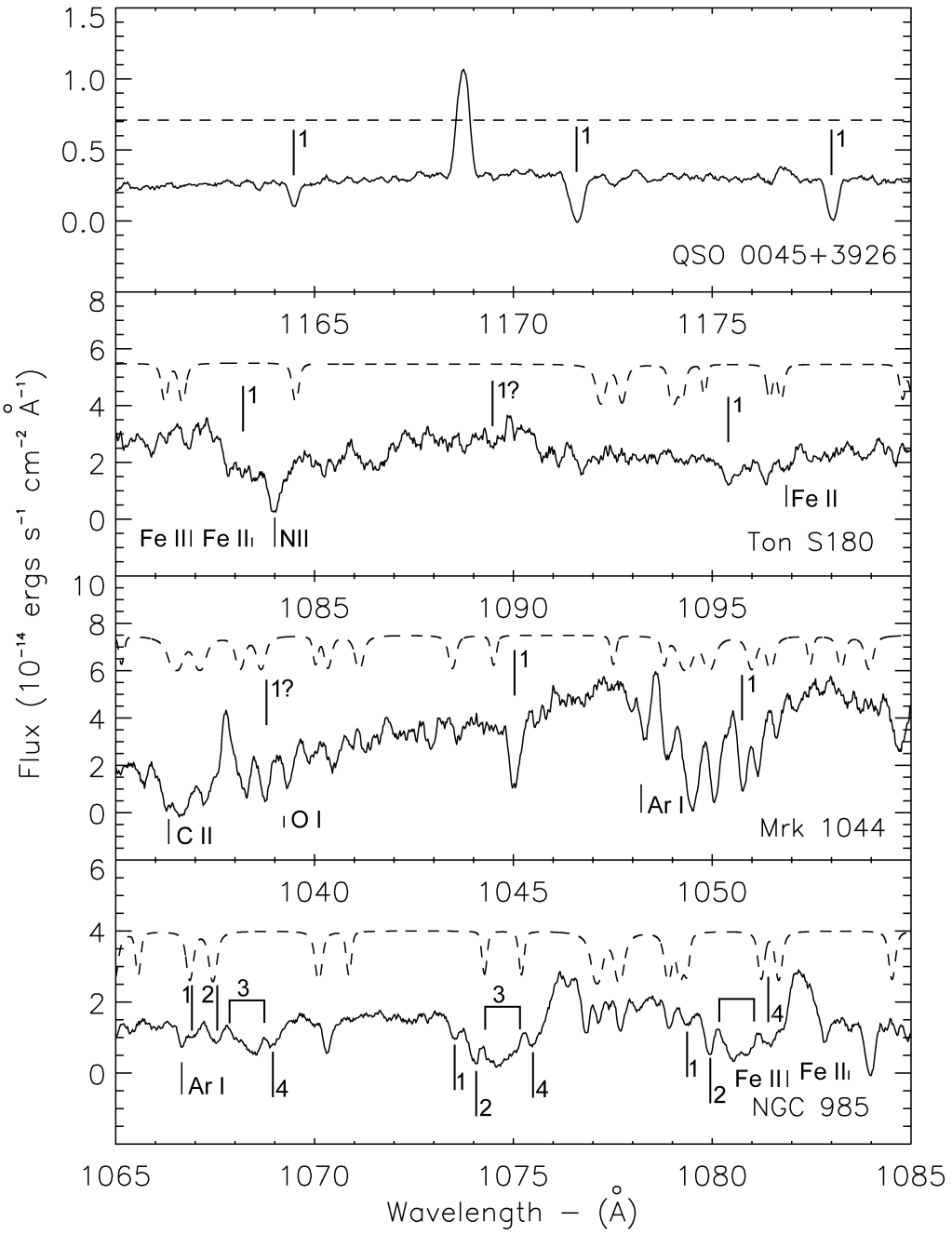

Figure. 4.2: We present all of the spectra for the targets we identified as having intrinsic absorbers. The spectra are plotted in the observed frame and kinematic components of intrinsic absorption in the lines of Lyβ (λ1025.7) and O VI ($\lambda\lambda$1031.9, 1037.6) are numbered. Broad components are indicated by brackets. Strong narrow emission lines are geocoronal. The dashed line represents the synthetic H_2 spectrum.

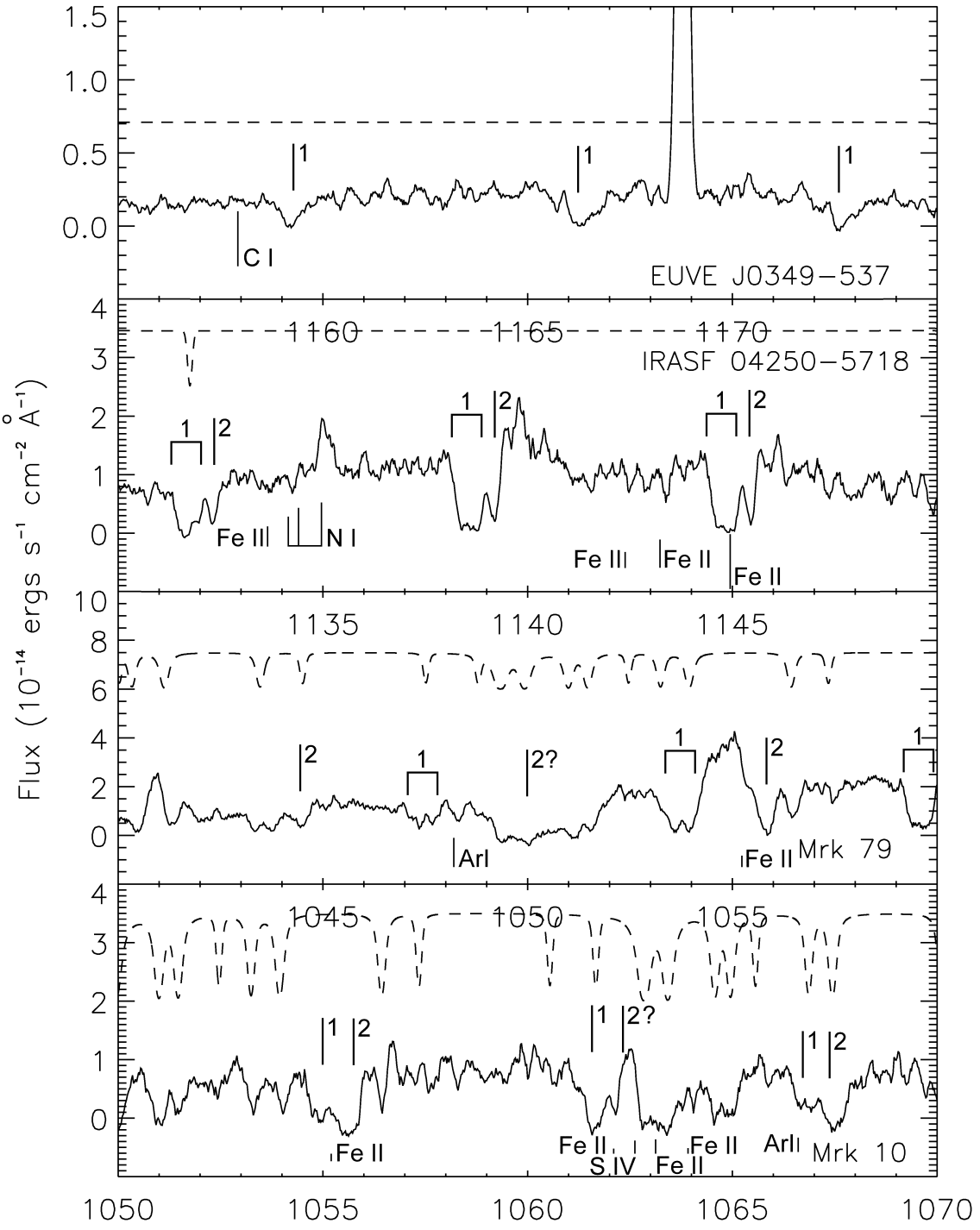

Figure. 4.3: Cont.

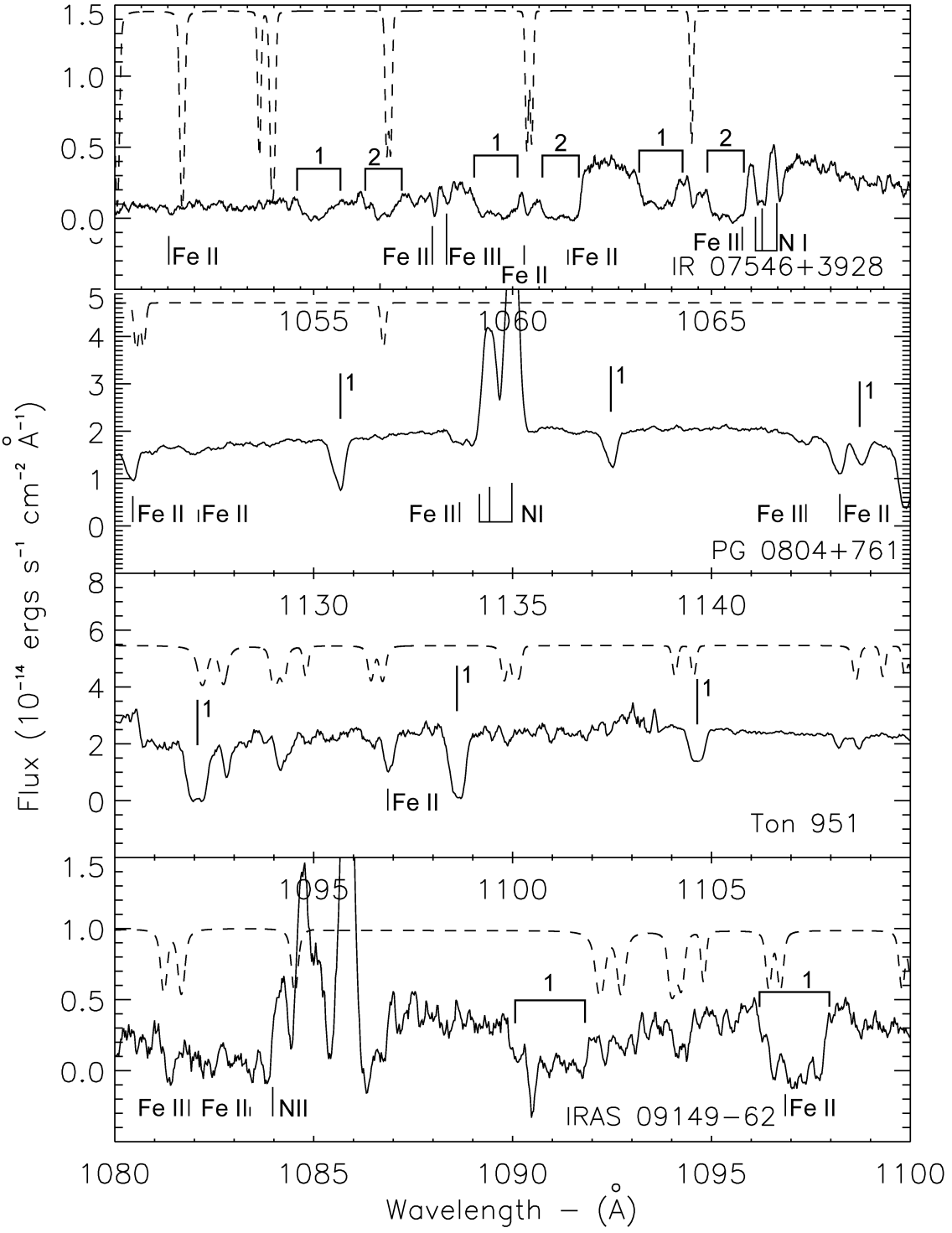

Figure. 4.4: Cont.

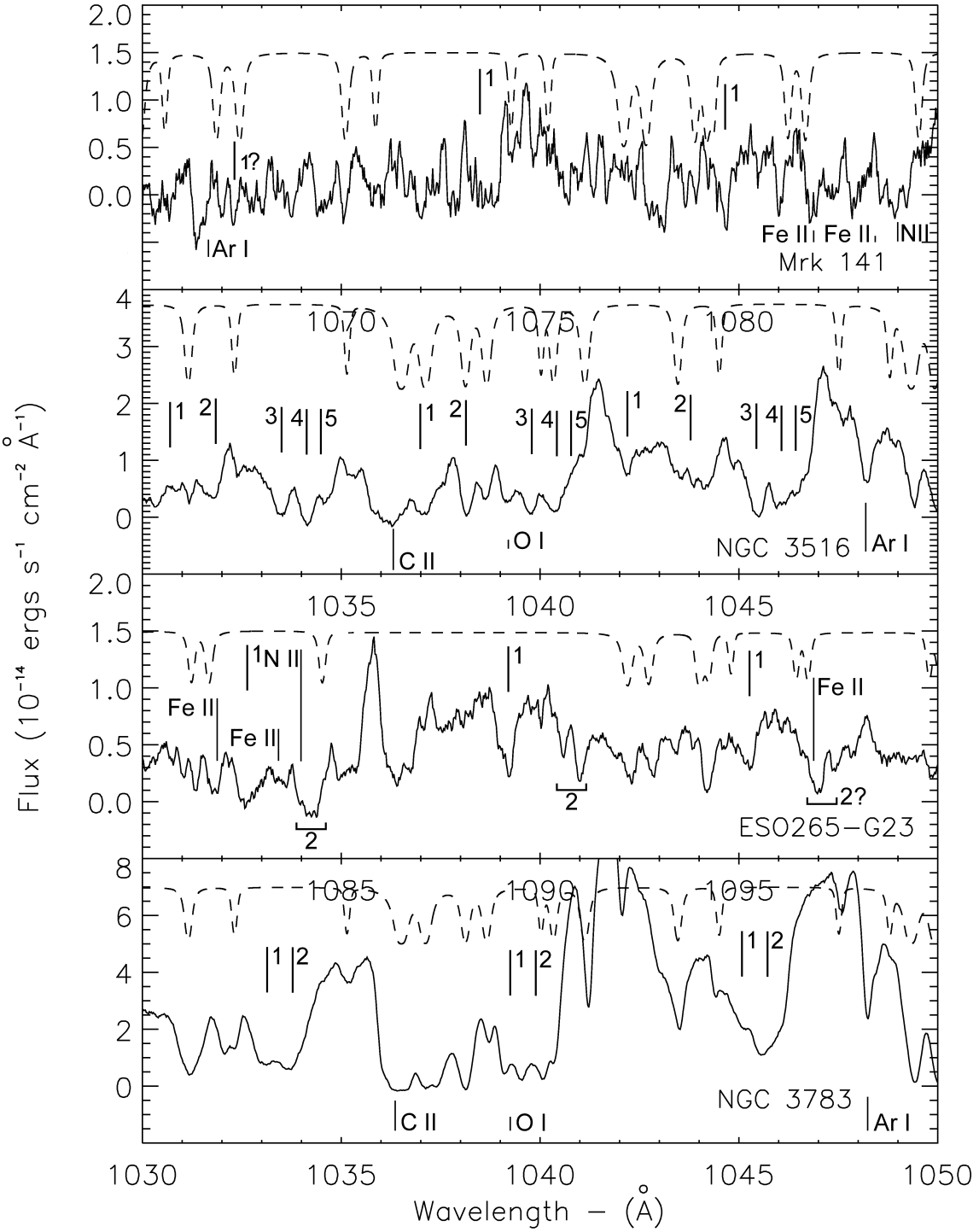

Figure. 4.5: Cont.

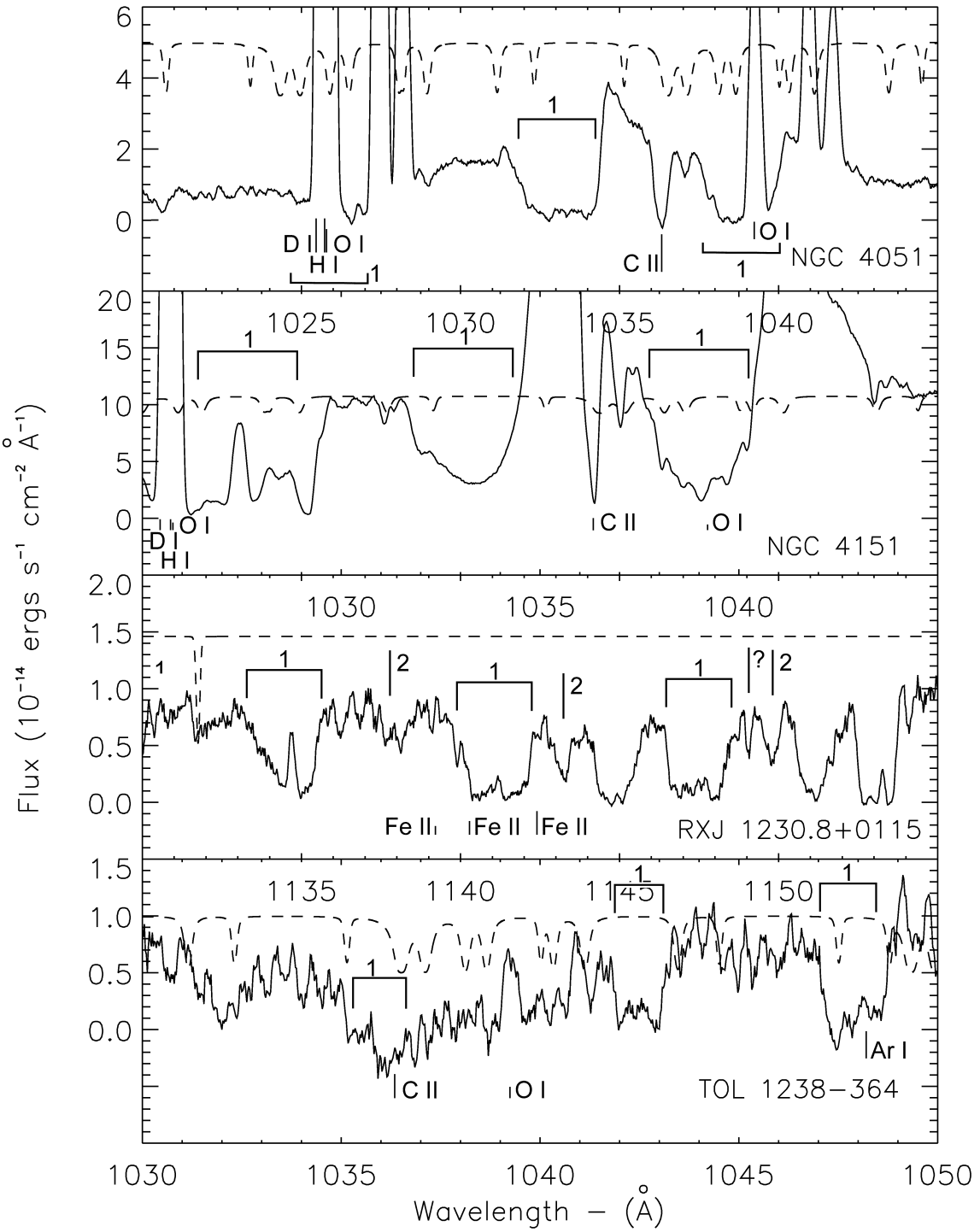

Figure. 4.6: Cont.

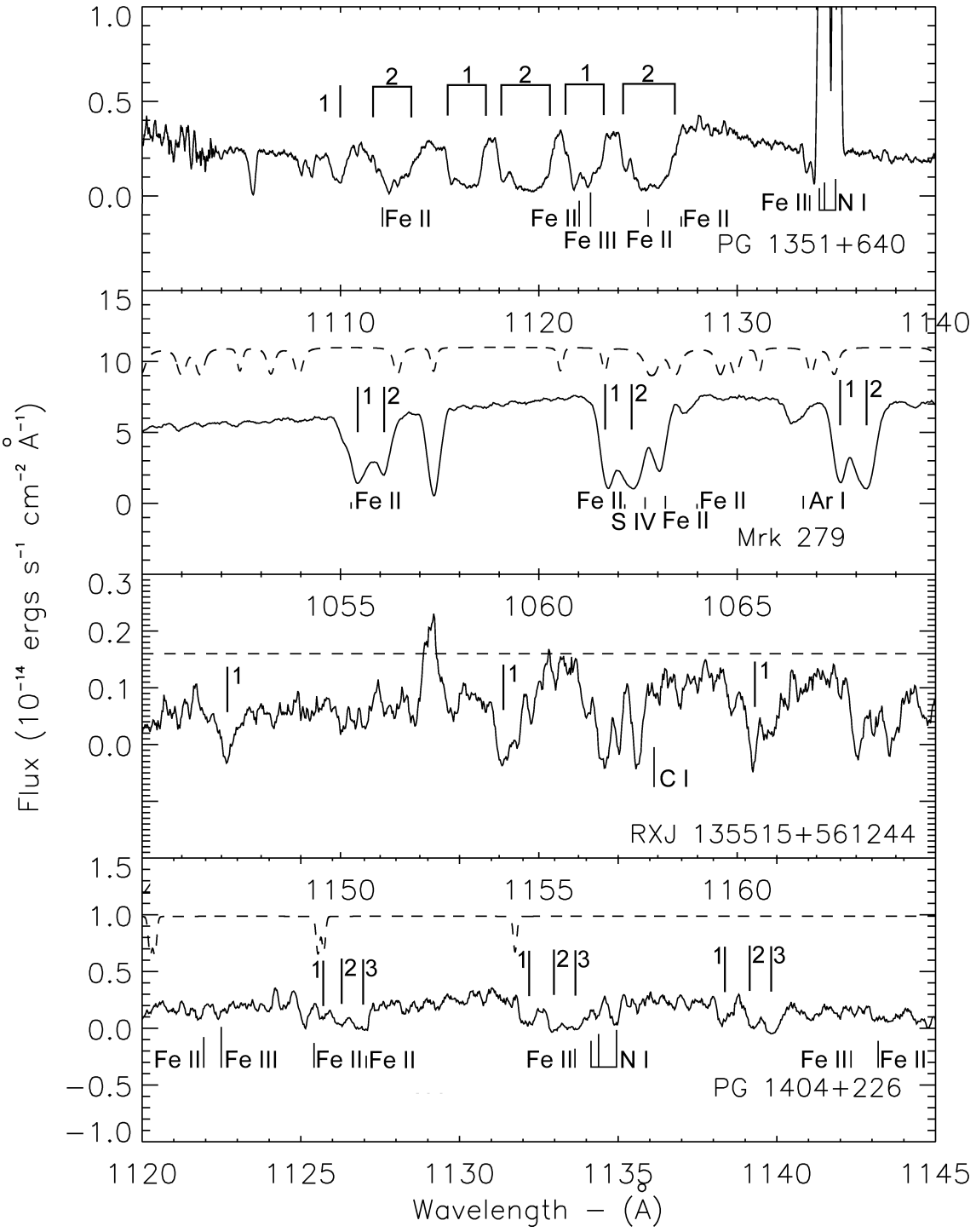

Figure. 4.7: Cont.

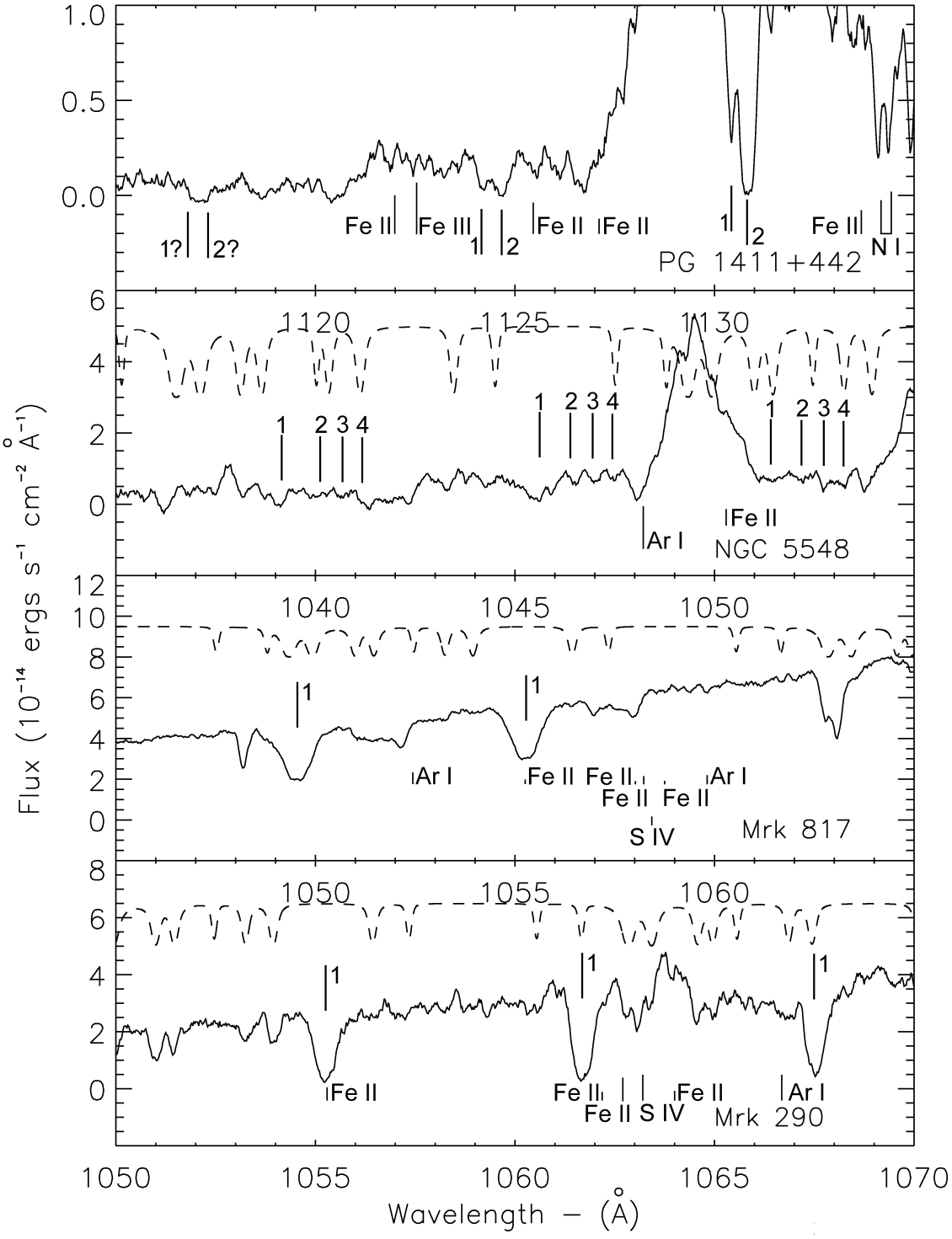
PG 1411+442
1?
2?
Fe II
Fe III
Fe II
Fe II
Fe II
N I
NGC 5548
Ar I
Fe II
Mrk 817
Ar I
Fe II
Fe II
Fe II
S IV
Mrk 290
Fe II
Fe II
Fe II
S IV
Fe II
Ar I
Flux (10^-14 ergs s^-1 cm^-2 Å^-1)
Wavelength – (Å)

Cont.

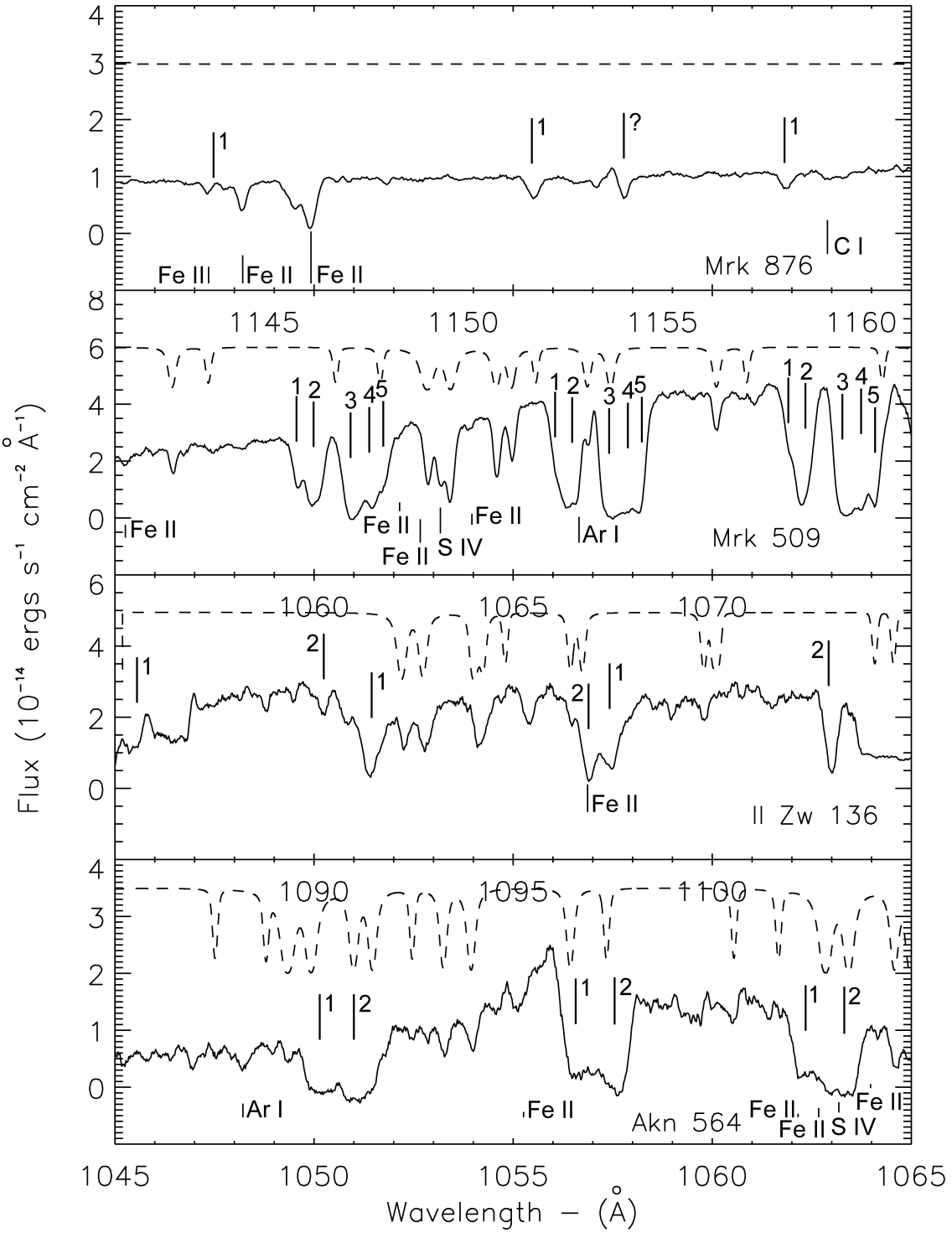

Figure. 4.8: Cont.

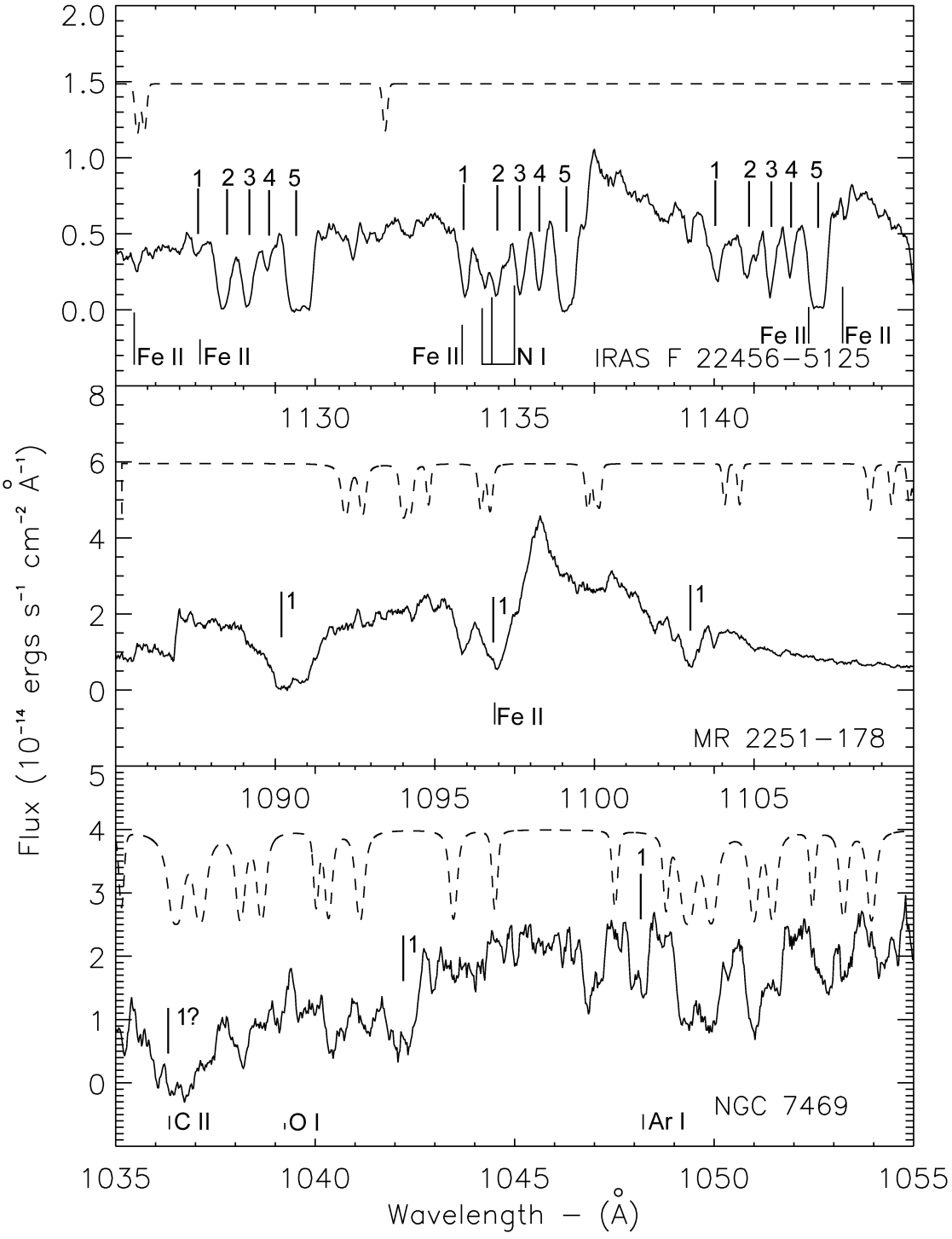

Figure. 4.9: Cont.

observation, I Zw 1 is in a low flux state. Thus, the O VI absorption lines may be present, but we label this target as a non-absorber because the potential lines are much like the surrounding noise. There is a line at approximately 1800 km^{-1}, but we only see it clearly in the O VI blue member. The other two are contaminated by H_2.

Mrk 304 and Mrk 478 have both been categorized as absorbers in the preliminary *FUSE* survey by Kriss (2002), but in our opinion Mrk 304 does not fit our conservative criteria. Mrk 478 shows no lines that cannot be explained by ISM contamination. Mrk 304 shows a possible line at 1800 km s^{-1} but it can only be seen in the Lyβ. Thus by our standards, this object is only a possible absorber, and we do not include it as a firm detection. While NGC 7469 is a well known intrinsic absorber, the signal-to-noise of NGC 7469 combined with heavy H_2 contamination lead to a problematic spectrum.

Another survey we tested against was Laor & Brandt (2002), which used mostly *HST* data. While they had a broad range of redshifts and object types, there were 12 objects that appeared in both of the studies. Of these 12 objects we agreed on 9. One object appears in both studies, but the signal-to-noise in the *FUSE* spectrum is too low for our study. Once again I Zw 1 and Mrk 304 are not absorbers on our list, but Laor & Brandt has classified them as absorbers. Mrk 290 however is listed by Laor et al. as a non-absorber, while we see a distinct absorbing feature at approximately 200 km s^{-1}.

4.3 Conclusions

For our final count we find of the 72 AGN with reasonably good signal-to-noise that 36 are intrinsically absorbing, with 11 new detections (see Appendix A). Crenshaw et al. (1999) found approximately 60% of their sample show intrinsic absorption. In our survey, we find that 50% are absorbers. This is a lower bound on the value due to the number of observations where the exposure times were not long enough to obtain a good signal-to-noise for the object. So the sample may be slightly biased toward detecting absorption in AGN that are brighter in the far-UV.

An important quantity to be determined is the global covering factor(C_g), which is the fraction of the sky covered by the ensemble of absorbers as seen from the nucleus. This quantity is useful in helping us understand the geometry of the nucleus and the absorbing region. Now, $C_g = F<C_f>$, where F is the fraction of galaxies that show intrinsic absorption and $<C_f>$ is the covering factor in the line of sight for the deepest component, averaged over all AGN with absorption. To estimate C_f for each individual AGN, we measured the residual flux (F_r) in the core of the deepest line. Assuming the component is saturated, and the residual flux is therefore unabsorbed continuum plus BLR flux (F_c), then $C_f = (1 - F_r/F_c)$. If the core is not saturated, which is unlikely in most cases, the value of C_f that we derived is actually a lower limit. Crenshaw et al. 1999 found $<C_f> \approx 0.85$. We measured the residual flux in saturated lines in the *FUSE* data and found that $<C_f> \approx 0.86$, so it is very similar in both near UV and far UV. Using $<C_f> \approx 0.86$ with $F \approx 0.50$ we find a global

covering factor of $C_g \approx 0.43$.

This measurement has also been made for other AGN samples. Ganguly et al. (2001) found a fraction of only 0.25 for C IV absorption in quasars with $z < 1.0$, while the Laor & Brandt study found F = 0.50 for Seyferts and quasars up to redshifts of 0.5. George et al. (2000) found F = 0.3 for X-ray absorption in low-z quasars, and Vestergaard (2003) found F = 0.55 for quasars between 1.5 and 3.5 in redshift for C IV absorption. So for several luminosities and a wide range of redshift, most surveys find values for F around 1/2. Given that C_f is usually close to 1, most studies find $C_g \approx 0.5$.

In the next chapter, we will provide measurements of equivalent width, full width at half maximum, velocity and other parameters by fitting these lines to find velocity centroids and equivalent width measurements. Once we have these values, we will examine each individual spectrum for variability in equivalent width, velocity and/or new components, which could lead to determinations of transverse velocities for the absorbers, as seen in Kraemer et al. (2001).

Don't be sorry, be quiet!

—— *Ronny Graham (Spaceballs)*

– 5 –

Characterizing the Absorption

In the previous chapter we cataloged 36 AGN with intrinsic absorption. We found 11 new UV intrinsic absorption objects in a sample of 72 nearby AGN observed by *FUSE*. We continue our study of that absorption by measuring the absorption lines we found in the 36 objects.

5.1 Optical Observations and Measurements

We obtained ground based optical spectra to determine redshifts and/or estimate black-hole masses and to supplement the *FUSE* data for three objects: IRAS F22456-5125, MR 2251-178 and WPVS 007. These data are readily available in the literature for most of the other objects. Each galaxy was observed in both the blue and red optical regions with the R-C spectrograph on the Cerro Tololo Inter-American Observatory (CTIO) 1.5-m telescope in Chile. Table 5.1 chronicles the dates, integration times and wavelength coverage for these data. The blue spectra (spanning approximately 3360 to 5440 Å) were taken using a grating with a dispersion of ∼1.47 Å/pixel, providing a resolution of 4.3 Å. The red spectra (5652 to 6972 Å) were taken using a Schott GG495 filter and a grating with a 1.10 Å/pixel dispersion grating, giving us a resolution of 3.1 Å. All objects were observed through a long slit with a width of 4″. The stars LTT 4364 and Feige 110 were observed with the same settings for the

purpose of flux calibration. The spectra were reduced and calibrated using standard IRAF reduction packages for long-slit spectroscopy. We show the reduced spectra in Figure 5.1.

Table. 5.1: Observation Log

Object	Date	Integration Time (s)	Resolution FWHM (Å)	λ Coverage (Å)
IRAS F22456-5125	2007 August 9	2400	4.3	3667-5409
IRAS F22456-5125	2007 August 16	2400	3.1	5639-6947
MR 2251-178	2007 August 15	2400	4.3	3667-5423
MR 2251-178	2007 August 17	2400	3.1	5639-6947
WPVS 007	2007 August 15	2400	4.3	3667-5423
WPVS 007	2007 August 17	1800	3.1	5639-6947

For the source IRAS F22456-5125, which had a redshift estimate listed on NED of 0.1 (Mason et al. 1995), we used our spectra to estimate the redshift based on the positions of lines in the blue spectrum. The centroids of the emission lines [O II] λ3727, [Ne III] λ3869, [Ne V] λ3424 and Hβ were available in the wavelength coverage of the blue setting and we found an average redshift of z=0.1016$\pm$0.0001. The redshifts from NED for WPVS 007 and MR-2251-178 are consistent with our measurements.

The optical spectra allowed us to determine mass estimates for the central supermassive black hole (SMBH) of these objects via the empirical relationships between SMBH mass and the Hβ FWHM and continuum luminosity at λ=5100Å (or, equivalently the Hβ line luminosity) calibrated by Vestergaard & Peterson (2006) using

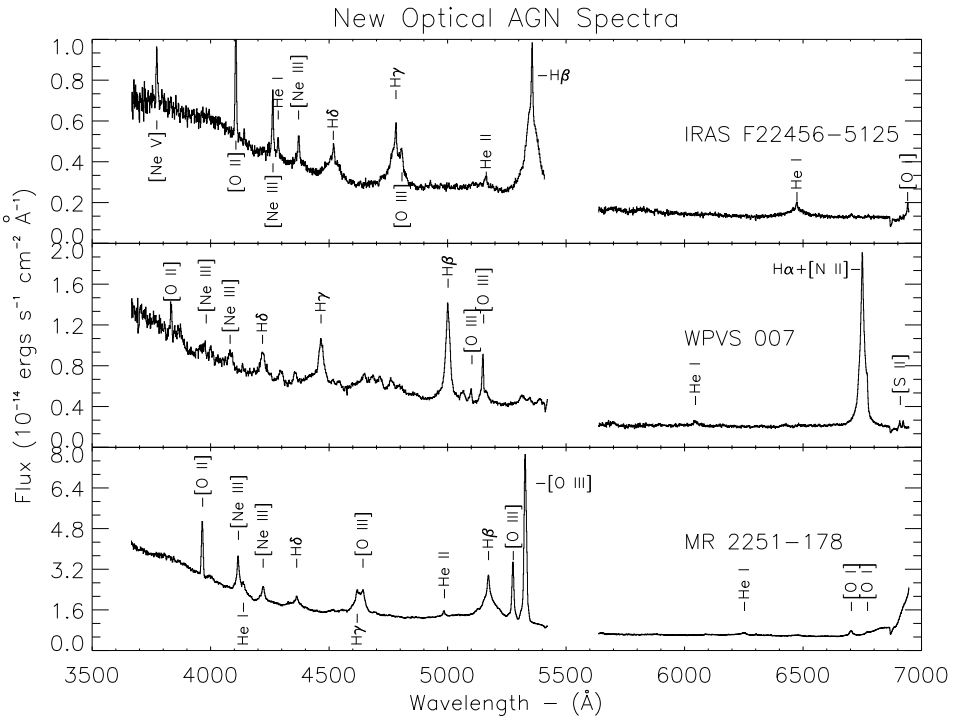

Figure. 5.1: New spectra taken at CTIO, plotted in the observed frame.

emission-line reverberation mapping. We present these masses along with the masses of the rest of the sample later in this chapter.

5.2 UV Observations and Measurement

5.2.1 Light Curves

Generating a continuum light curve for *FUSE* data proved to be a difficult task due to the nature of the two detectors and redshifted broad emission lines. Using the same method described by Dunn et al. (2006), we chose 1110 Å in the observed frame as a good position to measure the continuum flux. In a 10 Å bin, both detectors contribute

to the measured flux at that wavelength. In some spectra from either the LiF detector or the SiC detector, the target was sometimes out of the aperture. In these cases we did not include the segments. Also, due to redshift considerations, we were forced to move the bin when the redshift was ≥ 0.06. At those particular redshifts the broad line would provide a measured flux value too high for the continuum by up to 20-30%. For the majority of the observations, the flux we provide is an average flux within the 10 Å bin at 1110 Å; this avoids ISM lines (Morton 1991) and geocoronal dayglow lines (Feldman et al. 2001). The rest of the observations were measured in a 20 Å bin taken at 1160 or 1020 Å, depending on which bin was closest to and unaffected by the O VI broad line. We converted our fluxes to log specific luminosity, and provide flux, log luminosity, bin position, and errors in Table 5.2.

Table. 5.2: AGN Continuum Levels

Object	Observation ID	Julian Date +2400000 days	Flux[a] $\times 10^{-14}$	Bin Position (Å)	Log L_λ ergs s^{-1} $Å^{-1}$	σ_{LogL_λ} ergs s^{-1} $Å^{-1}$
WPVS 007	D8060201000	52950.360	0.48	1020	39.88	0.11
QSO0045+3926	Z0020401000	51874.176	1.01	1110	41.54	0.03
	D1310101000	52921.336	1.34	1110	41.66	0.05
	D1310102000	52922.707	1.40	1110	41.68	0.05
	D1310103000	52924.391	1.14	1110	41.60	0.04
	D1310104000	52983.242	0.88	1110	41.48	0.06
	D1310105000	53335.281	1.28	1110	41.65	0.07
	D1310106000	53336.105	1.24	1110	41.63	0.07
	D1310107000	53337.000	1.23	1110	41.63	0.07
TONS180	P1010502000	51524.742	6.16	1160	41.66	0.05
	D0280101000	53199.973	4.49	1160	41.52	0.05
MRK1044	D0410101000	53006.246	2.52	1020	40.12	0.09
NGC985	P1010903000	51536.551	2.45	1020	40.94	0.05
EUVEJ0349-537	E8970301000	53237.559	0.36	1110	41.06	0.04
IRASF04250-5718	D8080801000	52886.609	3.66	1110	41.89	0.07
MRK79	P1011701000	51512.949	1.15	1110	40.04	0.11
	P1011702000	51558.152	1.13	1110	40.03	0.10
	P1011703000	51596.613	1.41	1110	40.12	0.08
MRK10	Z9072801000	52673.195	1.07	1110	40.24	0.11
IR07546+3928	S6011801000	52317.062	0.11	1160	40.29	0.08
PG0804+761	P1011901000	51456.504	7.84	1160	42.18	0.01
	P1011903000	54548.312	14.08	1160	42.44	0.02
	S6011001000	52311.059	5.72	1160	42.05	0.02
	S6011002000	52315.406	5.90	1160	42.06	0.02
Ton951	P1012002000	53080.004	4.62	1160	41.56	0.06
	D0280304000	51595.316	3.42	1160	41.43	0.03
	D0280301000	53079.102	2.90	1160	41.36	0.07
IRAS09149-62	A0020503000	51581.129	1.42	1110	40.95	0.04
	S7011003000	53461.098	0.80	1110	40.70	0.09

Continued on Next Page...

Table. 5.2 – Continued

Object	Observation ID	Julian Date +2400000 days	Flux[a] $\times 10^{14}$	Bin Position (Å)	Log L_λ ergs s^{-1} $Å^{-1}$	σ_{LogL_λ} ergs s^{-1} $Å^{-1}$
	U1072202000	53929.031	0.74	1110	40.67	0.06
MKN141	D8061001000	53085.585	0.07	1110	39.09	0.38
NGC3516	P1110404000	51651.957	1.24	1020	38.97	0.18
	G9170101000	53776.217	0.69	1020	38.71	0.20
	G9170102000	54123.776	0.63	1020	38.67	0.23
ESO265-G23	A1210405000	51978.219	0.38	1110	40.36	0.13
	A1210407000	52341.223	0.39	1110	40.37	0.07
	A1210408000	52393.352	0.73	1110	40.64	0.03
	A1210409000	52394.416	1.03	1110	40.79	0.04
NGC3783	P1013301000	51576.621	4.90	1160	39.95	0.03
	B1070102000	51969.199	4.94	1160	39.95	0.03
	B1070103000	51979.535	3.49	1160	39.80	0.03
	B1070104000	51999.453	5.81	1160	40.02	0.03
	B1070105000	52087.727	4.47	1160	39.91	0.04
	B1070106000	51975.855	2.87	1160	39.72	0.03
	E0310101000	53130.965	4.11	1160	39.87	0.03
NGC4051	B0620201000	52362.582	1.29	1020	38.13	0.05
	C0190101000	52657.988	1.35	1020	38.15	0.07
	C0190102000	52717.824	1.51	1020	38.20	0.07
NGC4151	P1110505000	51609.410	2.50	1020	38.72	0.05
	P2110201000	52008.199	1.71	1020	38.56	0.08
	C0920101000	52423.469	21.52	1020	39.66	0.03
	P2110202000	52427.199	12.67	1020	39.43	0.05
RXJ1230.8+0115	P1019001000	51715.832	5.24	1110	42.14	0.06
TOL1238-364	D0100101000	51945.742	1.47	1110	39.53	0.06
PG1351+640	P1072501000	51562.117	1.19	1160	41.25	0.03
	S6010701000	52306.922	1.68	1160	41.40	0.02
MRK279	P1080303000	51540.527	11.45	1110	41.31	0.01
	P1080304000	51554.562	9.61	1110	41.23	0.02
	C0900201000	52413.258	0.61	1110	40.04	0.02
	D1540101000	52772.410	9.20	1110	41.21	0.01

Continued on Next Page...

Table. 5.2 – Continued

Object	Observation ID	Julian Date +2400000 days	Flux[a] $\times 10^{14}$	Bin Position (Å)	Log L_λ ergs s^{-1} $Å^{-1}$	σ_{LogL_λ} ergs s^{-1} $Å^{-1}$
	F3250103000	53711.961	7.35	1110	41.12	0.02
	F3250104000	53713.277	2.86	1110	40.70	0.08
	F3250106000	53769.598	4.53	1110	40.90	0.05
RXJ135515+561244	D8061601000	52712.387	0.39	1110	41.04	0.02
PG1404+226	P2100401000	52071.652	0.93	1110	41.23	0.10
PG1411+442	A0601010000	51675.637	2.01	1160	41.49	0.06
NGC5548	P1014601000	51703.055	1.55	1020	39.94	0.05
MRK817	P1080401000	51591.965	9.05	1110	41.23	0.03
	P1080402000	51592.766	7.20	1110	41.13	0.03
	P1080403000	51902.176	3.89	1110	40.87	0.003
	P1080404000	51958.891	6.25	1110	41.07	0.01
MRK290	P1072901000	51620.230	0.45	1110	39.87	0.08
	D0760101000	52819.457	3.44	1110	40.76	0.06
	E0840101000	53171.730	3.83	1110	40.81	0.06
MRK876	P1073101000	51467.766	0.24	1110	40.88	0.03
	D0280201000	52776.450	5.77	1110	42.26	0.08
	D0280203000	53049.797	5.71	1110	42.26	0.03
MRK509	X0170101000	51485.445	7.41	1020	41.23	0.05
	X0170102000	51488.703	8.00	1020	41.26	0.06
	P1080601000	51792.750	9.14	1020	41.32	0.05
IIZW136	P1018301000	51863.473	2.36	1160	41.25	0.04
	P1018302000	53152.684	3.72	1160	41.45	0.07
	P1018303000	53153.727	2.79	1160	41.33	0.07
	P1018304000	53310.586	3.71	1160	41.45	0.04
AKN564	B0620101000	52089.816	1.03	1110	40.08	0.02
IRAS F22456-5125	Z9073901000	52541.902	1.12	1110	41.33	0.10
	Z9073902000	52542.457	1.75	1110	41.52	0.04
	E8481401000	53194.629	6.08	1110	42.07	0.08
MR 2251-178	P1111010000	52081.012	0.99	1160	40.89	0.04
NGC7469	P1074101000	51724.101	1.30	1020	39.52	0.08
	C0900101000	52621.797	2.11	1020	39.73	0.14

Continued on Next Page...

Table. 5.2 – Continued

Object	Observation ID	Julian Date +2400000 days	Flux[a] $\times 10^{14}$	Bin Position (Å)	Log L_λ ergs s^{-1} $Å^{-1}$	σ_{LogL_λ} ergs s^{-1} $Å^{-1}$
	C0900102000	52621.767	2.17	1020	39.74	0.15

[a] Flux in ergs s^{-1} cm^{-2} $Å^{-1}$

5.2.2 Measured Absorption Quantities

We measured the equivalent width, FWHM and radial velocity centroid with respect to systemic redshift of each intrinsic absorption feature identified in §4. These measurements are listed in Table 5.3 for the Lyβ, O VI λ 1032 (O VIb) and O VI λ 1038 (O VIr) lines. Many features were blended or too contaminated by galactic absorption features to be measured accurately. Because *FUSE* has no onboard calibration lamp and has wavelength inaccuracies of up to 20 km s^{-1}, to correct the velocities we measured available ISM lines near our intrinsic absorption features, in order to avoid nonlinear calibration effects. These corrections have already been accounted for in our velocities in Table 5.3. We list explanations of our measured and unmeasured lines for each object in Appendix B.

Table. 5.3: Measured Absorption Parameters

Object	**Obs ID**	**Component**	**Equivalent Width**			σ_{EW}			**FWHM**			$\mathbf{V}_r$	σ_V
			Lyβ (Å)	O VIb (Å)	O VIr (Å)	Lyβ (Å)	O VIb (Å)	O VIr (Å)	Lyβ	O VIb (km s^{-1})	O VIr	(km s^{-1})	(km s^{-1})
WPVS 007	D8060201000	1	1.91	2.06	1.76	0.14	0.13	0.14	714	639	615	-397	26
QSO0045+3926	Z0020401000	1	0.29	0.61	0.29	0.04	0.06	0.05	100	172	69	361	13
	D1310101000	1	0.19	0.45	0.38	0.01	0.01	0.01	56	128	98	351	5
	D1310102000	1	0.19	0.38	0.29	0.02	0.02	0.02	69	101	107	345	12
	D1310103000	1	0.29	0.41	0.27	0.08	0.06	0.06	77	121	63	340	22
	D1310104000	1	0.17	0.36	0.31	0.01	0.02	0.02	82	107	74	346	16
	D1310105000	1	0.13	0.40	0.33	0.02	0.02	0.02	86	107	94	371	6
	D1310106000	1	0.16	0.42	0.28	0.02	0.02	0.02	69	91	85	375	7
	D1310107000	1	0.14	0.33	0.32	0.02	0.03	0.02	60	77	73	396	9
TONS180	P1010502000	1			0.13			0.03			65	-1732	
	D0280101000	1			0.17			0.03			85	-1792	
MRK1044	D0410101000	1	0.20	0.22		0.04	0.03		65	92		-1110	2
NGC985	P1010903000	1		0.11	0.06		0.01	0.01		96	77	-814	20
	P1010903000	2	0.12	0.26	0.20	0.02	0.01	0.01	34	72	55	-678	6
	P1010903000	3	0.56	0.71	0.65	0.02	0.02	0.01	158	199	180	-454	51
	P1010903000	4	0.15	0.16	0.23	0.02	0.01	0.01	41	44	63	-268	17
EUVEJ0349-537	E8970301000	1	0.47	0.71	0.60	0.04	0.04	0.06	128	218	165	26	21
IRASF04250-5718	D8080801000	1	0.56	0.62	0.64	0.06	0.07	0.07	159	195	184	-216	5
	D8080801000	2	0.15	0.25	0.20	0.06	0.03	0.03	41	66	51	-64	2
MRK79	P1011701000	1	0.35	0.65	0.76	0.18	0.17	0.17	117	242	220	-350	12
	P1011702000	1	0.30	0.52	0.43	0.10	0.09	0.08	175	240	160	-325	35
	P1011703000	1	0.18	0.57	0.52	0.07	0.08	0.06	86	198	194	-326	27
	P1011701000	2			0.39			0.13			255	-1404	
	P1011702000	2			0.31			0.08			87	-1387	
	P1011703000	2			0.28			0.07			81	-1367	
MRK10	Z9072801000	1	1.03		0.92	0.09		0.13	1.21		0.81	-126	18
IR07546+3928	S6011801000	1	1.07	1.49	1.00	0.05	0.03	0.02	280	436	351	-1777	9
	S6011801000	2	0.98	1.48	1.37	0.03	0.03	0.03	263	395	361	-1116	12

Continued on Next Page...

Table. 5.3 – Continued

Object	Obs ID	Component	Equivalent Width			σ_{EW}			FWHM			V_r	σ_V
			Lyβ (Å)	O VIb (Å)	O VIr (Å)	Lyβ (Å)	O VIb (Å)	O VIr (Å)	Lyβ	O VIb (km s^{-1})	O VIr	(km s^{-1})	(km s^{-1})
PG0804+761	P1011901000	1	0.21	0.13	0.09	0.004	0.003	0.003	69	67	64	363	7
	P1011903000	1	0.23	0.14	0.06	0.01	0.01	0.01	75	66	55	370	2
	S6011001000	1	0.19	0.11	0.10	0.01	0.004	0.01	63	64	81	356	1
	S6011002000	1	0.20	0.11	0.09	0.01	0.01	0.01	74	66	71	358	5
TON951	P1012002000	1	0.60	0.43	0.43	0.02	0.01	0.01	159	123	118	179	16
	D0280304000	1	0.69	0.42	0.46	0.05	0.03	0.02	190	150	128	173	25
	D0280301000	1	0.66	0.52	0.41	0.05	0.05	0.02	186	149	114	149	23
IRAS09149-62	A0020503000	1		1.72	1.26		0.22	0.12		504	389	18	18
	S7011003000	1			1.08			0.11			377	31	
	U1072202000	1			1.33			0.08			431	56	
NGC3516	P1110404000	1	0.27	1.76	0.06	0.07	0.09	0.03	168	510	52	-1511	360
	G9170101000	1	0.33	1.40	0.14	0.13	0.17	0.20	177	468	133	-1362	6.8
	G9170102000	1	0.23	0.53	0.15	0.07	0.07	0.04	133	202	63	-1343	101
	P1110404000	2		0.54	0.08		0.06	0.05		250	162	-866	125
	G9170101000	2	0.38	0.57	0.64	0.16	0.12	0.20	212	239	331	-888	38
	G9170102000	2	0.15	0.28	0.34	0.06	0.05	0.05	112	99	198	-911	52
	P1110404000	3		0.28	0.35		0.04	0.03		123	46	-410	15
	G9170101000	3	0.38		0.58	0.15		0.12	168		196	-460	10
	G9170102000	3	0.34	0.32	0.38	0.06	0.06	0.05	113	98	100	-456	2
	P1110404000	4	0.38	0.38	0.40	0.08	0.05	0.06	110	163	239	-216	1
	G9170101000	4	0.58		0.46	0.17		0.23	226		174	-236	30
	G9170102000	4	0.67	0.79	0.80	0.06	0.06	0.07	233	287	302	-227	6
ESO265-G23	A1210405000	1		0.29	0.15		0.15	0.09		127	126	-178	13
	A1210407000	1		0.34	0.32		0.05	0.04		141	73	-157	5
	A1210408000	1		0.29	0.36		0.10	0.08		63	288	-124	14
	A1210409000	1		0.34	0.30		0.13	0.10		92	81	-157	26
NGC3783	P1013301000	1	1.03	1.19	0.78	0.02	0.02	0.03	403	463	404	-660	10
	B1070102000	1	1.12	1.18	0.62	0.03	0.02	0.03	394	467	456	-668	20
	B1070103000	1	1.11	1.19	0.70	0.04	0.03	0.03	400	452	449	-663	16
	B1070104000	1	0.99	1.12	0.78	0.03	0.03	0.02	332	443	393	-675	19

Continued on Next Page...

Table. 5.3 – Continued

Object	Obs ID	Component	Equivalent Width			σ_{EW}			FWHM			V_r	σ_V
			Lyβ (Å)	O VIb (Å)	O VIr (Å)	Lyβ (Å)	O VIb (Å)	O VIr (Å)	Lyβ	O VIb (km s^{-1})	O VIr	(km s^{-1})	(km s^{-1})
	B1070105000	1	0.88	1.16	0.65	0.03	0.03	0.03	377	459	404	-682	13
	B1070106000	1	1.17	1.20	0.76	0.04	0.03	0.03	427	457	395	-664	12
	E0310101000	1	1.05	1.30	0.80	0.02	0.03	0.02	380	467	371	-657	30
NGC4051	B0620201000	1		2.28			0.00			672		-374	
	C0190101000	1		2.13			0.04			696		-348	
	C0190102000	1		2.14	1.88		0.05	0.04		670	627	-359	12
NGC4151	P1110505000	1		0.91			0.04			473		-706	
	P2110201000	1		1.48	1.21		0.07	0.04		514	522	-574	222
	C0920101000	1		1.77	1.95		0.01	0.01		718	681	-397	41
	P2110202000	1		1.66	1.99		0.08	0.05		662	716	-413	56
RXJ1230.8+0115	P1019001000	1		1.90	1.57		0.09	0.08		542	476	-2994	16
	P1019001000	2		0.27	0.26		0.06	0.05		71	69	-2420	50
	P1019001000	3		1.19	1.07		0.08	0.06		311	278	-2014	3
	P1019001000	4		1.17	1.08		0.06	0.08		304	280	120	2
TOL1238-364	D0100101000	1		1.10	1.51		0.14	0.15		339	454	-252	75
PG1351+640	P1072501000	1	0.60	1.31	1.20	0.01	0.01	0.01	182	453	447	-1705	73
	S6010701000	1	0.54	1.37	1.42	0.02	0.02	0.02	208	455	429	-1715	60
	P1072501000	2	1.51	2.08	1.94	0.02	0.01	0.01	407	559	516	-883	24
	S6010701000	2	1.23	2.16	2.12	0.02	0.02	0.02	333	579	565	-899	11
MRK279	P1080303000	1	0.77	1.20	0.75	0.01	0.01	0.01	321	478	301	-312	6
	P1080304000	1	0.82	1.15	0.77	0.02	0.02	0.02	328	482	307	-328	4
	C0900201000	1	1.01	0.96	1.06	0.07	0.06	0.06	299	497	312	-351	2
	D1540101000	1	0.76	1.32	0.97	0.01	0.01	0.01	290	474	319	-308	8
	F3250103000	1	1.19	1.80	0.97	0.13	0.10	0.10	285	508	306	-404	33
	F3250104000	1	0.87	1.64	0.93	0.13	0.13	0.11	392	518	366	-302	12
	F3250106000	1	0.69	1.26	0.90	0.22	0.21	0.16	324	502	328	-308	28
RXJ135515+561244	D8061601000	1	0.34	0.61	0.76	0.04	0.04	0.05	86	160	205	-834	12
	D8061601000	2		0.69	0.48		0.05	0.03		180	186	-163	28
PG1404+226	P2100401000	1	0.19	0.54	0.36	0.04	0.03	0.04	88	151	127	-166	57
	P2100401000	2		1.47	1.11		0.06	0.07		330	284	134	17

Continued on Next Page...

Table. 5.3 – Continued

Object	Obs ID	Component	Equivalent Width			σ_{EW}			FWHM			V_r	σ_V
			Lyβ (Å)	O VIb (Å)	O VIr (Å)	Lyβ (Å)	O VIb (Å)	O VIr (Å)	Lyβ	O VIb (km s^{-1})	O VIr	(km s^{-1})	(km s^{-1})
PG1411+442	A0601010000	1			0.64			0.03			170	55	
NGC5548	P1014601000	1		0.35	0.25		0.02	0.02		161	195	-441	4
	P1014601000	2		0.25	0.31		0.02	0.02		111	142	-683	5
MRK817	P1080401000	1	0.08	0.60	0.41	0.05	0.04	0.05	319	207	143	-4198	5
	P1080402000	1	0.12	0.51	0.39	0.05	0.05	0.06	236	237	146	-4184	16
	P1080403000	1	0.10	0.41	0.36	0.01	0.02	0.02	134	273	265	-4166	32
	P1080404000	1	0.06	0.40	0.33	0.01	0.00	0.01	210	208	154	-4144	12
	P1080404000	2		0.12	0.05		0.01	0.01		243	142	-3680	27
	P1080404000	3		0.12	0.09		0.01	0.01		118	139	-2966	6
MRK290	P1072901000	1	0.71	0.62	0.54	0.12	0.10	0.08	185	190	142	-225	14
	D0760101000	1	0.51	0.59	0.48	0.07	0.05	0.05	141	192	165	-212	17
	E0840101000	1	0.54	0.48	0.43	0.05	0.05	0.05	180	157	158	-187	72
MRK876	P1073101000	1		0.11	0.09		0.01	0.01		73	99	-3735	3
	D0280203000	1		0.15	0.11		0.00	0.00		101	94	-3724	0.8
MRK509	X0170101000	1	0.55	0.70	0.52	0.02	0.01	0.01	217	217	182	-305	16
	X0170102000	1	0.65	0.80	0.58	0.03	0.02	0.02	218	204	190	-304	19
	P1080601000	1	0.61	0.67	0.56	0.01	0.01	0.01	170	201	177	-300	18
	X0170101000	2	0.95	1.23	1.12	0.02	0.01	0.01	303	329	346	103	12
	X0170102000	2	1.05	1.27	1.16	0.03	0.02	0.03	321	331	322	27	11
	P1080601000	2	1.15	1.15	1.19	0.01	0.01	0.01	330	333	341	90	12
IIZW136	P1018301000	1		0.42			0.02			146		-1487	
	P1018302000	1		0.47			0.03			173		-1512	
	P1018303000	1		0.49			0.04			96		-1517	
	P1018304000	1		0.45			0.03			167		-1512	
	P1018301000	2			0.28			0.02			87	9	
	P1018302000	2			0.30			0.04			96	-2	
	P1018303000	2			0.18			0.03			61	9	
	P1018304000	2			0.31			0.02			99	-7	
AKN564	B0620101000	1	1.64	1.28	1.31	0.04	0.02	0.03	528	304	280	-65	10
IRAS F22456-5125	Z9073901000	1	0.06	0.32	0.28	0.04	0.06	0.06	42	110	105	-787	11

Continued on Next Page...

Table. 5.3 – Continued

Object	**Obs ID**	**Component**	**Equivalent Width**			σ_{EW}			**FWHM**			**V**$_r$	σ_V
			Lyβ (Å)	O VIb (Å)	O VIr (Å)	Lyβ (Å)	O VIb (Å)	O VIr (Å)	Lyβ	O VIb (km s^{-1})	O VIr	(km s^{-1})	(km s^{-1})
	Z9073902000	1	0.07	0.19	0.17	0.01	0.01	0.01	81	64	69	-803	22
	E8481401000	1	0.06	0.24	0.29	0.05	0.04	0.07	50	73	99	-812	28
	Z9073901000	2	0.42			0.05			130			-596	
	Z9073902000	2	0.35			0.01			97			-612	
	E8481401000	2	0.44			0.06			110			-617	
	Z9073901000	3	0.38	0.23	0.25	0.06	0.05	0.05	117	66	101	-424	9
	Z9073902000	3	0.27	0.20	0.21	0.01	0.01	0.01	77	67	69	-455	5
	E8481401000	3	0.33	0.38	0.26	0.05	0.06	0.06	96	151	94	-447	13
	Z9073901000	4	0.09	0.17	0.10	0.05	0.05	0.04	56	66	42	-311	3
	Z9073902000	4	0.08	0.21	0.14	0.01	0.01	0.01	40	63	66	-323	5
	E8481401000	4	0.12	0.18	0.14	0.05	0.05	0.04	35	105	39	-327	1
	Z9073901000	5	0.70	0.51	0.54	0.08	0.06	0.07	190	142	143	-118	19
	Z9073902000	5	0.68	0.67	0.46	0.01	0.01	0.01	182	136	134	-135	22
	E8481401000	5	0.72	0.54	0.57	0.07	0.06	0.07	178	147	137	-136	21
MR 2251-178	P1111010000	1	1.62	0.70	0.40	0.03	0.01	0.01	418	234	155	-300	23
NGC7469	C0900101000	1		0.40	0.30		0.002	0.01		151	137	-1847	17
	C0900102000	1		0.48	0.40		0.01	0.01		209	190	-1878	3

5.3 Correlations

All of our correlations show measurements from each absorption component in each observation, because many of the quantities can be variable over time. The most tantalizing correlation we found is that of velocity with specific luminosity (L_λ. While this was seen in C IV by Laor & Brandt (2002), their objects were mostly quasars with high luminosities and redshifts beyond 0.15, which was our redshift cutoff on the high end. We share four objects in common. We plot in Figure 5.2 all of our velocities measured for each object and each component. In general as the luminosity increases, it appears that the maximum velocity at each luminosity does as well. This confirms the trend that Laor & Brandt found for higher luminosity objects and shows that the trend also holds for lower luminosity objects such as Seyfert galaxies. To confirm this further, we converted the magnitudes provided by Laor & Brandt to log L_λ by using the four targets we share and found a scale factor of 1.7. We plot the Laor & Brandt observations along with our own measurements in Figure 5.3 and see that the two data sets follow remarkably similar trends. The relation given in Laor & Brandt is $v_{max} \propto L^{0.62\pm0.08}$.

Along with the black hole masses measured from the optical data, we compiled all of the known masses for our survey objects in Table 5.4 (we exclude those few without the necessary measured quantities) and calculated the Eddington ratio. For all objects referencing Peterson et al. (2004), the masses are from reverberation mapping; all others were calculated using the relationship found by Kaspi et al. (2000) and recently

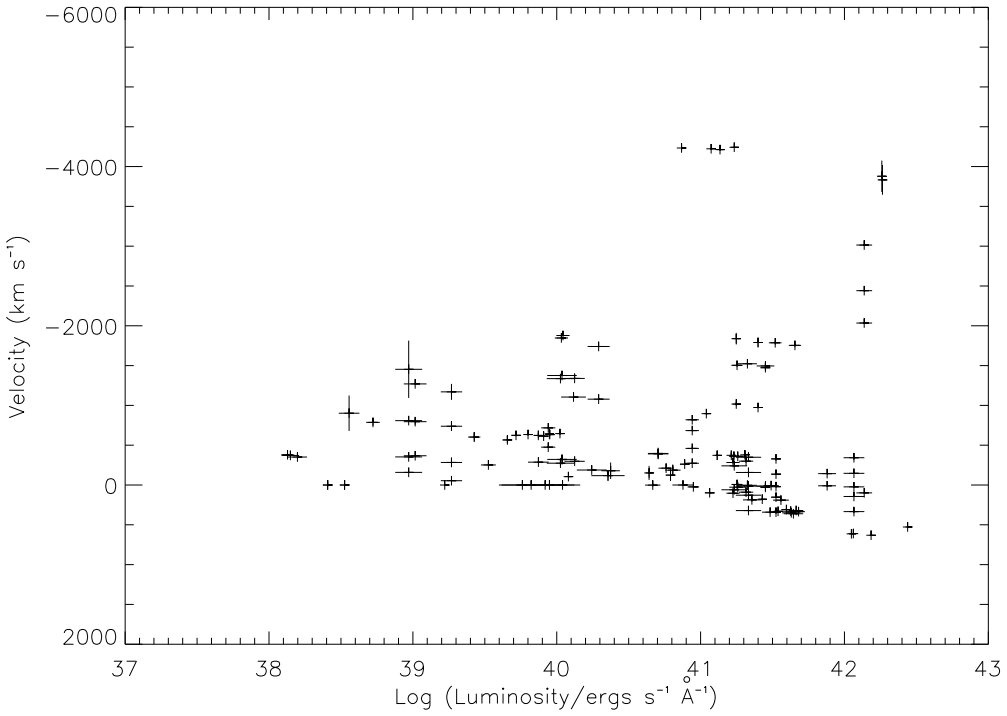

Figure. 5.2: The relation between luminosity and velocity using only data from *FUSE*.

calibrated by Vestergaard & Peterson (2006):

$$logM_{BH}(H\beta) = log\left[\left(\frac{FWHM(H\beta)}{1000\text{ km s}^{-1}}\right)^2\left(\frac{\lambda\, L_{5100}}{10^{43}\text{ ergs s}^{-1}}\right)^{0.5}\right] + (6.91 \pm 0.02) \quad (5.1)$$

using the FWHM of the broad Hβ emission line and the luminosity at 5100 Å.

We plot the maximum velocity, against Eddington ratio (L/L_{Edd}) in Figure 5.4. There appears to be no trend of maximum velocity with Eddington ratio. It should be noted that the two objects with the highest velocities have low ratios, and the one object with a high ratio has a low velocity. In order to complete the picture we would require more data and a wider range of objects spanning the range of ratios, as most of our targets are moderate Eddington accreting objects. In the future RXJ

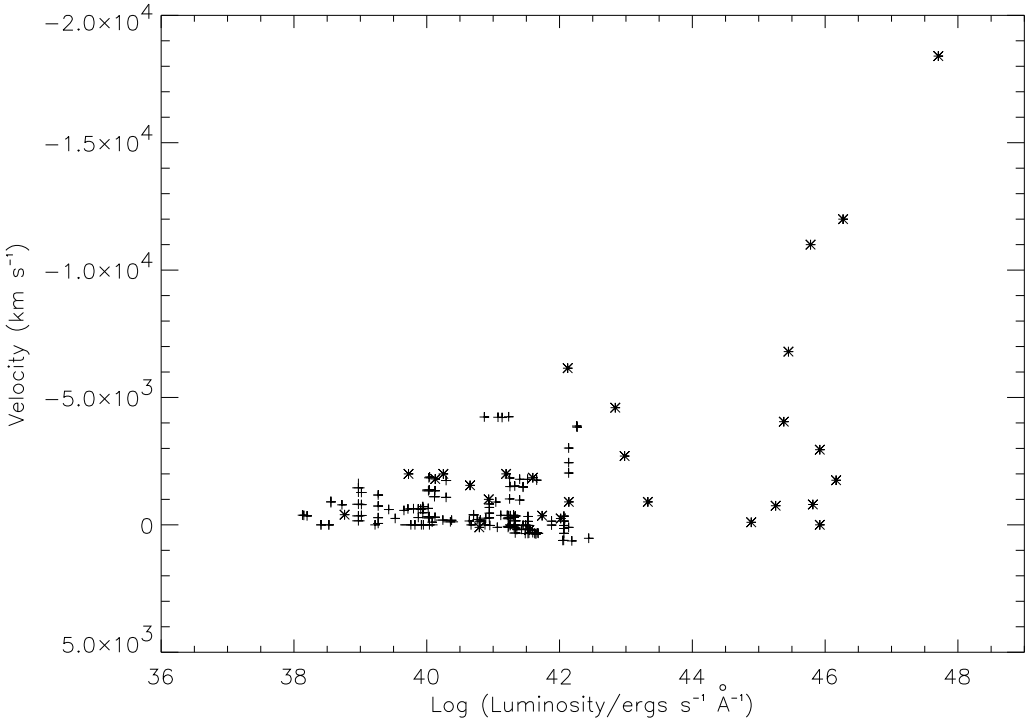

Figure. 5.3: Extended plot of luminosity and velocity using data from *FUSE* (+) and data measured by Laor & Brandt (2002) (*).

1230.8+0115 would be a good target for measuring due to its relatively high outflow velocity ($\sim$3000 km s^{-1}) for component 1 and mid-range velocities for components 2 and 3.

Table. 5.4: Black Hole Masses

Object	FWHM Hβ km s^{-1}	Mass $\times 10^6$	log λL_λ ergs s^{-1}	log L_{Bol} ergs s^{-1}	L/L_{Edd}	reference[b]
Mrk 79		52.4	43.72	44.71	0.08	1
PG 0804+761		693	44.94	45.93	0.10	1
NGC 3516		42.7	42.88	43.87	0.01	1
NGC 3783		29.8	43.26	44.25	0.05	1
NGC 4051		1.91	41.93	42.92	0.03	1
NGC 4151		13.3	42.88	43.87	0.04	1
Mrk 279		34.9	43.88	44.87	0.17	1
PG 1411+422		443	44.63	45.62	0.07	1
NGC5548		67.1	43.51	44.50	0.04	1
Mrk 817		49.4	43.82	44.81	0.10	1
Mrk 509		143	44.28	45.27	0.10	1
NGC 7469		12.2	43.72	44.71	0.33	1
Mrk 876		279	44.98	45.97	0.27	1
Ton 951		92.4	44.35	45.34	0.19	1
II Zw 136		457	44.46	45.45	0.05	1
PG 1351+640	1170	46	44.64	45.63	0.74	2
QSO 0045+3926	5970	564.9	44.60	45.59	0.05	7
Ton S180	970	10.2	44.27	45.26	1.42	3
NGC 985	5670	202.8	43.80	44.79	0.02	3
IRAS F04250-5718	2580	144.0	44.87	45.86	0.40	3
Mrk 10	3050	25.6	43.08	44.07	0.04	4
IR 07546+3928	2120	176.9	45.39[a]	46.39	1.10	8
Mrk 141	3600	65.0	43.60	44.59	0.05	3
RXJ 135515+561244	1100	9.4	43.98	44.97	0.79	3
PG 1404+226	790	7.7	44.38	44.37	2.43	5
Mrk 290	5320	157.3	43.69	44.68	0.02	5
Akn 564	970	4.8	43.62	44.61	0.67	4
MR 2251-5125	3768	240.0	44.64	45.63	0.14	6
IRAS F22456-5125	3297	154.9	42.76[a]	45.53	0.16	6
WPVS 007	1502	11.5	43.59	44.58	0.27	6

[a] Mass calculated from Hβ luminosity

[b] 1-Peterson et al. 2004, 2-Kaspi et al. 2000, 3-Grupe et al. 2004, 4-Botte et al. 2004, 5-Vestergaard et al. 2006 6-CTIO data, 7-Xu et al. 2003, 8-Marziani et al. 2003

[c] $L_{Bol} = 9.8\ \lambda L_{5100}$ (McLure & Dunlop 2004)

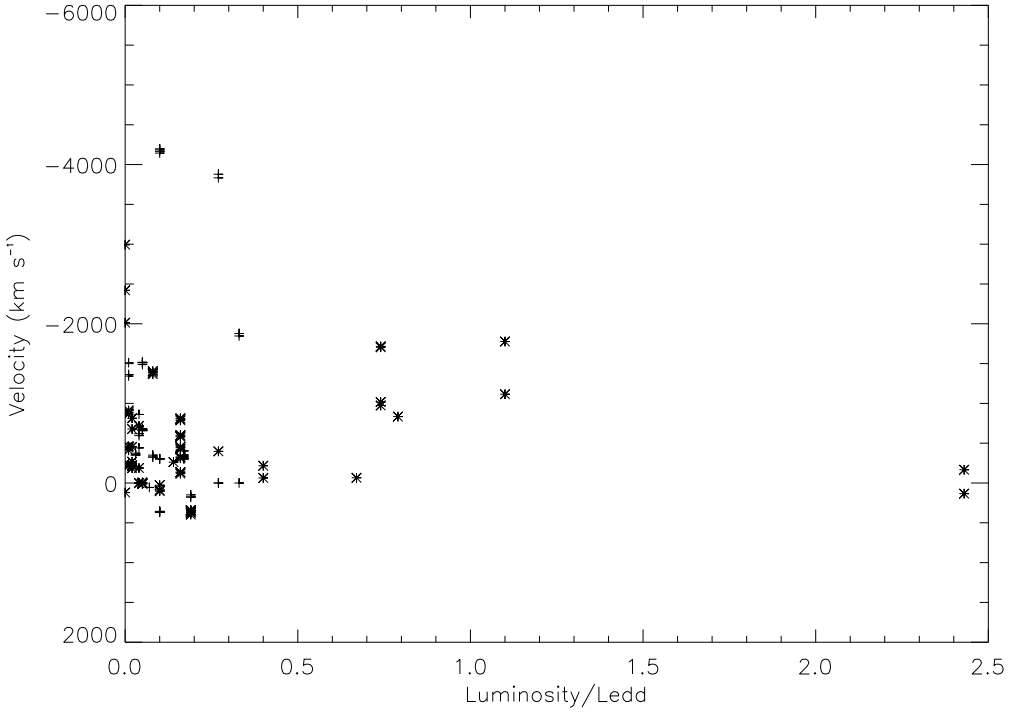

Figure. 5.4: Relationship between Eddington Ratio and maximum outflow velocity. Crosses are objects with reverberation mapping.

We examined how the equivalent width relates to the specific luminosity in our sample, which we show in Figure 5.5. Overall there appears to be no trend. The only notable feature in the plot is the lack of points for low luminosity and low EW. The paucity of points is most likely a selection effect of low signal-to-noise for weak lines in objects with low continuum fluxes. It should be noted that some of our EWs were measured over what have been seen, in less saturated UV absorption lines, to be multiple components (e.g., NGC 4151 in Kraemer et al. (2005)). Due to the heavy blending and saturation in O VI, we simply measure across blends as one component. We also tested for correlation by removing any measurements of lines in spectra with a

luminosity signal-to-noise of < 30 and measurements from spectra that are saturated with multiple components, and still found that there is no trend.

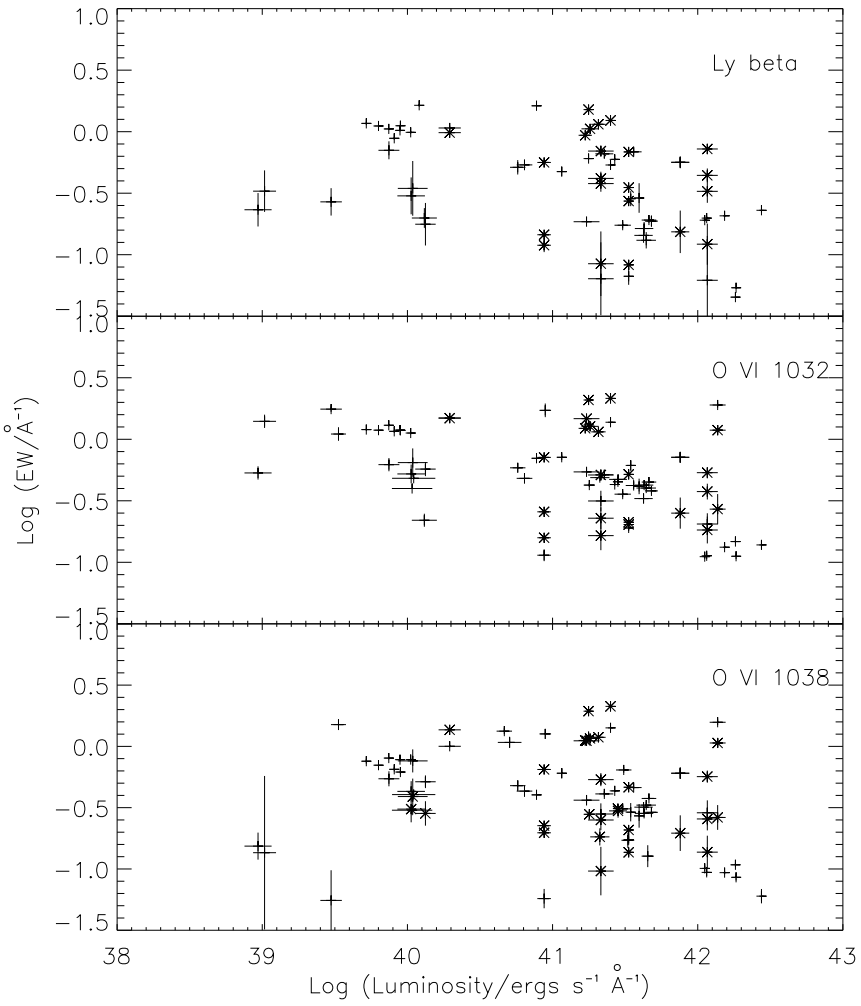

Figure. 5.5: EW vs. specific luminosity for our sample. The bottom plot is for O VI λ1038, the middle is for O VI λ1032 and the top plot is for Ly β. Plus symbols are components we label 1 and asterisks any component other than the first.

We additionally investigated the relation between EW and maximum velocity (not shown). Again, there appears to be very little trend save for the fact that in objects

such as Mrk 817 and Mrk 876 where the velocity is on the order of 3000 km s^{-1}, the EW is comparatively small. We also examined the relation between full width at half maximum and the specific luminosity, as shown in Figure 5.6. There appears to be essentially no relation between FWHM and velocity (not shown). However, there does appear to be a lack of very narrow absorption for O VI at low luminosities.

5.4 Variability

Our survey is the first to date with a significant number of objects with multiple spectra to provide enough data for a time series analysis of intrinsic absorption variability in the far ultraviolet. Of the 36 targets we found, 22 of the objects have multiple observations. Using the equivalent widths, velocities and FWHM we provided in Table 5.3, we examined a time series of each along with the corresponding fluxes for each observation from Table 5.2. Along with the times series, we examined the spectra for each object in chronological order to see visually how the absorption features changed. While most objects showed no real trends between EW, FWHM, or velocity vs. continuum flux, we found 8 cases that do.

Mrk 79 is one case of a likely variation. In Figure 5.7 Lyβ is only clearly visible in the first observation. Component 1 of O VIb is a broad feature due to blending with ISM lines. O VIr is a narrow, most likely saturated line. The variability for Mrk 79 is seen in the O VIr line. O VIr changes in EW for component 1, but does not appear to be correlated with continuum luminosity in Figure 5.8.

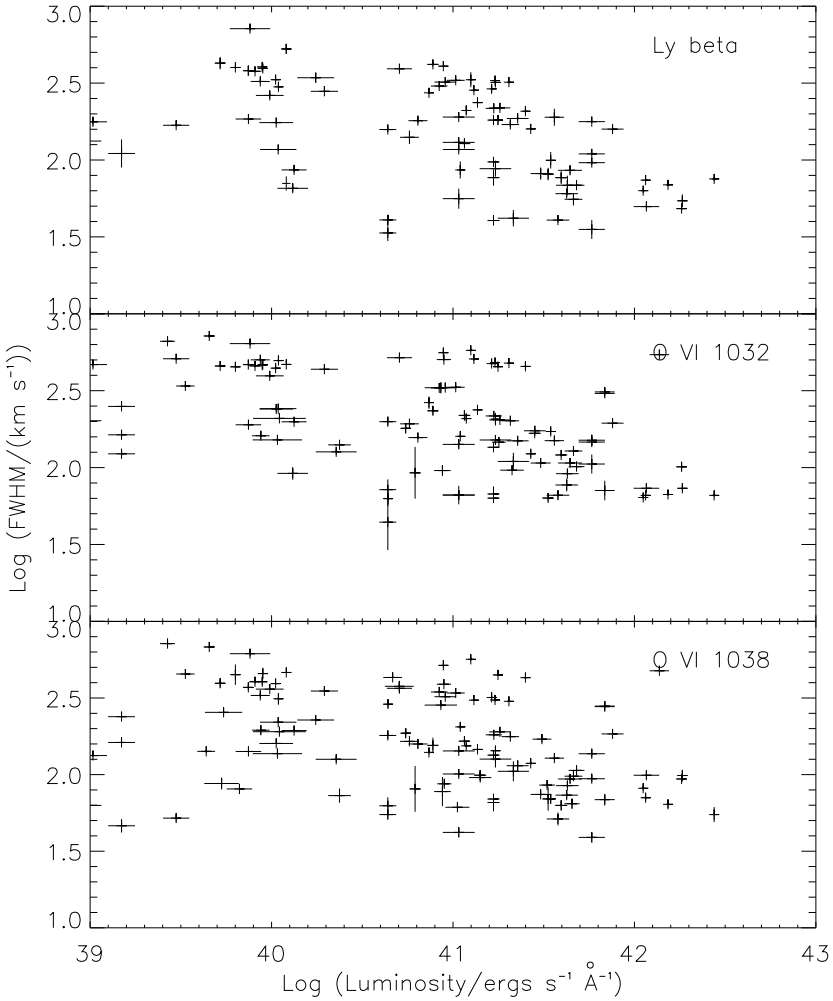

Figure. 5.6: FWHM vs.specific luminosity. The bottom plot is for O VI λ1038, the middle is for O VI λ1032 and the top plot is for Ly β.

NGC 4151 has broad, saturated absorption troughs. These troughs are comprised of several blended components seen as individual features in STIS data (Kraemer et al. 2001). Because the components are blended; it makes measuring individual EWs, FWHMs and velocities difficult. One interesting point is that in the first

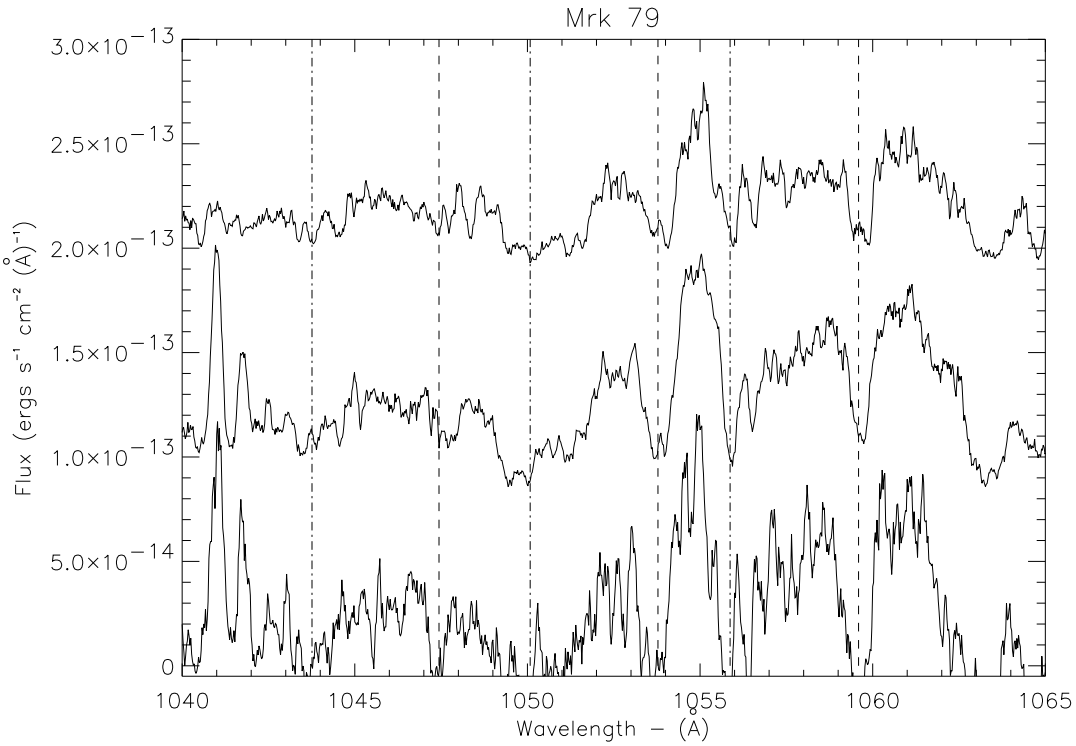

Figure. 5.7: The available spectra for Mrk 79 plotted in order of increasing time from bottom to top. The upper spectra are offset by: 6.0×10^{-14} & 1.2×10^{-13} ergs s^{-1} cm^{-2} Å^{-1}. Component 1 is labeled by a dashed line and component 2 by a dotted and dashed line in each of the three lines (Lyβ, O VIb and O VIr in order of increasing wavelength).

two observations, seen in Figure 5.9, the broad trough shows some structure, but in the subsequent observations, they blend too much to discern any one particular absorber. As shown in Kraemer et al. (2001), one particular component, labeled D′, only appears in weak flux states. In Table 2 we see that the earlier observations are weaker in flux, and that the D′ component flattens the region between ∼1029 and 1032 Å, which is consistent with the interpretation of Kraemer et al.

Mrk 817 is another object that shows evidence of variability. In Figure 5.10, we see that Mrk 817 shows in O VIb that component 1 evolves from 2 subcomponents

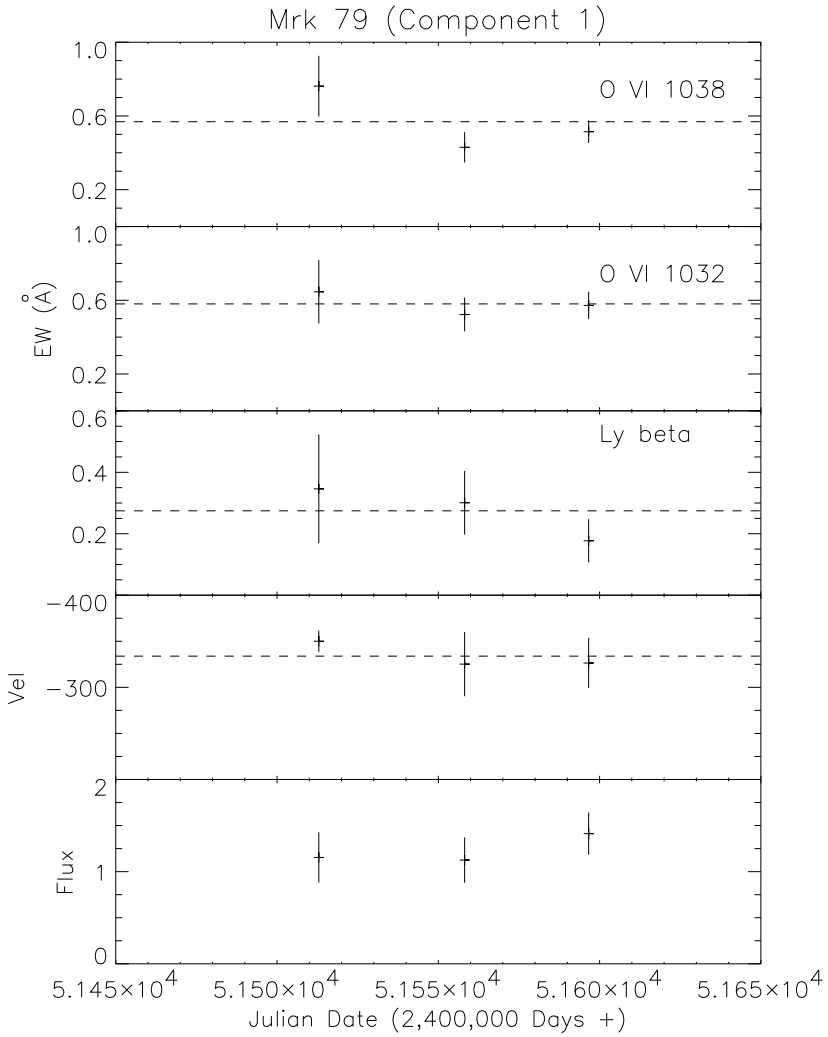

Figure. 5.8: This plot shows the relation for each of the three lines between EW, average velocity & flux over time. Top to bottom the lines are plotted in order of decreasing wavelength. The dashed line represents the average value line of the data, which is mostly to guide the eye. The continuum seems to increase slightly while O VI 1038 seems to vary by $2\sigma$and Lyβ shows some possible change.

to a smoother single component. It is possible that these subcomponents are hidden within the artificially broadened O VIr line due to galactic Fe II λ 1055. Lyman β is not visible most likely due to high ionization. This is confirmed by STIS spectra

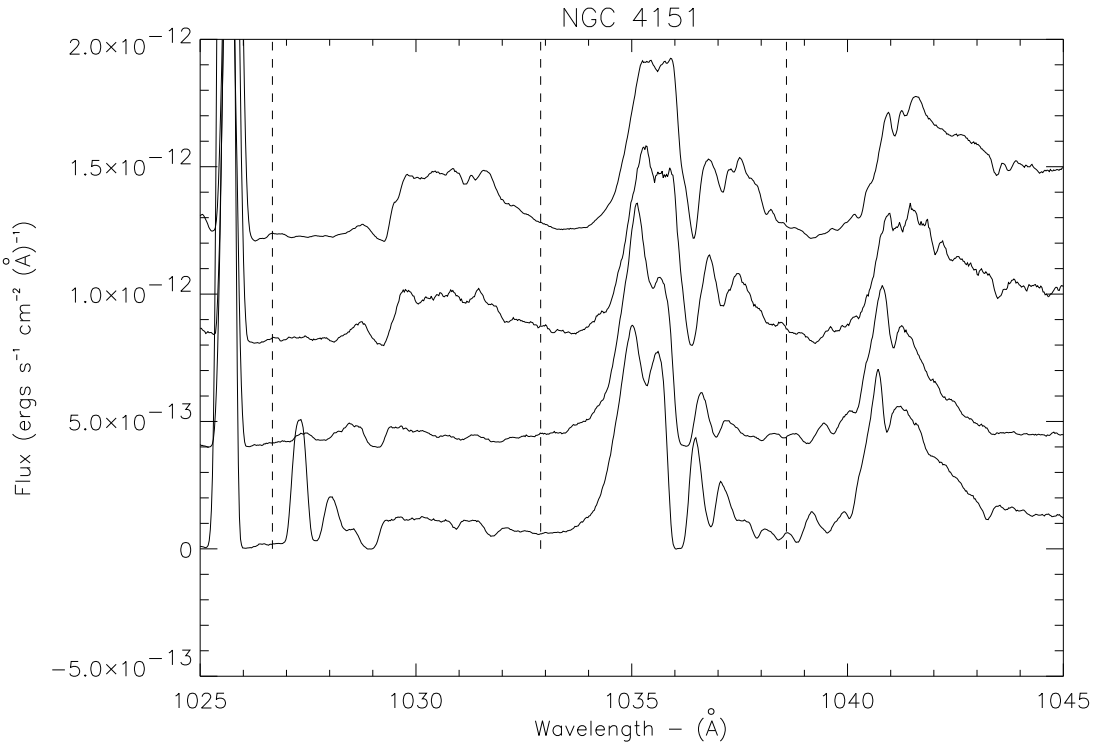

Figure. 5.9: Plotted in chronological order from bottom to top. The earlier spectra for NGC 4151 show the flattening of the region between 1029 and 1032 Åby an additional absorption component. The offsets for these data are: 4.0×10^{-13}, 8.0×10^{-13} & 1.2×10^{-12} ergs s^{-1} cm^{-2} Å^{-1}.

that show weak absorption in Lyman α (Penton et al. 2002). The equivalent widths for the lines show correlations with decreasing continuum flux (Figure 5.11), and the FWHMs show the same. The velocity seems to drop for Mrk 817, showing a significant decrease between the first observation and the last. All of this suggests two blended sub-components in the original observation, and that the higher velocity sub-component decreased with time.

Mrk 817 also demonstrates the appearance of a previously unseen line. At $\sim$ 1052 Å and $\sim$ 1058 Å we see that in the first spectrum there is no significant sign of an

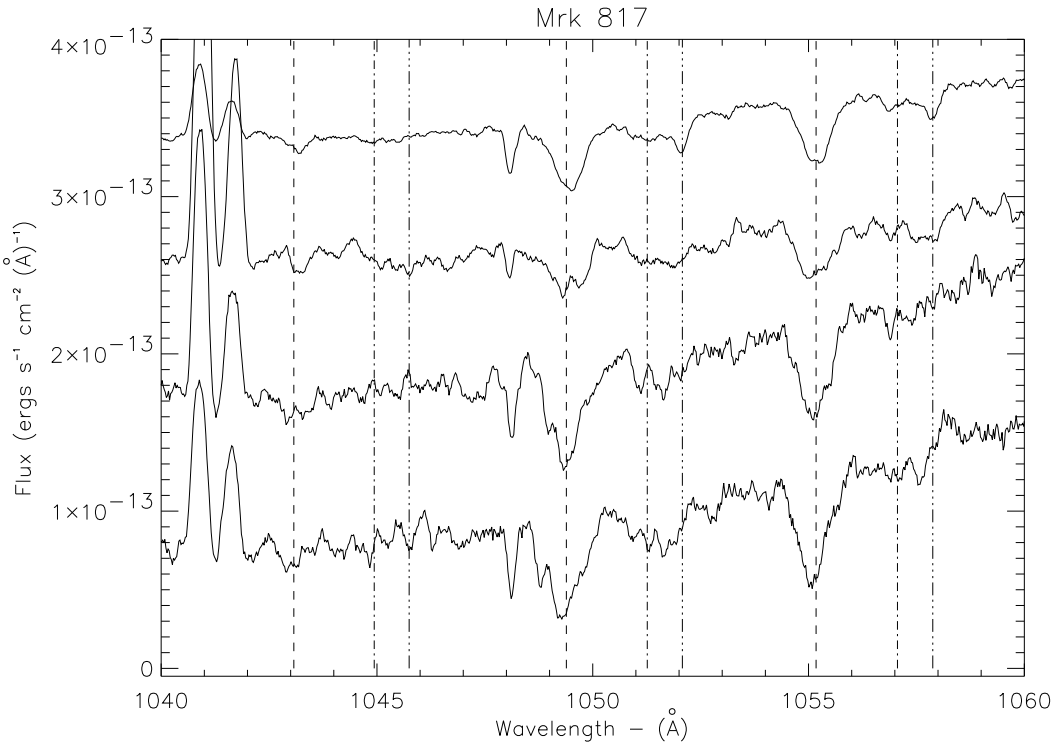

Figure. 5.10: These spectra show the changes seen in Mrk 817. We see variability in the O VIb line (component 1, dashed line), and find absorption appearing between 1051 and 1052 Å and 1056 and 1057 Å(components 2 and 3).

absorption feature. In the third spectrum there appears to be a slightly depressed broad feature, and in the final spectrum the broad line is clear with two O VI features on either side at the appropriate locations in velocity space v_r=3700 & 3430 km s^{-1}. However, we cannot rule out the possibility that the new component is present in the previous observations but not detectable due to the lower S/N.

In Figure 5.12, we present the available spectra for Mrk 279. Figure 5.13 shows the relation of EW and continuum flux for Mrk 279, which shows a weak trend. In both O VI lines the equivalent width increases with decreasing flux. For Lyβ the relationship with flux is much flatter. During the last three observations we see the

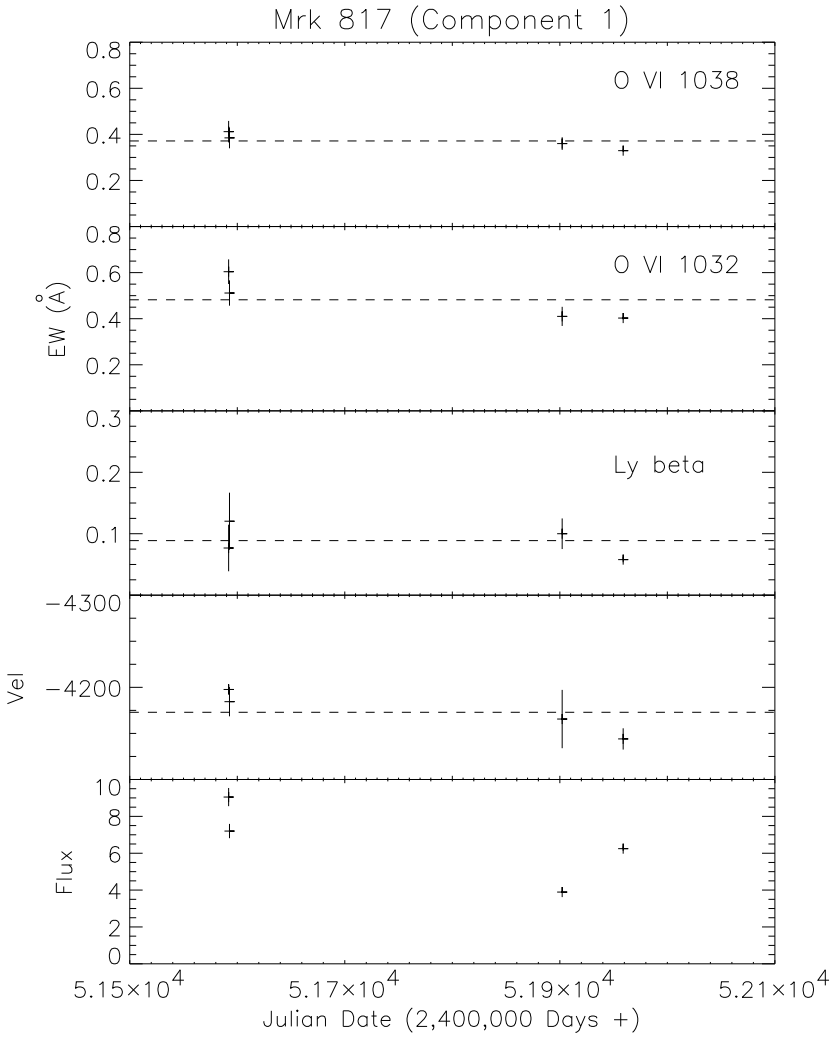

Figure. 5.11: Mrk 817 relationships of EW, velocity and flux for component 1over time. Both O VI lines show indications of decreasing EW with decreasing flux.

flux drop by ∼60% and then increase by ∼50%, while the EW for all three lines shows a chronological decrease.

Mrk 290 (Figure 5.14) provides a case for a weak anticorrelation between EW and flux. In this object the EWs for both members of the O VI $\lambda\lambda$1032, 1038 doublet

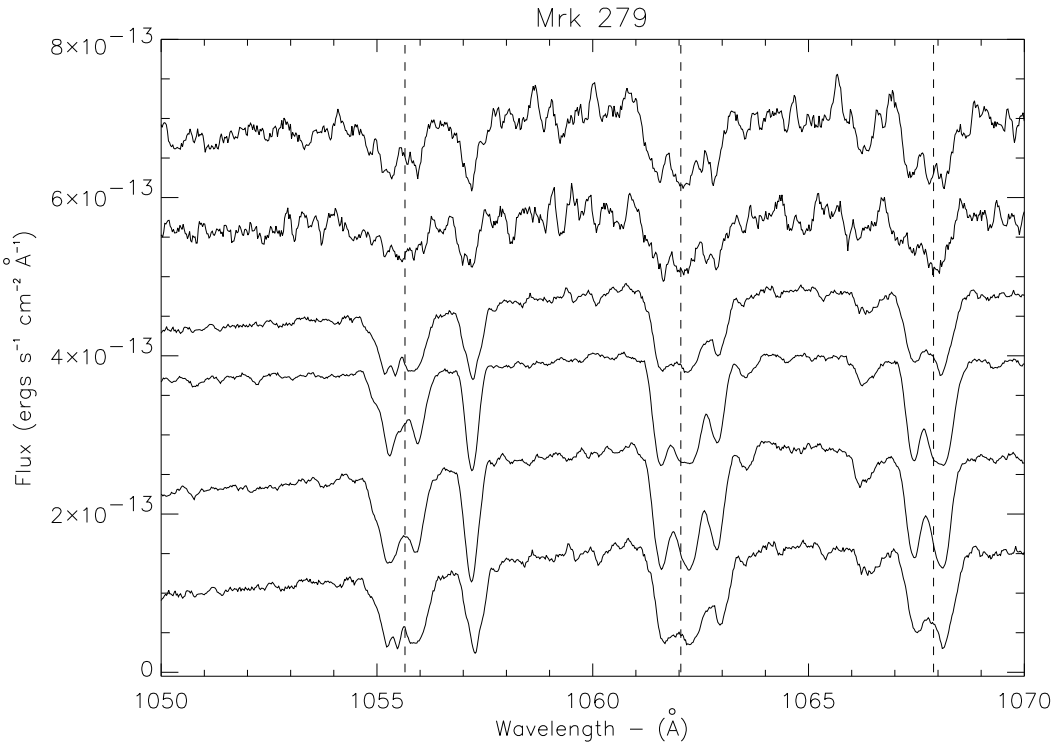

Figure. 5.12: We present the spectral time series for Mrk 279 with offsets in flux of: 1.0, 2.5, 3.5, 5.0 & 6.0 $\times 10^{-13}$ ergs s^{-1} cm^{-2} Å^{-1}. This shows the variability seen in the lines.

show a slight decrease with a significant increase in continuum flux over a 1200 day interval, and a moderate decrease in Ly β width, shown in Figure 5.15.

The variability in Mrk 509 was complex, as shown in Figure 5.16. What we measured for component 1 can be seen in Lyman β to be two at least subcomponents in two of our three spectra. What we call component 2 can be seen in Lyman β to be comprised of at least 2 or 3 subcomponents. Kraemer et al. (2003) confirms this by identifying 8 components in spectra from FOS and STIS, which are blended together into the two main components we see in the *FUSE* data. The components labeled 1-3 by Kraemer et al. are subcomponents that are contained in our measured component

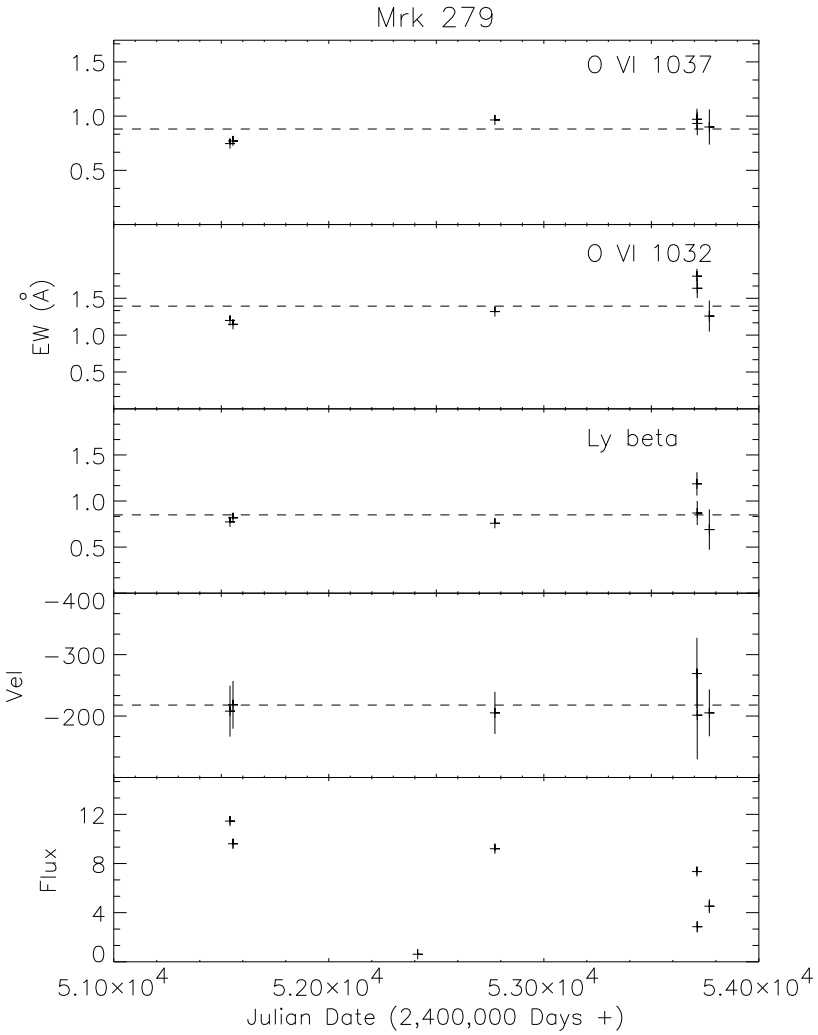

Figure. 5.13: Flux, EW and velocity against time for Mrk 279, similar to Figure 8. These quantities exhibit definite variability with time, and appears to be slightly anticorrelated with the flux. The last three points show signs of decrease in all three lines with the drop and rise of flux for those three observations, which hints at a lag in response time.

1, while those labeled 4-8 by Kraemer et al. make up our measured component 2. Subcomponents 3 and 6, as labeled by Kraemer et al., appear to vary. Subcomponent 3 shows an decrease in depth, while subcomponent 6 increases in depth over time.

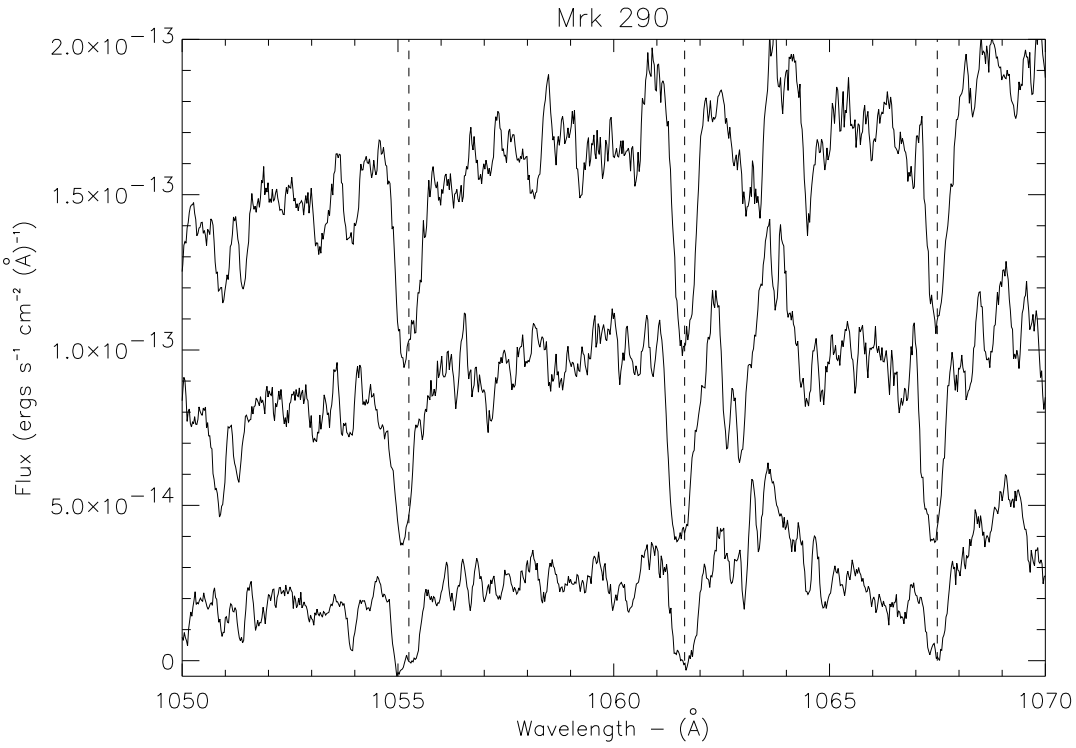

Figure. 5.14: These are spectra of Mrk 290, which show the line trends with time (bottom to top). The offsets for these spectra are: 3.0×10^{-14} & 9.0×10^{-14} ergs s^{-1} cm^{-2} $Å^{-1}$.

Our measured component 1 shows no change in EW or velocity over time (Figure 5.17), but our measured EW of component 2 shows a slight (2 σ) increase in Lyβ (Figure 5.18).

Figure 5.19 shows the spectra of PG 0804+761, which exhibits evidence of radial velocity change. This change is seen in all three lines as a centroid shift to more negative velocities, while the ISM lines remain stationary. We plot these centroid velocities vs. time (Figure 5.20). PG 0804+761 has a poorly estimated redshift, similar to IRAS F22456-5125. Thus the absolute values of velocity reflect redshifted lines, but they might change if a more accurate systematic redshift is obtained.

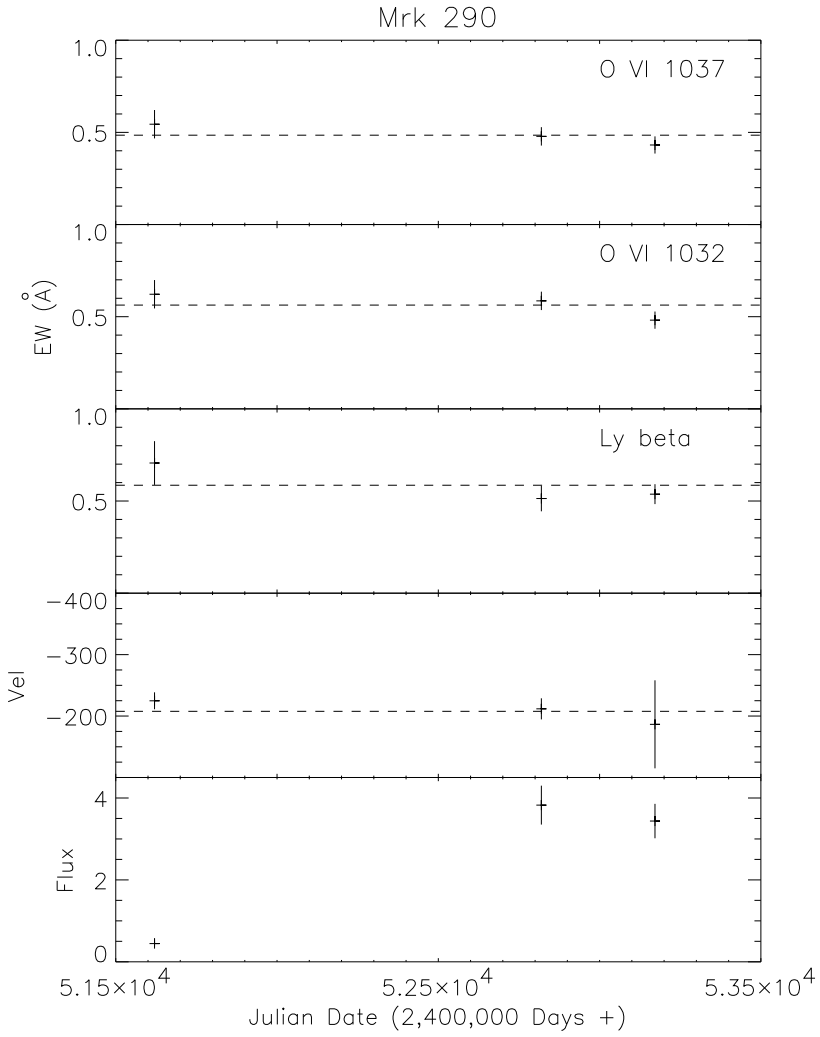

Figure. 5.15: We see in these plots (similar to Figure 5.8), that there is an decrease of EW with an increase in flux for all three lines. The trend for Lyman β is less convincing, however, due to the larger error bars.

In the object NGC 3783, we find variability of EW in the Ly β line. Figure 5.21 shows the time evolution of the spectrum, and Figure 5.22 shows the relation between flux and EW and velocity over time. The EWs for O VI λ1038 and O VI λ1032 show no correlation, across the dashed average EW line. Lyβ decreases from low flux

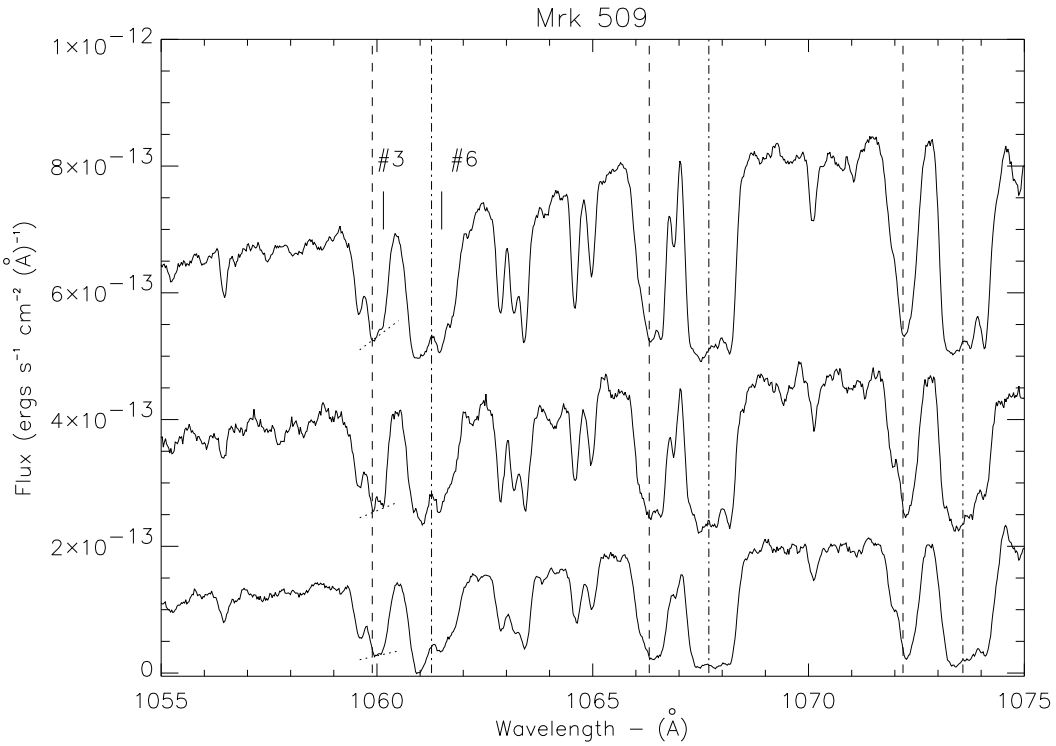

Figure. 5.16: We show the spectra for Mrk 509 and overplot the components 3 and 6 found by Kraemer et al. (2005), along with the dashed-dotted and dashed lines indicating our measured components 2 and 1 respectively. We have placed dotted lines to show the change in the slope of component 3 with respect to component 2. The offsets for these are: 2.5 & 5.0 $\times 10^{-13}$ ergs s^{-1} cm^{-2} Å^{-1}.

to high flux. However, this is evidently a blended combination of two components labeled 2 and 3 in a paper by Gabel et al. (2003). Thus it is difficult to determine if one or both lines are responding to continuum change. In Figure 5.21, we see that components 1 and 4 from Gabel et al. (2003) are visible in Ly β, and are hard to discern in O VI λ 1032 due to heavy contamination from C II and H_2. For O VI λ 1038 there are two H_2 lines nearby, but the weak component 4 is not visible.

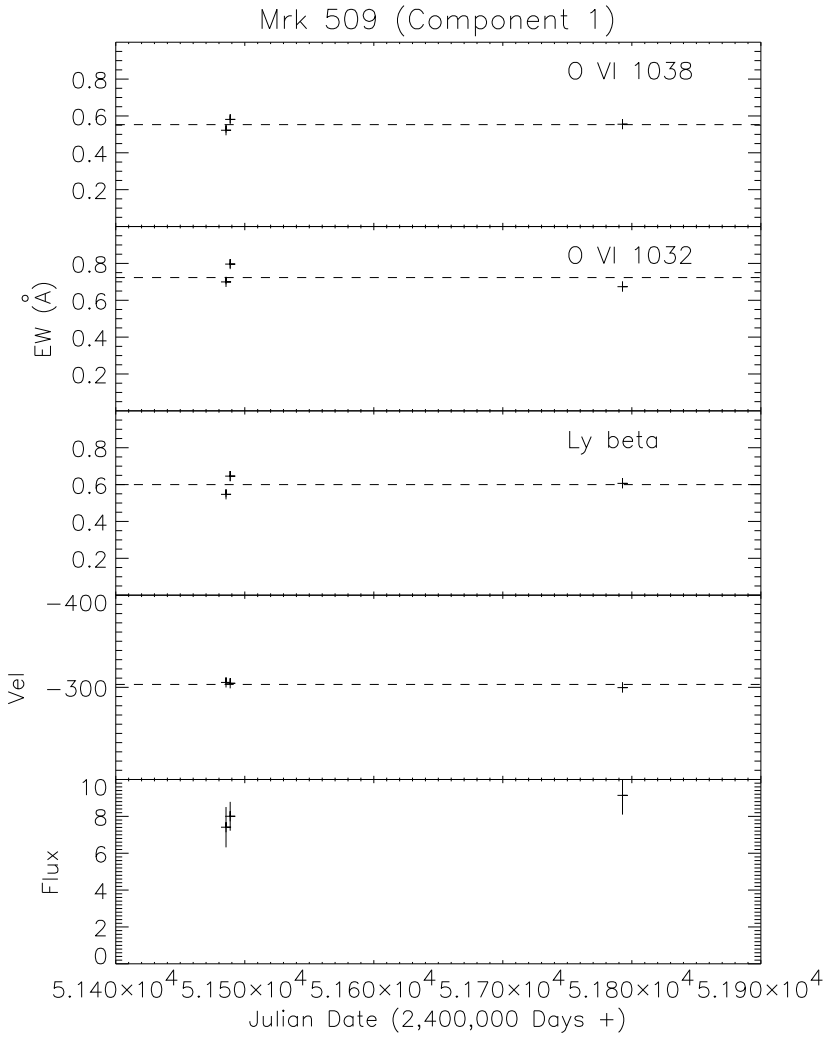

Figure. 5.17: Mrk 509 relations for component 1, plotted similar to Figure 5.8.

5.5 Discussion

In the Kraemer et al. (2005, 2006) studies of the variability in NGC 4151, they found some cases where the EWs of lines were anticorrelated with the continuum flux level, while others showed no relation to the flux. We see similar events in only a few

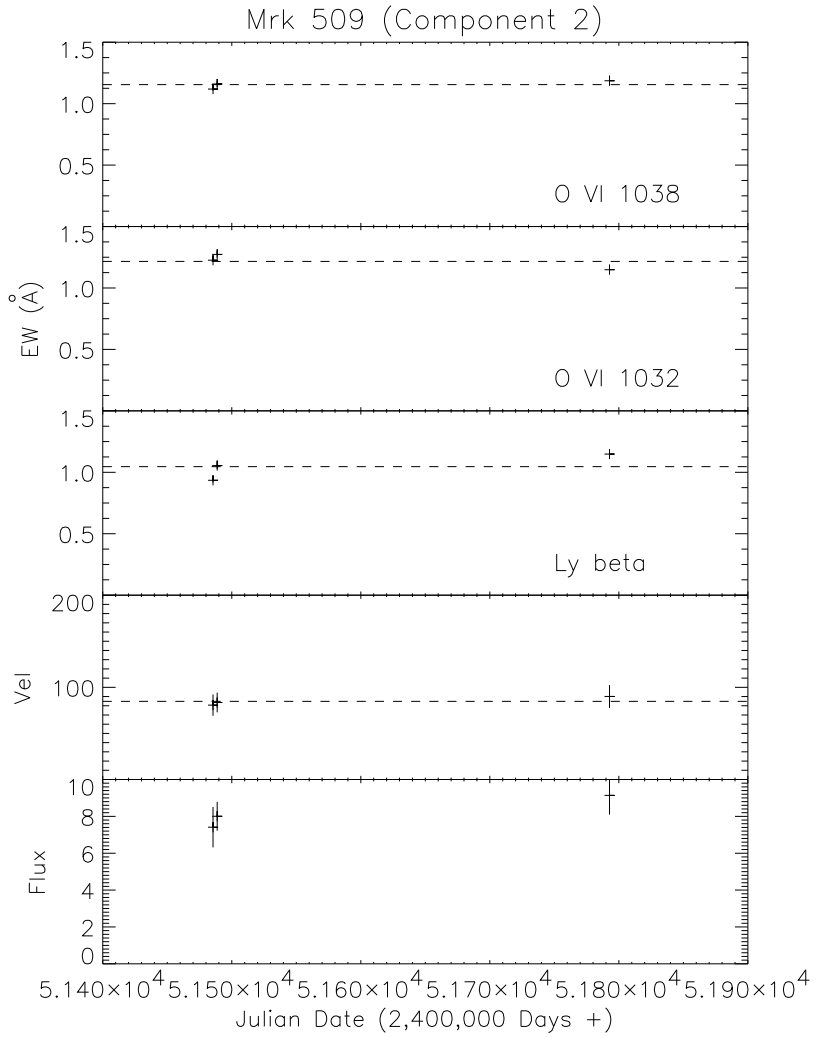

Figure. 5.18: Mrk 509 relations for component 2, plotted similarly to Figure 5.8.

objects like Mrk 817, where the O VI lines seem to follow the continuum, and Mrk 79, where the EWs vary but the continuum stays relatively constant. The paucity of O VI variability suggests that O VI, which is usually predicted to be very strong in absorber models, is saturated in most cases. The changes we do see in EW must be due to one of three events: a change in ionization, a covering factor change in the line

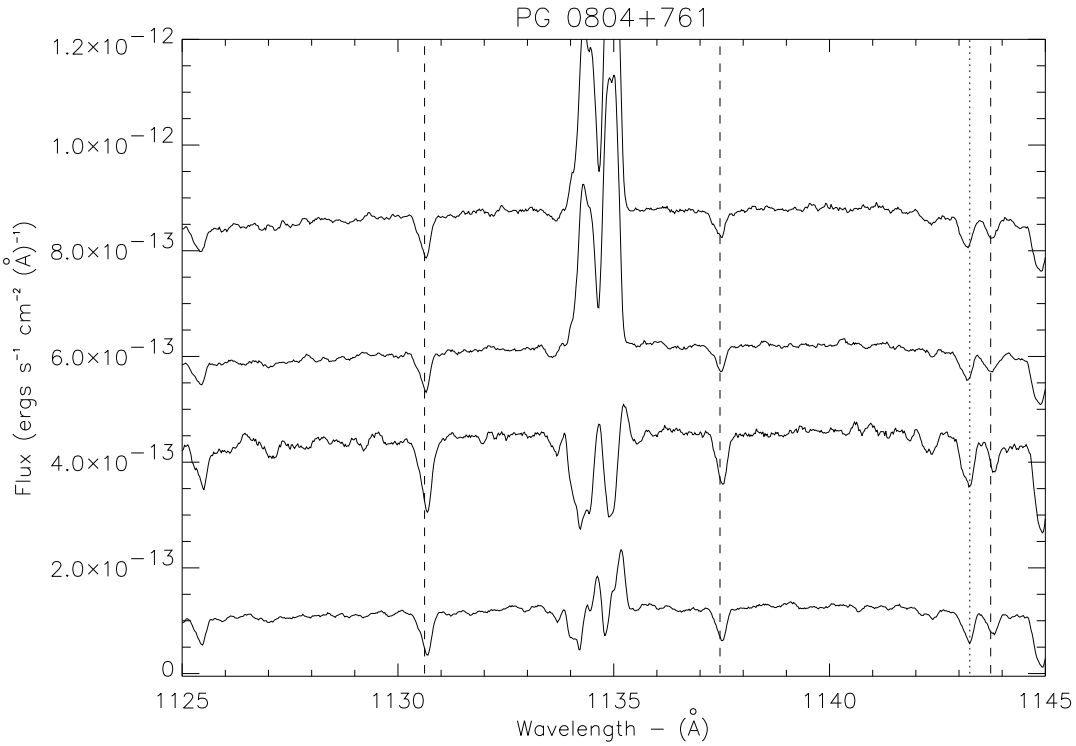

Figure. 5.19: Spectra for PG 0804+761. The lines are marked with the dashed average velocity line, and the lines clearly appear to move. The dotted line labels a galactic Fe II line λ1044.2 to show that the centroid for the ISM lines are not moving. Offsets for these are: 2.5, 5.0, 7.5 $\times 10^{-13}$ ergs s^{-1} cm^{-2} Å^{-1}.

of sight, or a total column change (characterized by N_H).The latter two could be due, for example, to bulk motion of gas across our line of sight. To summarize, we found 8 AGN with clear evidence for EW variations in at least one absorption component, and one of these AGN (PG 0804+761) shows evidence for radial velocity variations.

5.5.1 Potential Cases of Bulk Motion

There are three targets in our survey that the best canidates for bulk motion of gas across the line of sight with a transverse velocity (v_t), as described below. These three objects are Mrk 79, Mrk 817 and Mrk 509.

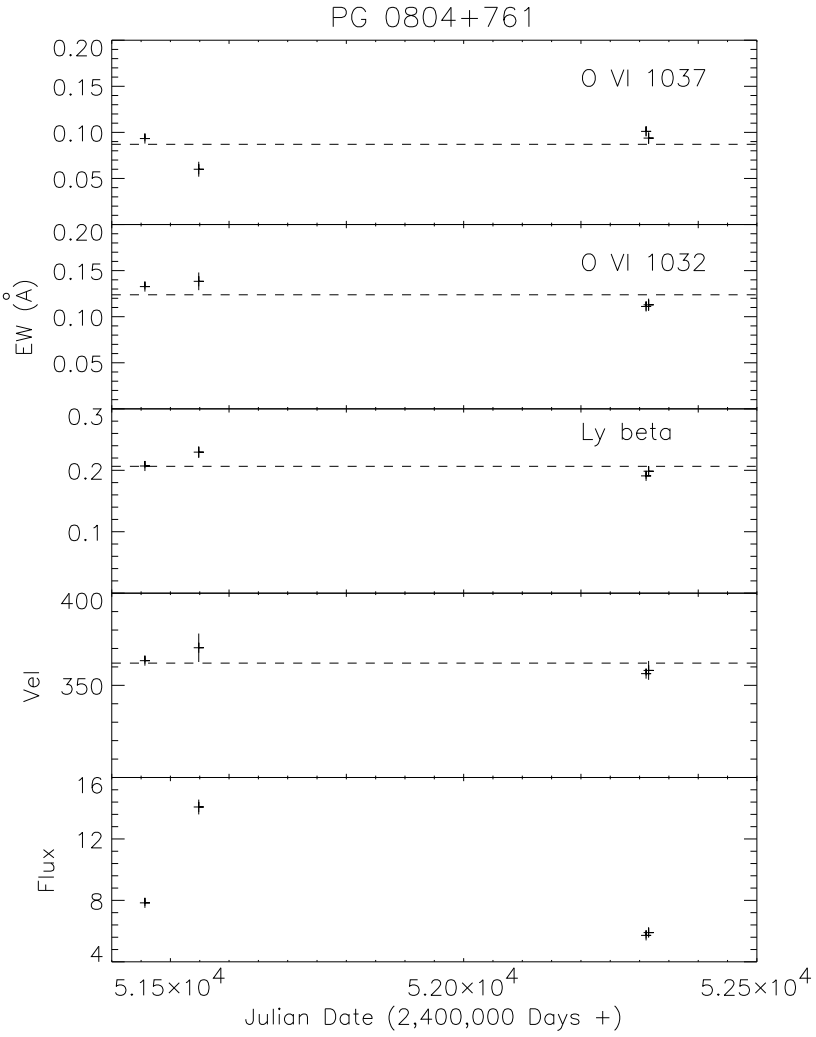

Figure. 5.20: PG 0804+761 relationships similar to Figure 5.8. We see definite correlations between velocity and EW with the flux levels with the exception of the Lyβ EW which seems to be low in the second observation.

Mrk 79 is an unique target because while the EW of component 1 is variable, the continuum does not change. By examining the line depth we see that there is no evidence for a covering factor change, so this lends itself to a case of changing total column, most likely due to bulk motion. We can calculate the transverse velocity

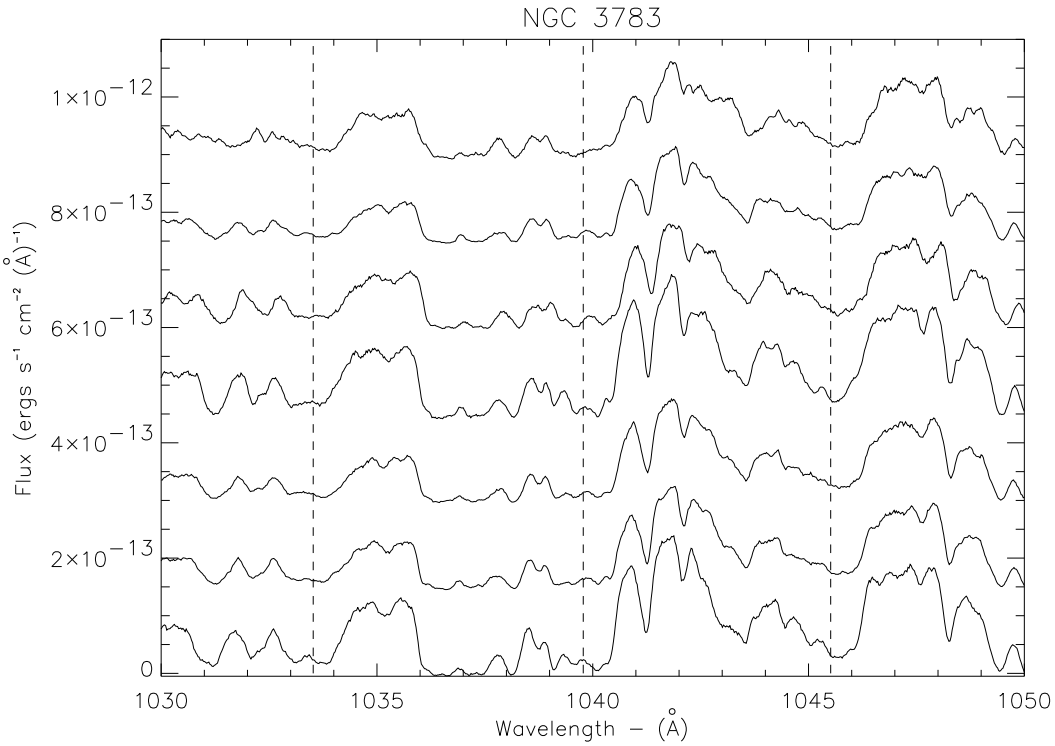

Figure. 5.21: Spectra showing the time evolution of NGC 3783. The measured component is labeled with the dashed line. Offsets for these are: 1.5, 3.0, 4.5, 6.0, 7.5 & 9.0 $\times 10^{-13}$ ergs s^{-1} cm^{-2} Å^{-1}.

by using the measured broad line diameter from Peterson et al. (1998) of 36 light-days and a time interval between observations (Δt) of 83.7 days. This would imply the absorber would be moving at a transverse velocity $\geq$126,000 km s^{-1}. Given the average radial velocity of the absorber v$_r \approx$300 km s^{-1}, the estimate for the transverse velocity is inordinately high. We will tackle further explanations in the next section.

In the case of Mrk 817, the appearance of the new absorption components (2 and 3) suggests transverse motion of material into the line of sight, and we can follow the methods used by Gabel et al. (2005) for NGC 3783. Assuming the O VI is saturated we can find the covering factor in the line of sight for O VI at the conclusion of the

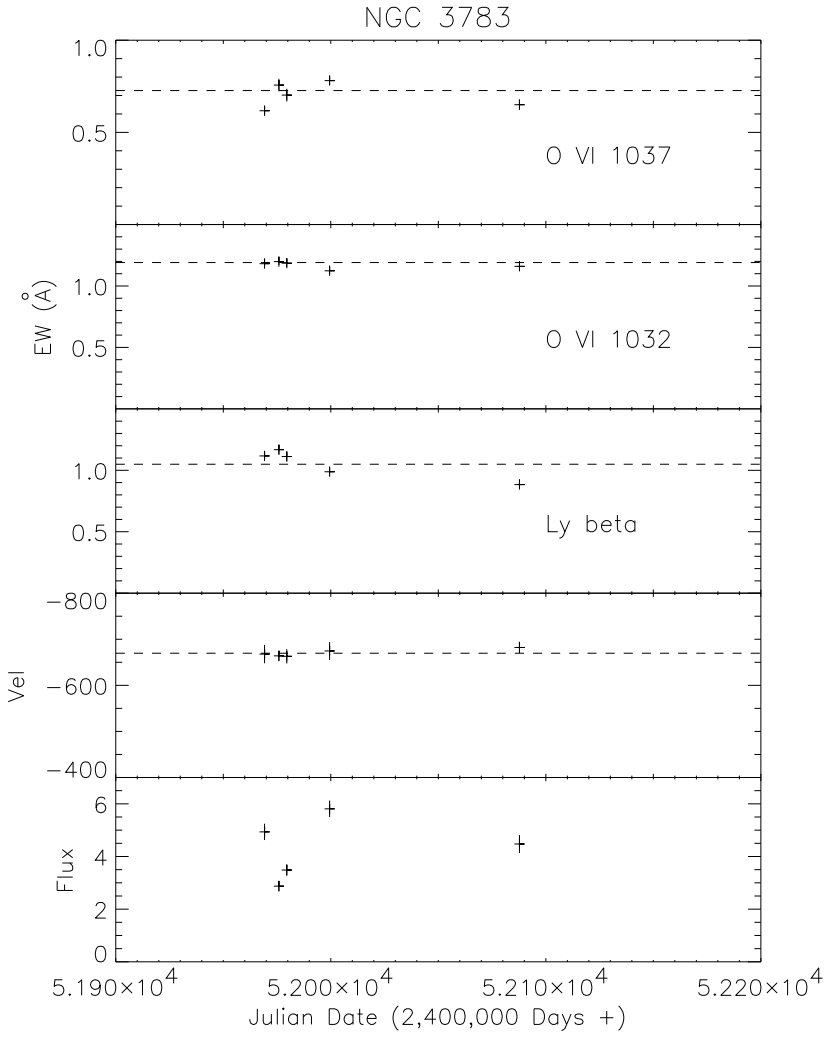

Figure. 5.22: This shows the relation for NGC 3783 between EW, velocity and flux over time, similarly to Figure 5.88. We see definite variability in the EW over time for all three lines. There appears to be a possible correlation between the change in Lyβ EW and continuum flux.

variability event with the equation (Crenshaw et al. 2003):

$$C_f = \frac{I_1^2 - 2I_1 + 1}{I_2 - 2I_1 + 1}, \tag{5.2}$$

where I_1 is the intensity at the core of the stronger oscillator strength line and I_2 is

for the weaker line. This number can be skewed by additional flux from the Narrow Emission Line Region (NELR) (Kraemer et al. 2002; Arav et al. 2002; Crenshaw et al. 2003), but for Mrk 817 the narrow emission lines are not prominent, and we find C_f = 0.98. The transverse size of the absorbing cloud is d=$d_{BLR}\times\sqrt{C_f}$ (Crenshaw et al. 2003). For Mrk 817, the BLR is 31 light-days across (Peterson et al. 1998). The absorption appeared over ∼310 days, which gives a lower limit to the transverse velocity of ∼29,800 km s^{-1}. This is exceptionally large compared to the radial velocities of 3700 and 3430 km s^{-1} for the two new components. Thus, either the components were buried in the noise in the earlier observations or we are witnessing appearance due to ionization changes.

Mrk 509 shows evidence for an increas in the EW of Lyβ in our component 2 with increasing continuum flux, which cannot be accomplished with a change in N_H or C_f. Thus, it is a prime canidadte for transverse motion.

Mrk 509 was shown in Peterson et al. (1998) to have a BLR size of 159 light-days. If we assume that subcomponents 3 and 6 are saturated in Lyβ, then we can calculate the change in covering factor (C_f) from the residual intensities in the cores (C_f = 1-I_r). In the case of subcomponent 6, we measured the core and found average covering factors C_f=0.78 and 0.96 for observations 1 and 3 (Δt=307.3 days). For subcomponent 3, we find covering factors C_f=0.93 and 0.77 for observations 2 and 3 (Δt=304.0 days). Subcomponent 6 therefore, showed an increase in covering factor by 0.18 while subcomponent 3 showed a decrease by 0.16. Based on the changes in

covering factors, from our previous distance equation we can find lower limits for the transverse velocities of 65,600 km s^{-1} for subcomponent 6 and 125,200 km s^{-1} for subcomponent 3. This seems extremely high for a transverse velocity when compared to the radial velocities of $\sim$300 km s^{-1}. Therefore, the changes in the depths of these two subcomponents are almost certainly due to ionic column variation and not covering factor changes.

Thus, even in the most favorable cases, we find no evidence for EW changes due to bulk motion. Because there is no evidence that transverse velocities of UV absorbers can reach these inordinately high values (Crenshaw et al. 2003), the only viable alternative is ionic column changes due to changes in the ionizing continuum.

5.5.2 Ionization Changes

The three objects for which we have ruled out bulk motion and the other six objects that showed signs of absorption variability all seem to show these as the result of changes in ionizing flux. Mrk 279 and Mrk 290 showed an anticorrelation between ionization parameter (U) and O VI EW, while NGC 3783 showed anticorrelation in Lyβ. For Mrk 279 and Mrk 290, this means that the ionization state is high, and NGC 3783 is indeterminate due to no detectable change in O VI. Mrk 817, component 1, is the only case where the EW for O VI is correlated with the flux, which means that U is relatively low. For NGC 4151 we see the D$'$ component decrease with increasing flux, thus it is another high U component. PG 0804+764 showed correlation between flux and EW for both the O VIb line and Lyβ. This object stands out because it is

the only object in the survey that showed an unexplainable change in radial velocity.

Mrk 79 showed a change in EW and no change in flux. Because we only have three observations, we believe that we are seeing a change in ionization with a time delay. Our observations do not accurately sample the lightcurve and there must be a delay between the EW response and the continuum, due to low densities and/or large distances of the absorbers from the continuum source (Crenshaw et al. 2003).

The appearance of the absorption components 2 and 3 in Mrk 817 is most likely due to a change in ionization. The light curve shown at the bottom of Fig. 5.11, shows that in the last observation where the two components are visible, the flux level had decreased significantly. The appearance of these lines may therefore be due to a decrease in ionizing flux. We can also use the possible disappearing subcomponent in component 1 to place limitations on the absorption systems. As the continuum flux decreases, the line weakens and vanishes/blends with the component at ∼1049.2 Å, and could be the explanation of the EW variations we noted in §5.4. In order to place these constraints, we need photoionization modeling of the absorbers.

Mrk 279 presents a similar situation. In Figure 5.13 we have a range of ∼58 days where the continuum flux drops and rises. The EW for the absorbers respond by decreasing. We could estimate a lower limit to the distance and density provided a model of the absorber and assuming the response is complete after 58 days. Ideally, we would need a monitoring campaign with several observations for an event such as this to fully explain the variations.

For the component Kraemer et al. (2002) labeled 3 in Mrk 509, we can assume that the ionizing flux increased and the column changed. We know from Kraemer et al. (2003) that the ionization parameter (U) for Mrk 509 in component 3 is 0.03. Kraemer et al. provide the ratio of neutral hydrogen to ionized hydrogen. Given the change in time, Δt = 2.6$\times$10^7 s, we can use the equation as seen in Krolik & Kriss (1995) and Bottorff et al. (2000):

$$t(X_i) = \left[\alpha(X_i) n_e \left(\frac{f(X_{i+1})}{f(X_i)} - \frac{\alpha(X_{i-1})}{\alpha(X_i)}\right)\right]^{-1}, \tag{5.3}$$

where α(X$_i$) is the recombination coefficient for the ion X$_i$ and f(X$_i$) is the fraction of the element in ionization state i, in our case Hydrogen Lyman β. From Kraemer et al. (2003) the ratio of H^0 to H$^+$ is $\sim$4.0$\times$10^{-4} for component 3, and we know α(X$_i$) for hydrogen is 2.5$\times$10^{-13}s (Osterbrock 1989). The recombination time is then 2.6$\times$10^7 s which gives a density n$_e$ = 3.8$\times$10^8 cm^{-3} for component 3.

Finally, we can estimate the distance of the absorbing cloud assuming a change in ionization, from the ionization parameter:

$$U = \frac{\int \frac{L_\nu d\nu}{h\nu}}{4\pi c r^2 n_e} \tag{5.4}$$

For our two components we find the distance from the source to be 0.3 pc for component 3.

5.5.3 NALs and BALs

From both our survey and the Laor & Brandt surveys, one object, PG 1411+442, appeared in both surveys with BAL and NAL signatures. The NALs appear superimposed on the BAL in both members of the O VI doublet. This evidence tied with the Laor & Brandt and our relationship from §5.3, shows that both BALs and NALs are related and follow the same trends and that they both may exist simultaneously in an object.

Also from our previous survey, WPVS 007 was omitted from the search for NALs due to the discovery of a newly appearing BAL by Leighly et al. (2007, in prep). We have reexamined this object and found that the NALs seen by Crenshaw et al. (1999) are still visible in the *FUSE* spectrum. The NALs for O VI and Ly β are buried in the BAL and have a velocity of -399 ± 10 km s^{-1}, as seen in Figure 5.23. This matches the velocity Crenshaw et al. (1999) found of -390 km s^{-1}.

We can evaluate the configuration of the NAL and the appearing BAL in WPVS 007. The time difference between the *FUSE* spectrum and the last FOS spectrum is 2655 days. If we use the relationship from Vestergaard & Peterson (2006):

$$R \propto L_\nu(5100\mathring{A})^{0.50\pm0.06}, \tag{5.5}$$

with a BLR size that has been estimated from reverberation mapping, we find that the BLR size for WPVS 007 is $\sim$23 light-days across. This gives a lower limit on the transverse velocity of the BAL of 2565 km s^{-1}. The NAL however is still apparent in

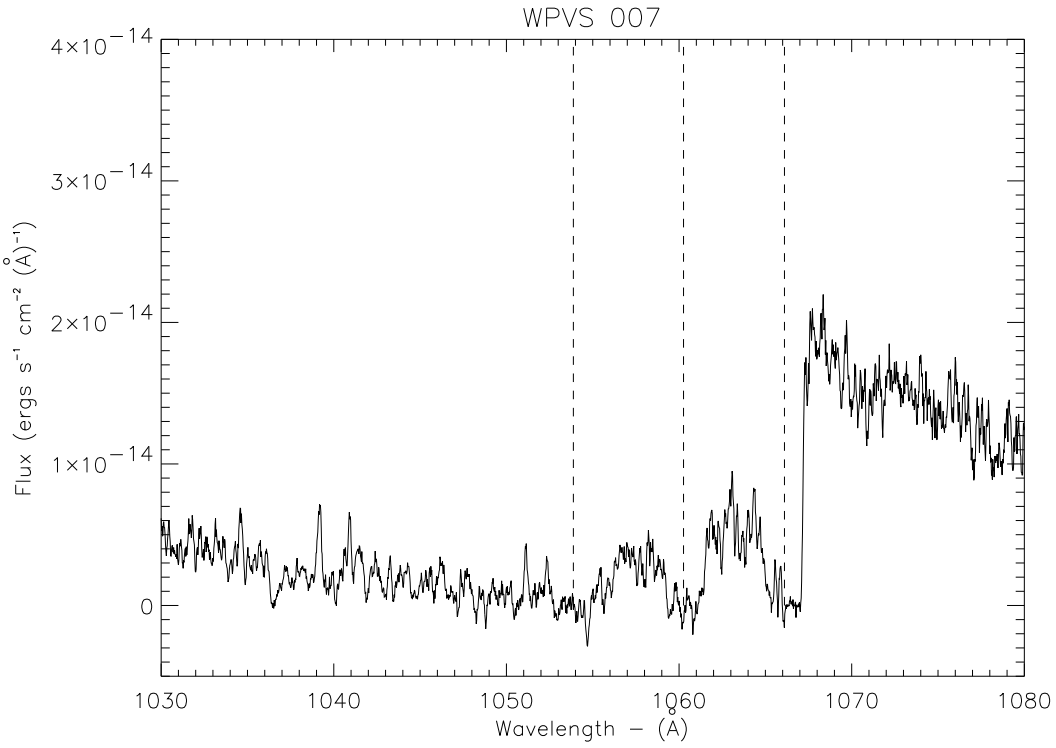

Figure. 5.23: Spectrum for WPVS 007. The three absorption features are marked with dashed lines.

the O VI doublet and Lyman β lines. This leaves us with two situations. Either the NAL is interior to the BAL and is still receiving sufficient ionizing flux to maintain the absorption, or the NAL is exterior to the BAL and is no longer receiving ionizing flux due to the BAL absorption. If the latter is true, then the recombination time-scale is larger than the 2655 days between observations, which could be used to estimate a density and distance provided photoionization modeling.

5.6 Conclusions

Our goal was to explore our *FUSE* survey (Dunn et al. 2007) in depth for correlations and variability. We sought to characterize the intrinsic absorption seen in nearly 50% of all nearby active galaxies in order to help characterize the outflow from the nuclear engine.

As shown by Laor & Brandt (2002), there is a relation between the maximum outflow velocity and the luminosity. Their survey contained moderate redshift objects and BAL quasars, while our survey was for smaller redshifts and luminosities. However, as shown previously, our relation between v_{max} and L is consistent with theirs. In both our surveys there is a distinct upper limit on maximum velocity that is dependent upon the luminosity of the object. This leads us to believe that both classical narrow intrinsic absorption lines and broad absorption lines are governed by the same relationship. Thus they may be related, in the sense that they may share a common driving mechanism.

Laor & Brandt (2002) also found for higher redshift galaxies that EW and luminosity are correlated for C IV. We examined correlations between the observed lines and the AGN properties. We found no link between the equivalent width and the luminosity. Because equivalent width increases with column density of the particular ion in question, it would seem that an increase in flux would increase the O VI EW in cases where the ionization parameter is low and vise versa for a highly ionized cloud, at least until the line reaches heavy saturation. We do not see this trend for either O

VI or Lyβ. This is most likely due to the heavy saturation in O VI and even Lyβ in many cases, while C IV and N V do not saturate as easily due to their abundances and the oscillator strengths of their UV lines.

It has been seen in the past that some objects show bulk transverse motion along with the more easily detectable radial motion (Crenshaw et al. 2003). Of the 35 objects available we have 22 with more than one observation. Two of these objects have only one usable observation, leaving 20 total useful data sets. In the survey we find 8 that show change. This frequency of variability events, in *FUSE* data (8/20), seems to be low. This could mean either the events are rare, that only weak absorption is subject to this change and/or the sample is biased by small number statistics, or the O VI saturation makes detecting variability difficult.

None of our objects with EW changes can be explained with transverse bulk motion. We have 7 that can be explained with ionization changes. In the case of Mrk 509 with modeling of the subcomponents, we can find a distance and density (n_H) of the third subcomponent of 0.3 pc and 3.8×10^8 cm^{-3} respectively. Also, we find one object that shows evidence for radial velocity changes (PG 0804+761); we currently have no explanation for this.

We find in Mrk 817 that the absorption appears in relatively weak lines, and furthermore even the changes in the absorption features for Mrk 509 are in relatively weak lines. This is the case for most transversely moving clouds seen in the past. With the low signal-to-noise *FUSE* data it may be that these weak lines are swamped by

the surrounding noise and only strong absorption features are noticeable, or it may be that bulk transverse motion is not a common event. Given that these changes are in weak absorbers, it suggests that strong absorbers appear more static in the far UV than do weak absorbers due to saturation and blending in many of the lines.

The circle is now complete. When last we met I was but the learner,
now I am the master.

—— James Earl Jones (Star Wars)

– 6 –

Physical Conditions in the UV Absorbers of IRAS F22456-5125

6.1 History of IRAS F22456-5125

IRAS F22456-5125 shows an interesting assortment of intrinsic absorption lines. It has five kinematic components spaning a velocity range of 700 km s^{-1}. Three of these five components are easily visible in Lyβ λ1025.7, C III λ977.0, Lyγ λ972.5, Lyδ λ949.7, Lyη λ937.8 and possibly N III λ989.7 and Ly 6 λ930.8, which are shown in Figures 6.1−6.3.

Currently there are several UV observations of IRAS F22456-5125. *IUE* observed this object five times and *FUSE* thrice. In the optical regime we have obtained two spectra from CTIO (§5.1), and two spectroscopic observations were taken with 2.2-m and 2.1-m telescopes at La Silla, Chile and McDonald Observatory of the University of Texas at Austin respectively (Mason et al. 1995; Grupe et al. 1998). These spectra were published later in Breeveld et al. (2001). IRAS F22456−5125 has also been studied in the X-Ray regime. There are several Advanced Satellite for Cosmology and Astrophysics (ASCA) observations, a Roentgen Satellite (ROSAT) observation and three XMM-Newton observations.

Breeveld et al. (2001) approximated the Spectral Energy Distribution (SED) from

the available observations in the X-Ray, UV and the optical. We show their SED power law fit in Figure 6.4 along with our measured continuum point for the 1020 bin averaged from Table 5.2. IRAS F22456−5125 showed two interesting features. The first was that the X-Ray observations showed evidence for an ultra-soft X-Ray excess, and the second was that the optical spectra drastically changed slopes. Their power law fits ($F_\nu \propto \nu^\alpha$ for the X-Ray were α=−1.3 and α=−0.8 for the soft (0.3−2 keV) and hard X-Ray (2−10 keV) respectively and a very high value of α=−3.1 for the ultrasoft X-Ray excess (0.1-0.3 keV). This excess, however, appears to be variable over time along with the slope in the optical regime. The optical slopes vary between α=−1.3 in the 1992 observation from Grupe et al. (1998) and α=+0.8 in the 1991 observation from Mason et al. (1995).

Based on our variability analysis we find that the absorption lines in IRAS F22456−5125 are stable over a time range of ∼450 days and a decrease in UV continuum flux by a factor of 6. We coadded all three available spectra weighted by exposure time for better signal-to-noise due to the lack of variability, and present the spectrum sections with the measurable lines in Figures 6.2−6.4. With so many lines present and a good range of ionizations, we decided this would make an excellent candidate for modeling the absorption.

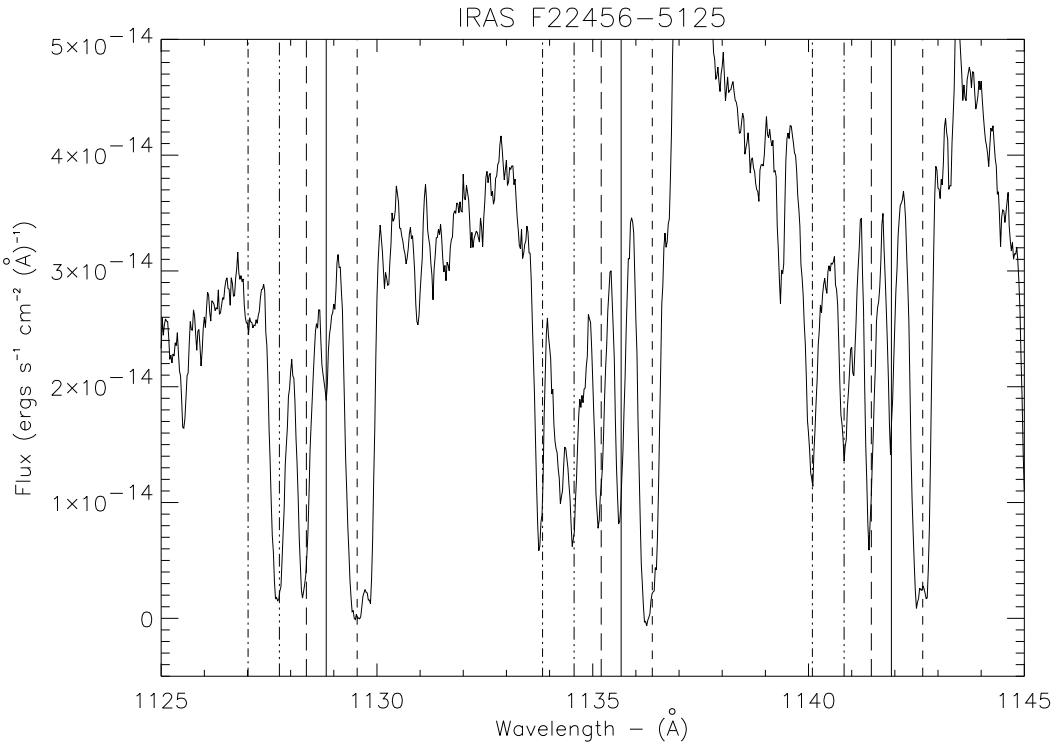

Figure. 6.1: Spectral region of Lyβ, O VIb and O VIr in order from left to right. Each of the dashed lines represents the average velocity for the 5 kinematic components averaged over the three available observations.

6.2 FUV Absorption Components

We measured the residual flux (F_r) for each of the O VI lines and Lyβ. We calculated the covering factors for the components using Eq. (5.2) for the lines in the doublet. For a saturated line, a good approximation for the covering factor should be 1-F_r. We present these data in Table 6.1. If we compare the covering factors from the O VI doublet and from Lyβ, we see that components 2, 3 and 5 are similar and thus likely to be saturated. Components 1 and 4 are the weaker components in Ly β, and not saturated based on the comparison. If we measure 1-F_r for O VIr, we see that all 5

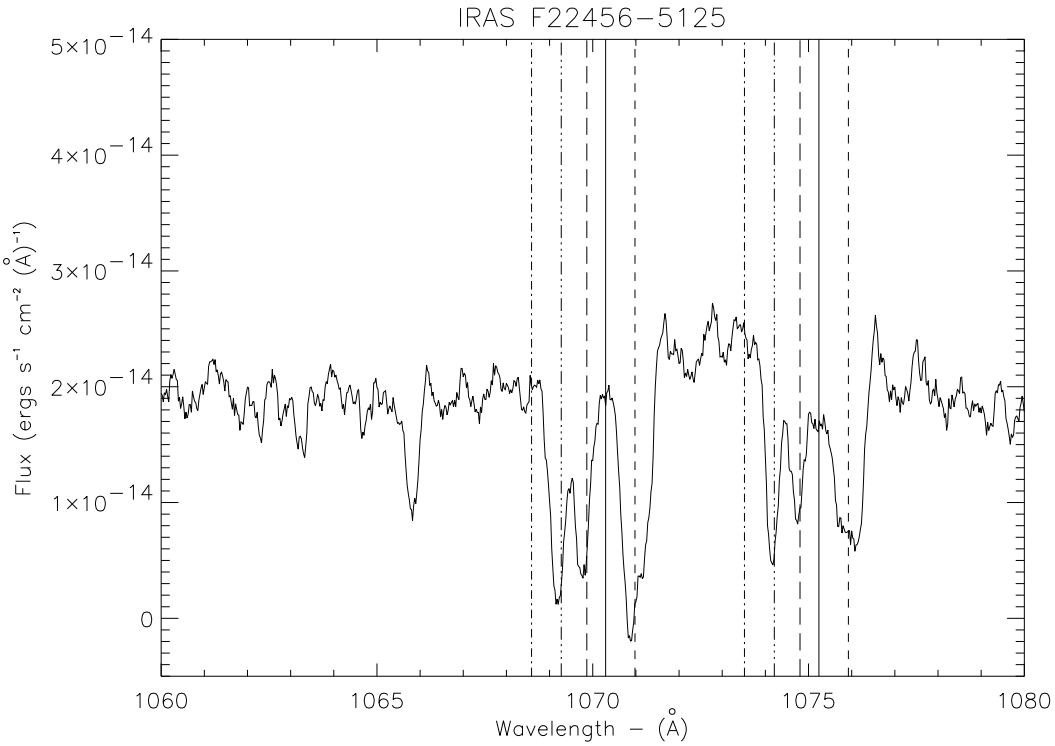

Figure. 6.2: Spectral region with Lyγ and C III right to left respectively. As in Figure 6.3, we have plotted the average velocities for each of the 5 kinematic components as vertical dashed and dotted lines.

lines are comparable and are thus saturated. We would expect the 1-F_r measurements to not exceed the values we derived from the O VI doublet. This discrepancy in the covering factors arises from geometry. These clouds are inside of the NLR and thus the narrow emission line is affecting the troughs of the lines as seen in §3.4 for NGC 3516. Thus, Eq. (5.2) does not hold for these lines as the addition is non-uniform and the columns we measure will be lower limits.

Provided with the covering factors from Table 6.1, we were able to convert from normalized flux to optical depth. Hamann et al. (1997) shows that the optical depth

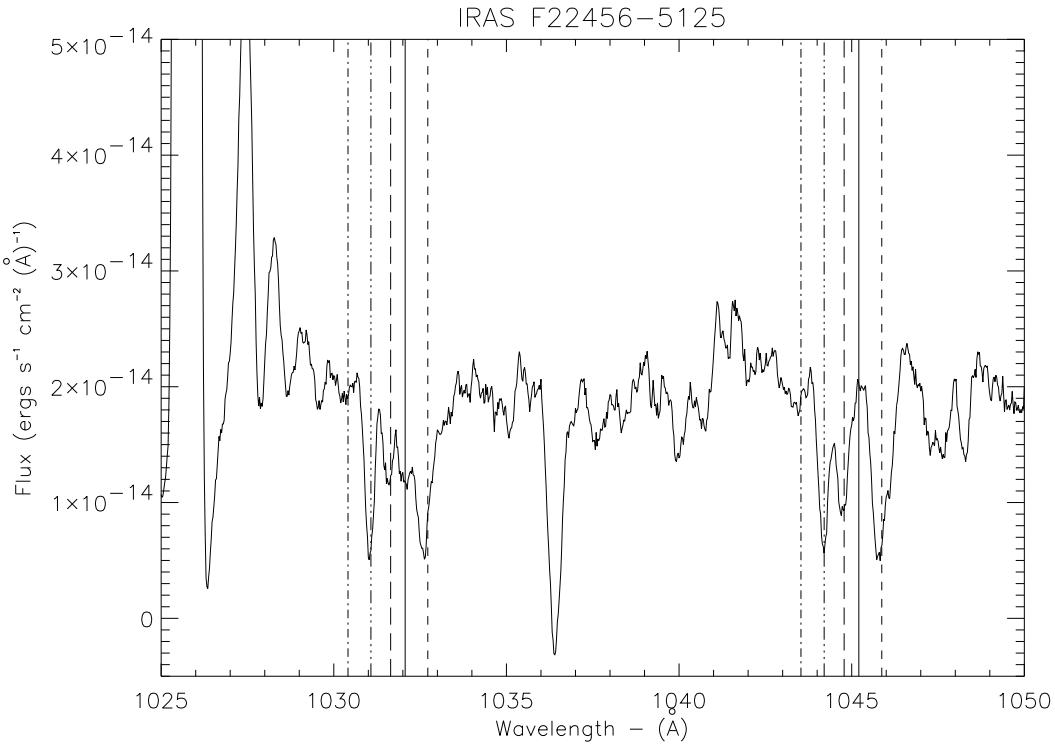

Figure. 6.3: Spectral region with Lyδ and Lyη right to left respectively. As before, we plot the average velocities for the 5 kinematic components as vertical dashed and dotted lines.

for a line from an absorber that does not completely cover the source is given by:

$$\tau = ln\frac{C_f}{I_r + C_f - 1}, \tag{6.1}$$

where τ is evaluated at each radial velocity (v_r). This equation combined with

$$N = \left(\frac{m_e c}{\pi e^2 f \lambda}\right) \int \tau(v_r) dv_r, \tag{6.2}$$

(Savage & Sembach 1991), where f is the oscillator strength of the line, give the column density for the line in question.

Because components 2, 3 & 5 are saturated, τ approaches infinity for Lyβ. Thus we did not include Lyβ for the calculation of the HI column in these components.

Lyγ showed the same trait for component 3. Components 2 and 5 however were measureable in Lyγ and Lyδ. Lyδ and Lyη provided good estimates for component 3. For each component we found at least two lines that were measureable for an HI column.

Table. 6.1: Covering Factors

Comp	Velocity km s^{-1}	FWHM km s^{-1}	C$_f$ (O VI)	1-F_r (Ly β)	1-F_r (O VIr)
1	−801	58	0.72	0.11	0.69
2	−608	112	0.69	0.92	0.64
3	−442	97	0.84	0.90	0.83
4	−320	44	0.66	0.35	0.62
5	−130	183	0.95	1.00	0.95

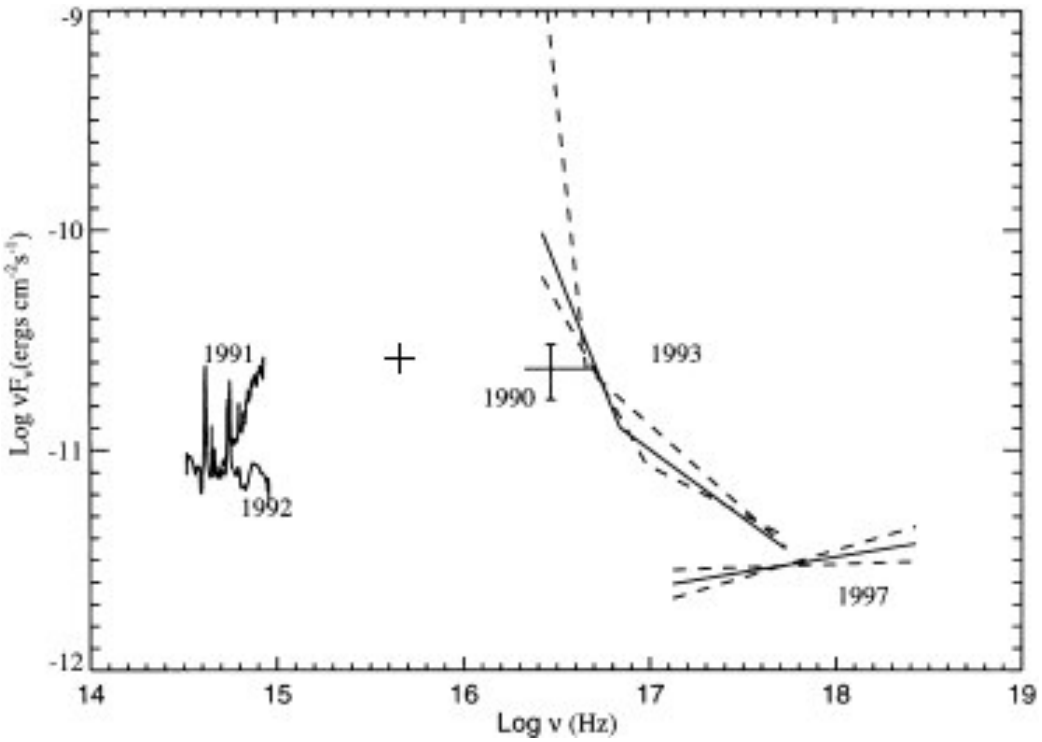

Figure. 6.4: The SED fit for IRAS F22456−5125 from Breeveld et al. (2001). The solid lines are power law fits for the ultra-soft X-Ray, soft X-Ray and hard X-Ray regimes. The spectra are the optical spectra taken by Grupe et al. (1998) and the 1990 point is for the ROSAT observation with respective error bars. We have added a point with the measured continuum flux for *FUSE* marked with a cross.

In O VI component 2, we see that an Fe II ISM line blended with O VI λ 1032 and O VI λ 1038 has an odd unexplicable feature. This feature can be seen in Figure 6.3. We attempted to exclude these features and measure just the absorption line itself. We provide the estimates of column for O VI, C III, N III, and HI in Table 6.2. Errors come from the standard deviation of multiple lines of the same ion; we cannot provide these errors for the C III and N III lines. The N III lines are very weak, if present, in the spectrum; we provide only an upper limit on them. O VI in components 2, 3 and 5 are only lower limit measurements, because we see that 1−F$_r$

is very close to the estimated covering factor, and we therefore we assume that the lines are saturated.

Table. 6.2: Column Densities

Components	N_{HI}	σ_{HI}	N_{OVI}	σ_{OVI}	N_{NIII}	N_{CIII}
			$\times 10^{-14}$ cm^{-2}			
1	3.6	0.77	8.9	1.1	<0.22	<0.033
2	60.2	5.0	>8.2	0.33	3.9	1.6
3	44.7	2.7	>8.7	1.2	<0.59	1.3
4	3.7	1.2	5.2	0.33	<0.13	0.46
5	62.5	5.2	>14.2	1.8	<0.64	1.3

6.3 Photoionization Models

The photoionization models used for this study were generated using the Beta 5 version of Cloudy (Ferland et al. 1998). The models are characterized by an ionization parameter, U [1] , and hydrogen column density, $N_H = N_{H^0} + N_{H^+}$ (in units of cm^{-2}). We assumed roughly solar elemental abundances (e.g. Grevesse & Anders (1989)) and that the absorbing gas was free of cosmic dust. The logs of the elemental abundances, relative to H by number, are as follows: He: -1.00, C: -3.47, N: -3.92, O: -3.17, Ne: -3.96, Na; -5.69, Mg: -4.48, Al: -5.53, Si: -4.51, P: -6.43, S: -4.82, Ar: -5.40, Ca: -5.64, Fe: -4.40, and Ni: -5.75. Because the predicted ionic column densities are not sensitive to density for $n_H < 10^{11}$ cm^{-2}, and we have no constraints on the radial distances of the absorbers, we assumed $n_H = 10^5$ cm^{-3}.

[1] $U = Q/4\pi\ r^2\ c\ n_H$ where r is the radial distance of the absorber and $Q = \int_{13.6eV}^{\infty}(L_\nu/h\nu)\ d\nu$, or the number of ionizing photons s^{-1} emitted by a source of luminosity L_ν

We based our model intrinsic spectral energy distribution on the 1020 Å flux observed with *FUSE* and the X-ray fluxes from Breeveld et al. (2001), as detailed in Section 6.1. We assumed a broken power law of the form $L_\nu \propto \nu^\alpha$ as follows: $\alpha = -0.77$ for energies < 12.15 eV, $\alpha = -1.3$ over the range 12.15 eV $\leq h\nu < 0.3$ keV, $\alpha = -1.6$ for 0.3 keV $\leq h\nu \leq 2$ keV, and $\alpha = -0.8$ for $h\nu > 2$ keV. We included a low energy cut-off at 1.24×10^{-3} eV (1 mm) and a high energy cutoff at 100 keV. The luminosity in ionizing photons is $Q \approx 2 \times 10^{55}$ photons s^{-1}.

The model results are shown in Table 6.3. The models were deemed to have successfully fit the data when the predicted H I and either the C III or the O VI columns were within one sigma of their measured values. For components 2, 3, and 4, the model over-predicts O VI, while fitting the H I and C III, which suggests that the O VI is saturated. The one discrepancy for these components is the under-prediction of the N III in component 2. To rectify this would require a N/C abundance ratio a factor ~ 7 times greater than solar, which seems highly unlikely. In components 1 and 4, we were able to match the H I and O VI columns, indicating that the latter were not saturated. The C III is over-predicted in the component 1 and under-predicted in component 4, by factors of ~ 2.5. In the former case, it is possible that some of the carbon is deposited onto dust grains; there would be no detectable extinction through a cloud with such a low column density, so it is possible that dust is present. In the latter case, there could be density inhomogeneity within the absorber. In that case, the C III would arise in higher-density/lower-ionization gas, while the O VI could

form in more the highly ionized gas (see Kraemer et al. 2001).

Table. 6.3: CLOUDY Model Parameters and Results

Component	log U (cm^2)	log N_H	H I[a]	O VI[a]	C III[a]	N III[a]
				$\times 10^{14}$ cm^{-2}		
1	18.6	−1.32	3.6 (3.6)	9.1 (8.9)	0.09 (<0.03)	0.03 (<0.2)
2	19.9	−1.30	63 (60.2)	172 (>8.8)	1.6 (3.9)	0.52 (1.6)
3	19.7	−1.34	47 (45)	112 (>8.7)	1.3 (1.3)	0.44 (<0.6)
4	18.4	−1.54	4.5 (3.7)	5.0 (5.2)	0.19 (0.5)	0.08 (<0.1)
5	20.0	−1.05	63 (62.5)	266 (>14.2)	1.1 (>14.2)	0.29 (1.3)

[a] Observed values are given in parentheses.

Although Seyferts with intrinsic absorption nearly always possess both UV and X-ray absorption (Crenshaw et al. 2003), *ASCA* spectra of IRAS F22456−5125 do not show evidence for X-ray absorption. In Table 6.4, we list the predicted O VII columns for each of the UV components. The fact that they are all $<3\times 10^6$ cm^{-2} is consistent with the lack of detectable X-ray absorption.

Table. 6.4: O VII Predictions

Component	O VII ($\times 10^{14}$ cm^2)
1	6.0
2	0.01
3	69
4	1.9
5	260

6.4 Conclusions

IRAS F22456-5125 shows continuum variability, stable absorption lines, and a variable soft X-Ray excess. This is a rare object because it shows 5 distinct lines in O VI, whereas most intrinsic absorbers in O VI are blended and saturated compared to C IV and N V.

Another point of interest is that Crenshaw et al. (1999) found a 1:1 correlation between UV absorbers and X-Ray warm absorbers. Based on our measurements and Cloudy modeling, we see UV lines but little evidence for X-Ray absorption. Otherwise, the ultrasoft X-Ray excess seen by Breeveld, Pucharewicz & Otani (2001) would likely be absorbed.

The SED for IRAS F22456−5125 is interesting as well. The two prior observations showed two states for the optical continuum, one in 1991 with a slope of α=+0.8 and one a year later with a slope of α=−1.3. In our observations in 2007, we see that the slope is more like the observation in 1991, possessing a positive slope.

One last interesting point is that the continuum varied by a factor of 6, while the EWs for the absorption features did not. We can estimate the time scale we should see a change for based on typical distances for absorbers at ∼20 pc (Crenshaw et al. 1999). If we consider the ionization time scale to be:

$$t_{ion} = \frac{h\nu}{F_{ion} < \sigma_{ion} >}, \tag{6.3}$$

where $<\sigma>_{ion} \approx 6\times10^{-18}$ cm^2 (Osterbrock 1989) and F_{ion} is the ionizing flux, we can

use an ionizing luminosity from the SED fits from Breeveld et al. (2001) to find the ionizing flux at that distance. The time requred for the cloud at that distance to adjust to the incoming ionizing flux would be $\leq$1 s. With the provided time frame of nearly two years, the clouds would have equilibrated, yet we see no change. According to our photoionization modeling and the covering factors we presented, these lines are saturated. Thus any reaction to a continuum change will be undetectable in O VI. We could use the higher order Lyman series lines to check for variability because they are more likely to be unsaturated; we intend to examine them in the future. Even with unsaturated lines, we would still have a temporal problem for the ionization as we cannot make observations with exposures on the order of seconds. A more viable alternative is to look for recombination, which has a longer time scale than ionization. Because IRAS F22456-5125 has been seen to be variable, this appears to be a case where we need a better cadence so we can pin down the exact Δt for recombination in order to calculate distance and densities.

That's great kid! Don't get cocky!

—— Harrison Ford (Star Wars)

– 7 –

Conclusions

7.1 Summary

For NGC 3516, we presented new spectroscopic data from *FUSE*. Using these new data we calculated a lightcurve for NGC 3516 for several instruments and showed that it is still in a historically low flux state. We examined the H_2 Galactic absorption lines and fitted them with a curve of growth. The H_2 columns we found were $\log(N/cm^{-2})$=18.4, 18.5 and 17.1 for the J=0, 1 and 2 lower rovibrational levels respectively. Also, we fit the intrinsic absorption line profile for the 8 components seen previously by Crenshaw et al. (1999) and Kraemer et al. (2002) and showed that we could use the model predicted columns for O VI to show the residual narrow emission line wing could be seen in the trough of the absorption line, indicating the NLR was not covered by the absorbing clouds.

In the first part of our survey, we saw that 36 of 72 low−z AGN show intrinsic O VI absorption lines. With a value of 0.5 for the fraction of AGN that show NALs, we calculated a global covering factor of 0.42, which holds information about the geometry of the clouds surrounding the BLR and nucleus. Our values are similar to those for AGN of similar and higher luminosities based on C IV absorption (Crenshaw et al. 1999, Laor & Brandt 2002, George et al. 2000).

After we measured each of the absorption lines from our survey, we plotted the data to look for correlations between various observational parameters, such as EW, FWHM, luminosity and velocity. We found the same luminosity-maximum outflow velocity trend Laor & Brandt (2002) found for a higher redshift sample of mixed BALs and NALs. This was reaffirmed by Ganguly et al. (2007), with SDSS data that showed the trend for a mixed NAL and BAL survey to much higher luminosities and redshifts. We saw no trend however for NALs between luminosity, EW, and FWHM. Also, comparing Eddington ratio with EW and velocity revealed no correlation.

We searched the data for variability in the absorption features and attempted to explain the variability we found. We detected variability in 8 of 20 AGN. In the three best cases for potential bulk motion, we showed that the transverse velocities were too large to explain the changes. Thus, we ruled out bulk motion for our set of targets. We found 8 cases of either EW change due to ionizing flux variation or a lack of EW change with a continuum change; the latter can be explained by undersampling of the continuum lightcurves. PG 0804+761 was the one case where we found a change in radial velocity, for which currently we have no explanation.

We saw in two of our targets (PG1411+442 & WPVS 007) that in the troughs of the BALs that the NAL lines were still detectable, and in one of those cases measurable for all three lines. This, combined with the velocity trend, has implications for the driving mechanism for BALs and NALs, along with some geometric information.

We used the SED fits from Breeveld, Pucharewicz & Otani (2001) to model the

five kinematic components in IRAS F22456-5125 using Cloudy. We used the fact that the continuum changed by a factor of ∼6 but the EW lines did not vary to estimate an ionization time scale for the absorbers, which provided little information due to a lack of observations. Also, we found that this object is likely one that disagrees with the 1:1 relationship Crenshaw et al. (1999) found between X-Ray and UV absorbers, in the sense that it has strong UV absorption but no detectable X-Ray absorption from highly ionized gas.

FUSE has provided us with a look into the far UV to study AGN with intrinsic absorption. We found in our survey that O VI was a good choice for determining the number of AGN that contained intrinsic absorption lines; this is primarily due to its high oscillator strength and high abundance. However, *FUSE* had several drawbacks. Because O VI is so sensitive, we found that the majority of the lines we studied in any detail were saturated. While we found that 40% of our available targets showed some evidence of absorption change, saturation generally leads to a lack of variability, such as in the case of IRAS F22456−5125, where we saw a sizable continuum change and no change in EW. Thus, it is possible that a much larger fraction of AGN have variable absorption. Another such problem was contamination from H_2 features, which are abundant shortward of 1030 Å. These features did not affect our O VI and Lyβ studies immensely, but because O VI and Lyβ are so often saturated, it would be better to use the higher order Lyman lines. However, it is difficult in most cases to measure any of the higher order Lyman series lines due to the contamination by

H_2. Only for redshifts z$\geq$0.1 were these lines shifted far enough that we are able to distinguish features.

7.2 Future Work

Our original goal was to examine the relationships between traits like luminosity, accretion rate, AGN type, orientation, and radio power (Crenshaw et al. 2003). We have helped improve our knowledge of the trends between several observables such as luminosity, accretion rate and velocity with the sample we have from *FUSE*. Of course, as in all surveys, we would like a larger survey of NALs to verify and reinforce our trends, and to look for signs of trends we were unable to detect.

In the future, I would like to continue this line of work. It is my belief that a heavy monitoring campaign on a handful of targets (IRAS F22456-5125, WPS 007, etc.) would lead to insight of the heart of AGN and the kinematics of intrinsic absorption. By using variability we have shown that we can estimate distances and densities of these clouds, and coupled with the global covering factor, perhaps we can begin to consider dynamical 3-D models to further our understanding of these phenomena.

The Cosmic Origin Spectrograph (COS) (to be installed on *HST*) will be essential to this process, due to its UV sensitivity. Currently, we have no available instrument to observe the UV. COS will be able to observe the near UV, which contains the C IV doublet. This is an excellent line to use for intrinsic absorption studies (Crenshaw

et al. 1999) because of its sensitivity and abundance. Unlike O VI, C IV is likely to be less saturated in many cases, thus more likely to show EW variations.

Also, I would like to use ground based observations of higher redshift objects to further my research. Over the next two years, I will have access to ground based spectroscopy that I can use to observe the C IV doublet as well as the O VI doublet in higher redshift AGN to continue to look for correlations and variability. Thus far I have focused on NAL objects, and for the optical targets we will be studying BAL quasars as well. I hope to find more ties between these two different phenomena and understand what physical processes create them and drive them.

References

Anderson, K. S., & Kraft, R. P. 1969, ApJ, 158, 859

Antonucci, R. R. J., & Miller, J. S. 1985, ApJ, 297, 621

Arav, N., Korista, K. T., & de Kool, M. 2002, ApJ, 566, 699

Arav, N., Li, Z.-Y., & Begelman, M. C. 1994, ApJ, 432, 62

Begelman, M. C. 1987, in BAAS, Vol. 19, 697

Begelman, M. C., McKee, C. F., & Shields, G. A. 1983, ApJ, 271, 70

Blandford, R. D., & Payne, D. G. 1982, MNRAS, 199, 883

Boroson, T. A., & Green, R. F. 1992, ApJS, 80, 109

Bottorff, M. C., Korista, K. T., & Shlosman, I. 2000, ApJ, 537, 134

Breeveld, A. A., Puchnarewicz, E. M., & Otani, C. 2001, MNRAS, 325, 772

Brotherton, M. S., Green, R. F., Kriss, G. A., Oegerle, W., Kaiser, M. E., Zheng, W., & Hutchings, J. B. 2002, ApJ, 565, 800

Collinge, M. J. et al. 2001, ApJ, 557, 2

Craig, N., & Fruscione, A. 1997, AJ, 114, 1356

Crenshaw, D. M., & Kraemer, S. B. 2001, ApJ, 562, L29

Crenshaw, D. M., Kraemer, S. B., Boggess, A., Maran, S. P., Mushotzky, R. F., & Wu, C.-C. 1999, ApJ, 516, 750

Crenshaw, D. M., Kraemer, S. B., & George, I. M. 2003, ARA&A, 41, 117

Cromwell, R., & Weymann, R. 1970, ApJ, 159, L147

Dixon, W. V. D., Dupuis, J., & Hurwitz, M. 2002, PASP, 114, 112

Dunn, J. P., Crenshaw, D. M., Kraemer, S. B., & Gabel, J. R. 2007, AJ, 134, 1061

Dunn, J. P., Jackson, B., Deo, R. P., Farrington, C., Das, V., & Crenshaw, D. M. 2006, PASP, 118, 572

Elvis, M., Plummer, D., Schachter, J., & Fabbiano, G. 1992, ApJS, 80, 257

Emmering, R. T., Blandford, R. D., & Shlosman, I. 1992, ApJ, 385, 460

Feldman, P. D., Sahnow, D. J., Kruk, J. W., Murphy, E. M., & Moos, H. W. 2001, J. Geophys. Res., 106, 8119

Ferland, G. J., Korista, K. T., Verner, D. A., Ferguson, J. W., Kingdon, J. B., & Verner, E. M. 1998, PASP, 110, 761

Ficarra, A., Grueff, G., & Tomassetti, G. 1985, A&AS, 59, 255

Fields, D. L., Mathur, S., Pogge, R. W., Nicastro, F., Komossa, S., & Krongold, Y. 2005, ApJ, 634, 928

Foltz, C. B., Chaffee, F. H., Hewett, P. C., Weymann, R. J., & Morris, S. L. 1990, in BAAS, Vol. 22, 806

Gabel, J. R. et al. 2003, ApJ, 595, 120

Ganguly, R., Brotherton, M. S., Cales, S., Scoggins, B., Shang, Z., & Vestergaard, M. 2007, ApJ, 665, 990

Ganguly, R., Charlton, J. C., & Eracleous, M. 2001, ApJ, 556, L7

George, I. M., Mushotzky, R., Turner, T. J., Yaqoob, T., Ptak, A., Nandra, K., &

Netzer, H. 1998, ApJ, 509, 146

George, I. M., Turner, T. J., Yaqoob, T., Netzer, H., Laor, A., Mushotzky, R. F., Nandra, K., & Takahashi, T. 2000, ApJ, 531, 52

Gillmon, K., Shull, J. M., Tumlinson, J., & Danforth, C. 2006, ApJ, 636, 891

Greenstein, J. L., & Matthews, T. A. 1963, AJ, 68, 279

Greenstein, J. L., & Schmidt, M. 1964, ApJ, 140, 1

Grevesse, N., & Anders, E. 1989, in American Institute of Physics Conference Series, Vol. 183, Cosmic Abundances of Matter, ed. C. J. Waddington, 8

Grupe, D., Beuermann, K., Thomas, H.-C., Mannheim, K., & Fink, H. H. 1998, A&A, 330, 25

Grupe, D., Thomas, H.-C., & Beuermann, K. 2001, A&A, 367, 470

Halpern, J. P. 1984, ApJ, 281, 90

Hamann, F., Barlow, T. A., Junkkarinen, V., & Burbidge, E. M. 1997, ApJ, 478, 80

Hazard, C. 1962, MNRAS, 124, 343

Kaspi, S., Smith, P. S., Netzer, H., Maoz, D., Jannuzi, B. T., & Giveon, U. 2000, ApJ, 533, 631

Khachikian, E. Y., & Weedman, D. W. 1974, ApJ, 192, 581

Kraemer, S. B., Crenshaw, D. M., & Gabel, J. R. 2001, ApJ, 557, 30

Kraemer, S. B. et al. 2006, ApJS, 167, 161

Kraemer, S. B., Crenshaw, D. M., George, I. M., Netzer, H., Turner, T. J., & Gabel, J. R. 2002, ApJ, 577, 98

Kraemer, S. B., Crenshaw, D. M., Yaqoob, T., McKernan, B., Gabel, J. R., George, I. M., Turner, T. J., & Dunn, J. P. 2003, ApJ, 582, 125

Kraemer, S. B. et al. 2005, ApJ, 633, 693

Kriss, G. A. 2002, in Astronomical Society of the Pacific Conference Series, Vol. 255, Mass Outflow in Active Galactic Nuclei: New Perspectives, ed. D. M. Crenshaw, S. B. Kraemer, & I. M. George, 69

Kriss, G. A., Espey, B. R., Krolik, J. H., Tsvetanov, Z., Zheng, W., & Davidsen, A. F. 1996, ApJ, 467, 622

Krolik, J. H., & Begelman, M. C. 1986, ApJ, 308, L55

——. 1988, ApJ, 329, 702

Krolik, J. H., & Kriss, G. A. 1995, ApJ, 447, 512

Lanzetta, K. M., Turnshek, D. A., & Sandoval, J. 1993, ApJS, 84, 109

Laor, A., & Brandt, W. N. 2002, ApJ, 569, 641

Leighly, K. 2007, in prep

Maran, S. P., Crenshaw, D. M., Mushotzky, R. F., Reichert, G. A., Carpenter, K. G., Smith, A. M., Hutchings, J. B., & Weymann, R. J. 1996, ApJ, 465, 733

Mason, K. O. et al. 1995, MNRAS, 274, 1194

McLure, R. J., & Dunlop, J. S. 2004, MNRAS, 352, 1390

Morton, D. C. 1991, ApJS, 77, 119

Oke, J. B., & Sargent, W. L. W. 1968, ApJ, 151, 807

Osterbrock, D. E. 1989, Astrophysics of gaseous nebulae and active galactic nuclei (Research supported by the University of California, John Simon Guggenheim Memorial Foundation, University of Minnesota, et al. Mill Valley, CA, University Science Books, 1989, 422 p.)

Penton, S. V., Stocke, J. T., & Shull, J. M. 2002, ApJ, 565, 720

Peterson, B. M. 1997, An Introduction to Active Galactic Nuclei (Cambridge, New York Cambridge University Press)

Peterson, B. M. et al. 2004, ApJ, 613, 682

Peterson, B. M., Wanders, I., Bertram, R., Hunley, J. F., Pogge, R. W., & Wagner, R. M. 1998, ApJ, 501, 82

Reynolds, C. S. 1997, MNRAS, 286, 513

Romano, P., Mathur, S., Pogge, R. W., Peterson, B. M., & Kuraszkiewicz, J. 2002, ApJ, 578, 64

Sahnow, D. J. et al. 2000, ApJ, 538, L7

Savage, B. D., & Sembach, K. R. 1991, ApJ, 379, 245

Schmidt, M. 1962, ApJ, 136, 684

Scott, J. E. et al. 2004, ApJS, 152, 1

——. 2005, ApJ, 634, 193

Seyfert, C. K. 1943, Contributions from the Mount Wilson Observatory / Carnegie Institution of Washington, 671, 1

Shakura, N. I., & Syunyaev, R. A. 1973, A&A, 24, 337

Shull, J. M., & Sachs, E. R. 1993, ApJ, 416, 536

Siegmund, O. H. et al. 1997, in Proc. SPIE EUV, X-Ray, and Gamma-Ray Instrumentation for Astronomy VIII, Oswald H. Siegmund; Mark A. Gummin; Eds., ed. O. H. Siegmund & M. A. Gummin, Vol. 3114, 283

Tumlinson, J. et al. 2002, ApJ, 566, 857

Turner, T. J. et al. 2002, ApJ, 568, 120

Turnshek, D. A., Grillmair, C. J., Foltz, C. B., & Weymann, R. J. 1988, ApJ, 325, 651

Ulrich, M. H., & Boisson, C. 1983, ApJ, 267, 515

Ulrich, M.-H., Courvoisier, T. J.-L., & Wamsteker, W. 1988, A&A, 204, 21

Vestergaard, M. 2003, ApJ, 599, 116

Vestergaard, M., & Peterson, B. M. 2006, ApJ, 641, 689

Wakker, B. P. 2006, ApJS, 163, 282

Weymann, R. J., Carswell, R. F., & Smith, M. G. 1981, ARA&A, 19, 41

York, D. G., Ratcliff, S., Blades, J. C., Wu, C. C., Cowie, L. L., & Morton, D. C. 1984, ApJ, 276, 92

Zheng, W. et al. 2001, ApJ, 562, 152

Appendices

– A –

Notes on Individual Objects with Intrinsic Absorption

A.1 QSO 0045+3926

QSO 0045+3926 is a new intrinsic absorption discovery. We find that this object shows clear single-line absorption in all three lines. The O VI region is found in the SiC portion of the spectrum; while the signal-to-noise is less, there are no ISM lines nor any H_2 contamination.

A.2 Ton S180

Ton S180 shows very weak absorption, with some contamination from H_2 and a N II ISM line in the Lyman β line and no sign of H_2 absorption in the O VI red member. The Fe II ISM lines appear to be negligible based on the essentially non-visible nearby lines. This object was first seen as an absorber in Kriss (2002) but no intrinsic absorption was detected longward of 1200 Å. Also, this object shows little to no evidence for X-ray absorption. (Turner et al. 2002)

A.3 Mrk 1044

Fields et al. (2005) have identified the same lines we found in the *FUSE* observation. The obvious component appears in both the O VI lines, but the Lyman β line is seriously contaminated by H_2. There is also evidence for a weaker line that appears to be slightly blended with Ar I in the O VI blue member, but is not clearly visible in O VI red and non-existent in Lyman β.

A.4 NGC 985

Absorption for this target was reported by Kriss (2002). Kriss lists this target with only one component, while we find that there are three narrow line absorbers with one blended broad absorber, which may consist of be two sub-components. The H_2 spectrum is present in each of the O VI and Lyman β lines, but weak nearby. This allows for clear identification of each of these intrinsic absorption lines.

A.5 EUVE J0349-537

EUVE J0349−537 was first found in the EUVE survey and the optical counterpart was found by Craig & Fruscione (1997). Since that time it has appeared in 4 more surveys, but it has not been studied carefully. This target shows one absorber that is broad enough that it is clearly above the noise, with a second nearby absorption feature that could be noise as it is only slightly visible in the O VI lines. This is a new absorption detection.

A.6 IRASF 04250-5718

This object originated in the Einstein Slew Survey (Elvis et al. 1992). We find at least two components absorbing in the far ultraviolet. It shows a broad component blended with a narrower component at a slightly lower velocity with very little contamination. This absorption has been seen previously by Kraemer et al. (1999).

A.7 Mrk 79

We see one component that is broad and shows very little contamination in the O VI lines. The Lyman β line is significantly weaker but still visible with little contamination. The second component is a narrow feature that is visible in the O VI red member, while the blue is highly contaminated and the Lβ absorption is weak at best. This absorption has been identified previously (Crenshaw & Kraemer 2001).

A.8 Mrk 10

This object shows H_2 contamination in both of the O VI doublet lines, and Ar I (λ1067) in the O VI red member. The absorption features are much too broad for H_2 and ISM absorption to completely explain them. Thus we find one or possibly two broad blending components. Mrk 10 has not been identified before as an intrinsically absorbing object.

A.9 IR 07546+3928

This object was found in the New Bologna Sky Survey (Ficarra et al. 1985); it has been flagged for possible C IV absorption studies with the *International Ultraviolet Explorer (IUE)* (Lanzetta et al. 1993). It has however not been labeled as an intrinsic absorbing target until now. In the *FUSE* observations there are two broad components which are heavily contaminated in the O VI blue member by Fe II ISM lines. The Ly β and the O VI red member are fairly devoid of contamination.

A.10 PG 0804+761

While the spectrum of this object shows dayglow N I, the intrinsic absorption lines are evident with no clear interference from ISM. This object is a newly found intrinsic absorber.

A.11 Ton 951

Ton 951 was identified by Kriss (2002). We find a single narrow absorption feature. Only one of the three available lines has any H_2 contamination.

A.12 IRAS 09149-62

One of the less well-studied AGN targets, IRAS 09149-62 shows broad absorption features across both members of the O VI doublet. The N II dayglow lines leave

whether or not Lyβ shows absorption open to speculation. This detection is a first for this object.

A.13 Mrk 141

This spectrum is highly noisy and the continuum flux level is extremely low. There are two lines from O VI that are in the same place in velocity space, but this object is not an ideal example of an intrinsic absorber due to the lack of a Lyβ line at that velocity. It was classified as an intrinsic absorber by Kriss (2002).

A.14 NGC 3516

We present in this thesis 2 new observations of NGC 3516 taken by *FUSE*. There have been a total of 6 observations taken with *FUSE*. In the first observation Kriss (2002) identified the same components seen in FOS, STIS and GHRS data by Crenshaw et al. (1999) and Kraemer et al. (2001). Kraemer et al. showed that NGC 3516 shows variability in the absorption features, allowing them to find a lower limit on the transverse velocity of $\sim$1800 km s^{-1}.

A.15 ESO 265-G23

This spectrum is full of H_2 features; however there is at least one absorption feature and two more possible components. The Lyβ for the second possible component has a strong N II ISM line in it while the O VI red member is aligned with a Fe II ISM

line. This is a new intrinsic UV absorption discovery.

A.16 NGC 3783

NGC 3783 was heavily studied by Gabel et al. (2005) using STIS and *FUSE* spectra. We find two broad components covering the span between -500 and -800 km s^{-1}, which agrees with Gabel et al. (2005). However Gabel et al. found a component at -1350 km s^{-1} which is coincident with a feature in Lyβ.

A.17 NGC 4051

NGC 4051 shows a broad absorbing region that has no real contamination in the O VI blue member. The O VI red member is visible, but an O I dayglow line lies inside the trough and the Ly β has a similar problem with an O I dayglow line alongside the Ly β dayglow line. Using STIS, Collinge et al. (2001) found two absorbing systems, one at ~ -600 km s^{-1} and one at ~ -2400 km s^{-1}. Each of these broad components break into up to 8 smaller components in STIS spectra in the C IV and N V lines. In the *FUSE* data we see only the lower velocity component. There is no evidence in the *FUSE* spectrum for a higher velocity component.

A.18 NGC 4151

Kraemer et al. (2006, and references therein) performed an in depth study on NGC 4151, which showed multiple components in STIS spectra. In the *FUSE* data we

find multiple components blended together due to the sensitivity of O VI to intrinsic absorption. The Lyβ region is spoiled by the Lyβ dayglow. We only provide the centroid of the velocity in Table 2 for this object.

A.19 RXJ 1230.8+0115

Due to the high redshift of RXJ 1230.8+0115, there is little interference from the ISM (only 3 Fe II lines). There appears to be at least one broad component with 2 other unexplained lines (1051 Å and 1050 Å) with two other broad absorption regions which do not have corresponding matches in velocity space. This was recognized by Ganguly et al. (2001) and attributed to intervening gas in the IGM.

A.20 TOL 1238-364

This object has been classified as a Seyfert 2 galaxy (NED), but there does seem to be evidence for a broad line region in the *FUSE* spectrum. We find 1 broad component that shows some contamination from H_2, Ar I, and C I. Because this has been labeled as a Seyfert 2 galaxy, it seems this object has not been considered as a target for intrinsic absorption studies.

A.21 PG 1351+640

PG 1351+640 has ample ISM contamination, but the overall absorption features look to be the same in all three lines. This was seen by Kriss (2002) and fitted by Zheng

et al. (2001).

A.22 Mrk 279

As seen by Kriss (2002) and followed up with further study and Chandra observations by Scott et al. (2004), we find that there are three possible components in Mrk 279. Of the three, only one is free from question of contamination. The other two could be combinations of H_2 or ISM lines; however, there seems to be a paucity of H_2 absorption in nearby regions of the spectrum. Two of the three features appear to be intrinsic absorption.

A.23 RXJ 135515+561244

This spectrum is in a very low continuum flux state, but shows evidence for one component of absorption with no contamination. This is a new intrinsic UV absorption discovery.

A.24 PG 1404+226

While the spectrum shows heavy ISM contamination, there are three absorption components uncorrupted in the O VI red member. These components agree in velocity with their O VI blue member and Ly β counterparts and have very little overlap with the ISM lines. This was a common target with the Laor & Brandt (2002) survey.

A.25 PG 1411+442

Laor & Brandt (2002) found that PG 1411+442 showed a large range of velocity for the intrinsic absorption (∼5000 km/s). We see the broad absorption Laor & Brandt found, but we also have found two narrow components that are quite clear.

A.26 NGC 5548

NGC 5548 was found to be intrinsically absorbing by Shull & Sachs (1993) in data from *IUE* along with evidence of X-Ray warm absorption (George et al. 1998). Crenshaw et al. (1999) found absorption in FOS data as well. More recently Crenshaw et al. (2003) saw five blended and broad components in data from STIS. We see in the *FUSE* data a situation similar to that as Crenshaw et al. found, with five blended and broad components.

Brotherton et al. (2002) examined the *FUSE* data available prior to 2002 and found intrinsic absorption spanning the range between 0 and -1300 km s^{-1}, which is coincident with what we have found in our coadded spectrum.

A.27 Mrk 817

We consider this a weak absorber. Mrk 817 shows a weak absorption line that is isolated in the O VI blue member, and has a weak Fe II contamination in the O VI red member. The Ly β is hardly visible, but this is easily understood due to the lower sensitivity of Ly β. This object has the fastest radial velocity component in a Seyfert

galaxy to date (Table 5.3), as seen in Kriss (2002).

A.28 Mrk 290

Seen by Kriss (2002), the absorber is a narrow (∼200 km/s FWHM) absorption component. There is some possibility for contamination in each of the three lines; however, the amount of contamination can be estimated from nearby ISM features. Because the nearby features have larger oscillator strengths and are weak lines, this contamination must be small in our absorption features.

A.29 Mrk 876

We see an O VI broad line, with a few narrow absorption features that are most likely intrinsic, and have not been seen before.

A.30 Mrk 509

Mrk 509 shows absorption broad enough that it was first seen in data from *IUE* by York et al. (1984). It also shows evidence for an X-Ray warm absorber, as discussed in Reynolds (1997) and George et al. (1998). Kriss (2002) published the *FUSE* spectrum and identified the absorption components.

Kraemer et al. (2003) examined STIS data and found 8 components spanning the velocity range between -422 and $+210$ km s^{-1}. They performed photoionization models of the absorbers and found that they are not the same absorbing regions as

the X-Ray absorbers.

In the *FUSE* observations with high resolution, in the Lyβ absorption feature we see the two same broad absorbers, but due to the fact that the Lyβ line is less sensitive, we can see that the two broad components are composed of between 4 and 5 components, the fifth overlapping with a coincident H_2 line.

A.31 II Zw 136

Crenshaw et al. (1999) found two components in the FOS spectra for II Zw 136, which we see repeated in our *FUSE* observations. Component 1 is clearly visible and virtually free of ISM interference; component 2 in the *FUSE* observations is clearly seen only in the O VI red member. Ly β is weak at best and the O VI blue member is heavily contaminated with an Fe II line and two H_2 lines in the vicinity.

A.32 Akn 564

Akn 564 shows 2 broad and blended absorption components. H_2 lines heavily populate the area, but are far too narrow to account for the absorption. Crenshaw et al. (1999) saw absorption in the FOS data at the same central velocities we find. Romano et al. (2002) published the *FUSE* spectrum for this target and also identified the same components we find. Crenshaw & Kraemer (2001) found that this was 1 of 2 Seyfert galaxies that showed traits they characterized as a dusty lukewarm absorber.

A.33 IRASF 22456-5125

This object was seen first in the ROSAT wide field survey and later observed in the EUV. X-Ray studies have found this target to be highly variable (Grupe et al. 2001), but no ultraviolet intrinsic absorption has been previously identified. In our spectra we find 5 'finger-like' narrow absorption components with little to no contamination from the ISM.

A.34 MR 2251-178

Ganguly et al. (2001), using FOS and STIS observations, found variability in the absorption in both velocity and column density. They found that the velocity of the component was ~ -1300 km s^{-1}, in data from STIS and FOS. We find that this object shows clear absorption in both Lyβ and the O VI red member. While the blue member has both H_2 and ISM contamination, the velocity overlap is adequate enough to say that a significant portion of the absorption feature is intrinsic to the object.

The question for MR 2251−178 is whether the absorption is best aligned at -2000 km s^{-1} where the Lyβ absorption is weak and possibly just ISM contamination, or at -300 km s^{-1} where the O VI red member is weak. This could be a case of coincidental alignment where there are absorbers at both of these velocities; thus two of the features will be broader than the third component. Because X-Ray studies have shown this source to be highly variable in X-Ray absorption (Halpern 1984), and also

to be variable in the UV (Ganguly et al. 2001) it seems likely that the velocity of the component in the *FUSE* data is either -2000 km s^{-1} or -300 km s^{-1}.

A.35 NGC 7469

NGC 7469 is a highly studied Seyfert 1 galaxy. Many surveys and studies to date have classified this as an intrinsically absorbing Seyfert galaxy (Scott et al. 2005; Kriss 2002; Crenshaw et al. 1999). Thus this object is a known intrinsic absorber. In the *FUSE* data however, the absorption appears very weakly and in the Lyman β line there is a C II ISM line along with two heavy H_2 lines leaving doubt to the absorption feature. The O VI blue line is found at the same wavelength as Ar I (λ 1048 Å) which tends to be a strong ISM line in the far UV.

– B –

Notes on Individual Measurements

B.1 QSO 0045+3926

Lyman β is hard to measure for D1310105. In all other observations, the absorption lines appear to be single narrow features.

B.2 Ton S180

O VI λ1032, is not visibile and Lyman β is corrupted by a blend of Fe II, N II and H_2 ISM lines. O VI λ1037 is a clean absorption feature.

B.3 Mrk 1044

O VI λ1037 is blended with an H_2 complex in component 1 and 2. Lyman β is possibly contaminated by H_2 as well for component 1. Component 2 is weak based on the one more easily visible O VI λ1032 line, and virtually nonexistent in Lyman β

B.4 NGC 985

Four components are visible and measurable. Component 1 has contamination from H_2 in both Lyman β and O VI(1037). Component 2 has possible contamination in

Lyman β. Components 2 and 4 are blended slightly with component 3 in the O VI (1032) line.

B.5 EUVE J0349-537

All of the lines are clean narrow absorption features. They show some wing asymmetry towards the red, possibly due to another blended absorption component.

B.6 IRASF 04250-5718

Components 1 and 2 are very close in velocity space, but separable in our measurements. O VI λ1037 could have some contamination from Fe II.

B.7 Mrk 79

Component 1 is blended with H_2 for Lyman β and O VI λ1032; O VI λ1037, however, is a narrow single line. Component 2 appears to be broader and possibly multicomponent. It appears very weak in Lyman β, and could be contaminated by H_2.

B.8 Mrk 10

We measured across both visible components. It was too difficult to estimate the amount of blending. Both O VI λ1037 and O VI λ1032 are blended with H_2, and O VI λ1032 has possible Fe II ISM features imbedded.

B.9 IR 07546+3928

Both components are broad, most likely saturated features. Some H_2 blending in the O VI λ1032 line.

B.10 PG 0804+761

H_2 and ISM have lines free of contamination, with single narrow features.

B.11 Ton 951

Ton 951 has narrow single lines that look to be rather flat in the cores, thus most likely saturated. Only Lyman β has any possible contamination.

B.12 IRAS 09149-62

The feature is broad and most likely multi-component. O VI λ1032 has a false line where the segments do not overlap. Lyman β is buried beneath a plethora of geocoronal dayglow lines.

B.13 Mrk 141

This spectrum is too noisy to measure the lines.

B.14 NGC 3516

Multi-component absorption features for NGC 3516 have been seen in the past (Crenshaw et al. 1998). We can distinguish 5 of these features, but 4 and 5 are too blended for individual measurements, while heavy H_2 contamination pollutes the other features.

B.15 ESO 265-G23

In the A1210405 observation, O VI λ1037 was weak and too hard to measure, and in the A1210408 observation, the width of the line was uncertain. For component 2, Lyman β has contamination from a N II ISM line, while O VI λ1037 has a stong Fe II line coincident.

B.16 NGC 3783

Components 1 and 2 are strong broad features that blend significantly. We have measured across both. O VI λ1032 has several sources of possible contamination.

B.17 NGC 4051

Heavy dayglow lines appear in both the B0620201 and C0190101 observations for O VI λ1037 and in all three observations for Lyman β. O VI λ1032 is a broad feature probably containing muliple components.

B.18 NGC 4151

O VI resolves into individual highly blended components for the first and third observations, and O VI λ1037 is laced with several H_2 lines that probably produce contamination. Lyman β has heavy dayglow in all 4 observations.

B.19 RXJ 1230.8+0115

This is a multi-component system. There are 4 features for each of the O VI lines, and none visable for Lyman β. All but component 2 seem to be saturated.

B.20 TOL 1238-364

The feature has heavy H_2 in Lyman β along with a C II ISM line, while O VI (1037) has contamination from Ar I.

B.21 PG 1351+640

All lines were measurable for both components. Only in component 1 for O VI (1037) is there any real ISM contamination possible.

B.22 Mrk 279

O VI (1032) is blended with either an Fe II ISM line or an H_2 feature. Both components are blended and cannot be measured independently.

B.23 RXJ 135515+561244

Components 1 and 2 are blended and measured together. Measured components 3 and 4 are blended together as well, but not readily visible in Lyman β

B.24 PG 1404+226

Component 1 is weak in Lyman β, while 2 and 3 are blended. We measured across both components 2 and 3.

B.25 PG 1411+442

This object has a BAL beyond 1127 Å, with residual flux to $\sim$ 1120 Å. We see two narrow components we measured together for O VI red, but the O VI blue members are very weak and hard to measure. Lyman β is completely wiped out by the BAL.

B.26 NGC 5548

In the program ID D15501 observations, we were unable to measure the components at all. The P1014601 observation however provided O VI measurements for both components, Lyman β was not measurable.

B.27 Mrk 817

No Lyman β was visible. Both members of the O VI doublet are broad features that appear to be single individual components; only O VI blue has any possible contamination from H_2.

B.28 Mrk 290

Similar to Mrk 817, Mrk 290 has semi-broad features that appear to be single components. Fe II is aligned with Lyman β, and H_2 features are aligned with the O VI members.

B.29 Mrk 876

Mrk 876 has very weak absorption, that appears to be clean in O VI. Lyman β is either nonexistent and the Fe II ISM line is the predominant feature or is heavily contaminated by the ISM line.

B.30 Mrk 509

Two broad features are visible, and are composed of 8 blended components (Kraemer 2002). Some H_2 is present in all three lines but it is unclear how much in affect, the aborption. We measured across what look to be two components as one line, and three components for another.

B.31 II Zw 136

These data show two components: one fast moving component and one much slower. This causes the O VI (1032) line and the O VI (1037) line to blend and makes this useless to measure, while component 1 for both O VI (1032) and Lyman β are measurable. Component 2 is weak in Lyman β and susceptible to noise; the line for O VI (1037) however, is very strong and appears to be a single component with no blending.

B.32 Akn 564

Akn 564 shows 2 very broad components that overlap and are indistinguishable from one another at the continuum level; thus we measured across both.

B.33 IRASF 22456-5125

Five individual components are easily discernable for both members of the O VI doublet, while Lyman β has 3 strong and 2 weak components. The O VI doublet has possible contamination by Fe II and in O VI blue there is a N I complex interfering. We measured each of the components available; however the ISM contamination in component 2 of O VI blue was unavoidable, and had to be left unmeasured.

B.34 MR 2251-178

There is possible O VI (1037) contamination from H_2 and Fe II, while the other two lines appear to remain unscathed. Lyman β is a strong broad line, while the O VI lines are weaker and appear to be only single components.

B.35 NGC 7469

This is a very noisy spectra that we have no LiF 1b data for. We were able to distinguish both members of the O VI doublet with no contamination. Lyman β however proved to be elusive.